January 2020

Enhanced Hydrocarbon Recovery In Tight And Shale Reservoirs Using Surfactants And Supercritical CO2

Shaojie Zhang

ENHANCED HYDROCARBON RECOVERY IN TIGHT AND SHALE RESERVOIRS USING SURFACTANTS AND SUPERCRITICAL CO_2

by

Shaojie Zhang

Bachelor of Science, China University of Petroleum (East China), 2014

Master of Engineering, China University of Petroleum (East China), 2017

A Dissertation

Submitted to the Graduate Faculty

of the

University of North Dakota

In partial fulfillment of the requirements

for the degree of

Doctor of Philosophy

Grand Forks, North Dakota

December

2020

Name: Shaojie Zhang

Degree: Doctor of Philosophy

This document, submitted in partial fulfillment of the requirements for the degree from the University of North Dakota, has been read by the Faculty Advisory Committee under whom the work has been done and is hereby approved.

DocuSigned by:
Hui Pu
C63B8AB854E4448...
Dr. Hui Pu

DocuSigned by:
Vamegh Rasouli
0EB956E8C9C9456...
Dr. Vamegh Rasouli

DocuSigned by:
Kegang Ling
AE10F7CCAFC7487...
Dr. Kegang Ling

DocuSigned by:
Dongmei Wang
08C8564EBF15478...
Dr. Dongmei Wang

This document is being submitted by the appointed advisory committee as having met all the requirements of the School of Graduate Studies at the University of North Dakota and is hereby approved.

DocuSigned by:
Chris Nelson
2E0AF068C733403...
Chris Nelson
Dean of the School of Graduate Studies

12/10/2020
Date

PERMISSION

Title Enhanced hydrocarbon recovery in tight and shale reservoirs using surfactants and supercritical CO_2

Department Petroleum Engineering

Degree Doctor of Philosophy

In presenting this dissertation in partial fulfillment of the requirements for a graduate degree from the University of North Dakota, I agree that the library of this University shall make it freely available for inspection. I further agree that permission for extensive copying for scholarly purposes may be granted by the professor who supervised my dissertation work or, in his absence, by the Chairperson of the department or the dean of the Graduate School. It is understood that any copying or publication or other use of this dissertation or part thereof for financial gain shall not be allowed without my written permission. It is also understood that due recognition shall be given to me and to the University of North Dakota in any scholarly use which may be made of any material in my dissertation.

Shaojie Zhang
December 7, 2020

ACKNOWLEDGEMENTS

I would like to express my sincere gratitude to my advisor Dr. Hui Pu for his insightful guidance and encouragement during my Ph.D.'s study in the Department of Petroleum Engineering at the University of North Dakota. Without his support and supervision, the dissertation would not be possible.

I also thank other members of my advisory committee, Dr. Vamegh Rasouli, Dr. Kegang Ling, and Dr. Dongmei Wang. Thank Dr. Rasouli, Dr. Ling, and Dr. Wang for giving valuable advice, instructions, and encouragement during my Ph.D. study.

Next, I would like to thank the financial support from North Dakota Industrial Commission Oil and Gas Research Program (Contract No. G-041-081) and thank North Dakota Geological Survey Wilson M. Laird Core and Sample Library for providing core samples.

Finally, and most importantly, I would like to thank my parents and brother for their encouragement and love.

DEDICATION

This dissertation is dedicated to my family for their

love and support throughout my life.

ABSTRACT

The tight and shale oil reservoirs have been becoming increasingly important energy resources. However, the flow and storage mechanisms of oil in tight and shale reservoirs are still ambiguous. The inorganic pores, organic pores, and kerogen skeleton in shale oil reservoirs can store hydrocarbons. Besides, the oil recovery of tight and shale oil reservoirs is extremely low even with the assistance of hydraulic fracturing and horizontal drilling. The surfactants and CO_2 are commonly used to enhance the oil recovery in tight and shale reservoirs. A comprehensive review of CO_2 and surfactants EOR is shown in Chapter II.

The spontaneous imbibition is a very important mechanism for oil production from fractured reservoirs. The counter-current spontaneous imbibition experiments and nuclear magnetic resonance (NMR) were combined to study the imbibition and the fluid distribution in eight core samples. NMR is able to detect fluid distribution in different sizes of pores ranging from micropores to fractures. Before the experiments, the Middle Bakken and Berea cores were saturated with air. Then imbibition experiments with one end open (OEO) and two ends closed (TEC) boundary conditions were carried out. The numerical solutions of spontaneous imbibition models match quite well with experimental results by adjusting model parameters. The capillary pressure and relative permeability curves were obtained from the matching. The imbibition experiments, mathematical models, and nuclear magnetic resonance (NMR) results are discussed in Chapter III.

Surfactants are very common chemicals for EOR in fractured tight reservoirs. We

experimentally investigated the EOR using various kinds of surfactants. Six core samples were obtained from the Middle Bakken Formation in North Dakota. Before the imbibition experiment, petrophysical analyses were conducted for the samples. XRD method was used to analyze the mineral composition. Nitrogen adsorption and SEM methods were combined to study the pore size distribution and microstructures. Then I performed brine imbibition and surfactant imbibition in six Bakken cores and two Berea sandstones. Before the experiment, the cores were fully saturated with Bakken crude oil. The core plugs were then submerged into the brine and surfactant solutions with an all-face-open (AFO) condition. Experiments of brine and surfactant imbibing into oil-filled cores were carried out with the recording of recovered oil volume using imbibition cells. Different types of surfactants such as cationic, anionic, and nonionic, were tested in the study. Those experiments and the results are presented in Chapter III.

The shale oil reservoirs have much complex storage and flow mechanisms. The inorganic pores, organic pores, and kerogen matrix are important media to store water and oil in shale rocks. We present a vacuum imbibition method to identify the volume of water and oil in these media. Before the experiments, comprehensive rock characterizations were carried out on shale samples from Shahejie Formation combining various methods including N_2 adsorption, scanning electron microscope (SEM), X-ray diffraction, and RockEval pyrolysis. Then, vacuum imbibition experiments were conducted on shale samples using water and n-dodecane. The accurate volumes of water in organic pores, oil in inorganic pores and organic pores, and the volume of dissolved oil were determined from vacuum imbibition experiments. The effects of thermal maturity (Ro) on shale storage were analyzed. Furthermore, novel mathematical models of oil and water vacuum imbibition in shale were proposed. The water imbibition in inorganic pores is a capillary flow. The oil imbibition in shale includes capillary flow in pore structures and diffusion in kerogen. The

pore-kerogen double diffuse layer (PKDDL) physical model was proposed for the mechanisms of the hydrocarbon mass transfer between pore structures and kerogen. The capillary pressure and the dissolution rate constants were obtained by matching mathematical models with experimental results. This method is crucial for evaluating the water and oil storage and transfer in organic-rich shale and advances the crucial mechanisms for the evaluation and development of shale reservoirs. The experimental method, mathematical models, and results of the vacuum imbibition study are in Chapter IV.

The oil recovery of shale reservoirs is very low due to the extremely low permeability and the existence of organic matter. CO_2 injection in shale oil reservoirs is a feasible method for CO_2 geological sequestration and enhanced oil recovery. However, the mechanisms of mass transfer in inorganic pores and organic matter (kerogen) are still ambiguous. Thus, the mechanisms of diffusion and extraction were investigated. A novel pore-kerogen diffuse layer (PKDL) model was proposed for mass transfer between kerogen matrix and pores (inorganic pores and organic pores). Mathematical models for hydrocarbon mass transfer in spherical and cylindrical shaped rocks were derived. The predicted responses of the mathematical models closely matched the experimental data of CO_2 injection experiments. Hydrocarbon recovery of shales shows a delayed effect compared to tight rocks due to the additional extraction process between supercritical CO_2 and kerogen. Hydrocarbons were extracted out of the kerogen matrix and then diffused through the inorganic and organic pores. This theoretical research advances the diffusion and extraction theories in shale oil. The models and results are shown in Chapter V.

TABLE OF CONTENTS

LISTS OF FIGURES

LISTS OF TABLES

CHAPTER I

INTRODUCTION

1. Motivations

Unconventional oil and gas are becoming increasingly important energy in the past decade. However, the oil recovery of tight and shale oil reservoirs is generally lower than 10% IOOP (Hawthorne et al., 2019b). Besides, the storage of water and oil in shale formations is much more complex than that in the tight reservoirs and conventional reservoirs (Xie et al., 2019; Zhang et al., 2020). Thus, it is desirable to comprehensively investigate the storage, flow mechanisms, and EOR in unconventional reservoirs.

The wettability of tight reservoirs can be changed from oil-wet to water-wet by using different surfactants (Meng et al., 2018). The imbibition process is a very important mechanism for oil recovery from fractured tight reservoirs. The oil can be displaced out at the presence of capillary pressure Alvarez et al., 2017). Thus, the water imbibition experiments are systematically investigated using air-saturated tight Bakken cores and Berea sandstone core samples. Imbibition experiments are carried out in two-end-closed (TEC) and one-end-opened (OEO) boundary conditions. The capillary pressure and relative permeability curves are obtained by matching experimental results with mathematical models. In addition, water and surfactant imbibition experiments are performed on oil-saturated tight Bakken cores. The oil recovery is recorded during the surfactant imbibition experiments. The effects of surfactant types, clays, and pore size on oil recovery were analyzed.

The storage and transport mechanisms of oil in shale oil rocks is still a challenging problem. The hydrocarbons can be stored in inorganic pores, organic pores, and bulk kerogen (Huang et al.,

2020; Sang et al., 2018). The specific surface area, porosity, and permeability of shale rocks are significantly impacted by the total organic content (TOC). The contents of micropores and mesopores increase with the organic content (Tang et al., 2016). The content of hydrocarbon in kerogen increases with total organic content (Sang et al., 2018). However, the experimental method to accurately measure the hydrocarbon content in each major component of shale is still a difficult issue. Thus, we propose a new vacuum imbibition method to test the storage capacity of inorganic pores and organic matter in shale oil rocks. The mathematical models for vacuum imbibition experiments are derived.

CO_2 injection in shale is a feasible method for EOR and carbon storage. However, the mass transfer in shale oil reservoirs is still unclear due to the organic matter. Methane and CO_2 can adsorb and diffuse in the organic matter shale gas reservoirs (Etminan et al., 2014; Liu et al., 2019; Wang et al., 2018). However, there is very little research focusing on hydrocarbon and CO_2 mass transfer in shale oil reservoirs. Thus, I systematically explore the mass transfer mechanisms of hydrocarbon during CO_2 injection in shale rocks. Some new mass transfer models for CO_2 EOR in shale reservoirs are proposed. Those models are verified with experimental results from the literature.

2. Research Objectives

The objective of this dissertation was to solve the key issues in understanding EOR mechanisms in the Middle Bakken and shale rocks using surfactants and supercritical CO_2. The research scope of this dissertation was focused on the following aspects:

(1) Experimental and numerical studies of the mechanism of spontaneous imbibition in various rocks. Examine the oil recovery of the Middle Bakken cores from different surfactants using the spontaneous imbibition method.

(2) Studies of the storage mechanisms of water and oil in shale reservoirs. Evaluate the storage capacity of inorganic pores and organic matter.

(3) Investigate the diffusion and extraction mechanisms for CO_2 EOR in shale rocks. Mathematical modeling of miscible CO_2 EOR in shale. Verify the mass transfer models by matching mathematical models with experimental data.

3. Hypotheses

(1) The spontaneous imbibition is an important mechanism for the oil recovery of Middle Bakken rocks. Surfactant imbibition can improve the oil recovery of Middle Bakken samples. The types of surfactants will significantly impact oil recovery.

(2) The oil storage mechanisms in shale rocks may be tested using water and oil vacuum imbibition experiments. The exact oil volume in inorganic pores and organic matter can be obtained from vacuum imbibition experiments. The total organic carbon and thermal maturity might significantly impact the storage capacity of oil in organic matter.

(3) The CO_2 is an efficient solvent in extracting oil from inorganic pores and organic matter. The mass transfer in organic matter can be modeled by combining diffusion and extraction theories.

3. Dissertation Organization

This dissertation is composed of five chapters. The introduction is shown in Chapter I, which generally presents the motivations, objectives, hypotheses, and dissertation organization. Chapter II is a comprehensive review of enhanced oil recovery using surfactants and supercritical CO_2. Chapters III-V are based on published papers, of which I am the first author, about topics of EOR mechanisms of surfactants and miscible CO_2 injection. Chapter VI is conclusions and recommendations. A brief summary of each chapter is shown as follows:

Chapter II is a comprehensive review of recently published papers regarding EOR

mechanisms using surfactants and supercritical CO_2. Chapter III explores the mechanisms of water spontaneous imbibition in tight rocks. The relative permeability and capillary data are obtained from the imbibition experiments. In addition, spontaneous imbibition experiments are performed on the Middle Bakken rocks using various kinds of surfactants. Oil recovery is obtained from those experiments carried out at a high temperature condition. Chapter IV describes the mechanisms of storage and transport of water and oil storage in shale reservoirs using vacuum-imbibition method. The mathematical models of hydrocarbon flow and diffusion in shale rocks are proposed and matched with experiments. Chapter V investigates the mass transfer mechanisms and oil recovery of miscible CO_2 injection in shale oil reservoirs. Mathematical models of mass transfer between pores and bulk kerogen are proposed. Mathematical models for shale samples in spherical and cylindrical shapes are derived. Those models are matched with experimental results from the literature.

CHAPTER II

REVIEW OF THE APPLICATIONS OF SURFACTANTS AND SUPERCRITICAL CO_2 ENHANCED OIL RECOVERY

1. EOR Mechanisms of Surfactants.

Surfactant enhanced oil recovery is one of the most commonly used EOR methods to reduce the interfacial tension and to change the wettability. Surfactants are amphiphilic molecules, which have a hydrophilic portion and a hydrophobic portion. The hydrophilic part is soluble in water solution, and the hydrophobic part is insoluble in water (Belhaj et al., 2020).

1.1. Surfactants Used for EOR

1.1.1. Anionic Surfactants

Anionic surfactants have negative charges on the head groups when they are in water solution. Anionic surfactants are widely used chemicals for EOR due to their advantages, as shown following (1) easy to synthesize with low cost, (2) anionic surfactants have low adsorption on rocks due to the negative charges of minerals surface, (3) effectively reduce interfacial tension, (4) their high stability at high-temperature conditions (Belhaj et al., 2020). The anionic surfactants can be classified into carboxylate, sulfate, sulfonate, and phosphate (Negin et al., 2017). Carboxylate surfactants exhibit high stability and efficiency at high temperature and high salinity conditions with the existence of cations (Lu, 2014). Alkyl sulfates are commonly used surfactants, and their molecular structure is shown in Figure 2-1.

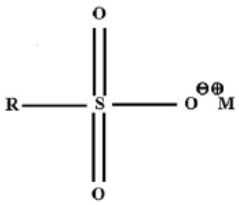

Figure 2-1 Molecular structure of an alkyl sulfate (Negin et al., 2017).

The “R” could be various hydrophobic hydrocarbon chains, and those hydrocarbon groups biodegrade really easily. The sulfate group enables the surfactant hydrophilic and soluble in the aqueous phase. Nevertheless, the sulfate group is sensitive to temperature, and the solubility of surfactants decreases with temperature. The sodium dodecyl sulfate (SDS) is one of the commonly used sulfate surfactants. The molecular structure of a Sodium Dodecyl Sulfate is shown in Figure 2-2.

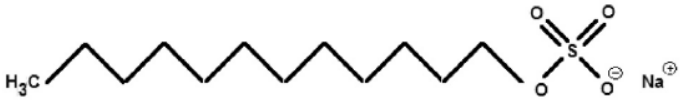

Figure 2-2 Molecular structure of SDS surfactant.

1.1.2. Nonionic Surfactants

Nonionic surfactants have no charge in aqueous solutions. They are commonly used to change the efficiency of other ionic surfactants. Nonionic surfactants have the advantage of high stability under high salinity conditions. However, their ability to reduce IFT is lower compared to ionic surfactants. A combination of anionic and nonionic surfactants is an efficient method to increase the stability in high salinity brine. The molecular structure for an alkyl ethoxy carboxylated is presented in Figure 2-3 (Negin et al., 2017). The ethoxy group forms the hydrogen bond with water. This mechanism enhances the iteration energy between surfactant and water, and reduces the IFT. The carboxylate group increases the stability of surfactants at high-temperature conditions.

$$RO(CH_2CH_2O)_xCH_2COO^-M^+$$

Figure 2-3 Molecular formula for alkyl ethoxy carboxylated. R is the alkyl group with a carbon number of C_8-C_{18}.

1.1.3. Cationic Surfactants

Cationic surfactants have positively charged tails. Cationic surfactants can dissociate in water solution and form an amphiphilic cation and an anion. Cationic surfactant is easy to be adsorbed on the negatively charged clay surface. Thus, the cationic surfactant has high efficiency in altering the wettability of the rock surface. Cationic surfactants have been identified as an efficient chemical to change the wettability and improve the oil recovery in carbonate rocks due to the negatively charged rock surface. However, the cationic surfactants are more expensive due to the high-pressure reaction condition in the synthesis process (Kumar et al., 2016).

1.1.4. Zwitterionic Surfactants

Zwitterionic surfactants contain a negatively charged tail and a positively charged tail. They have been widely used in the research of enhanced oil recovery due to their high water solubility, high stability under high salinity and temperature conditions, and remarkable interfacial activity (Zhong et al., 2019a). It has been reported that zwitterionic surfactants can significantly reduce the interfacial tension with a very low concentration of 50−3000 mg/L under a high salinity condition (Wang et al., 2010). Meanwhile, zwitterionic surfactants have good stability with other surfactants, such as ionic and nonionic surfactants. Using zwitterionic surfactants with other kinds of surfactants can improve their stability and strengthen their interfacial properties. Experimental results have shown that a synthesized zwitterionic surfactant can recover additional 27.03% of oil from rocks because it is able to change the wettability and interfacial tension (Kumar and Mandal, 2017).

1.2. Interfacial Tension

During the water flooding, the flow is a multiphase flow, and oil recovery is low because the oil can be trapped in pores. As the surfactants are injected into the oil reservoirs, the hydrophilic head is placed in water, and the hydrophobic tail contacts the crude oil. The concentration of surfactants on the interface is higher than in the bulk water phase. This process forms an adsorbed film due to the interactions between the crude oil, surfactants, and water (Gbadamosi et al., 2019). This mechanism can lead to a lower interfacial tension at the oil/water interface. The reduction of the interfacial tension at the interface can decrease the capillary force. The improved oil recovery mechanism of reducing interfacial tension is related to the remobilization of residual oil. The low interfacial tension allows the oil droplets to flow more easily in the pores. The N_{ca} is defined as the ratio of viscous force to capillary force as $N_{ca} = v\mu_w/\sigma_w$ (Guo et al., 2017). It has shown that the lower the interfacial tension, the higher the capillary number and oil recovery (Yuan et al., 2015).

1.3. Wettability Alteration

The wettability refers to the propensity or inclination of the surface at the presence of an immiscible fluid (Cheraghian, 2015; Mohammed and Babadagli, 2015). For the reservoir rock, the wettability of the rock surface largely impacts the location, distribution, and flow of the liquid (Alhammadi et al., 2017). The wettability of the reservoir is of significant importance because it impacts the oil recovery parameters, such as residual oil saturation, capillary pressure, and relative permeability curves. The wettability of reservoirs generally has three types: oil-wet, water-wet, and mixed-wet (Christensen and Tanino, 2017). The wettability properties of rock can be characterized by the contact angle, zeta potential, and surface imaging, etc. The contact angle measurement is the most commonly used method to identify the wettability of a solid surface. For

the oil phase, the surface is oil-wet as the contact angle is larger than 90°, and the surface is water wet as the contact angle is smaller than 90°. The wettability alteration from oil-wet to water-wet will decrease the capillary force and increase the oil relative permeability of the reservoir, as shown in Figure 2-4 (Gbadamosi et al., 2019; ShamsiJazeyi et al., 2014). Oil can be more easily recovered from water-water reservoirs than oil-wet reservoirs.

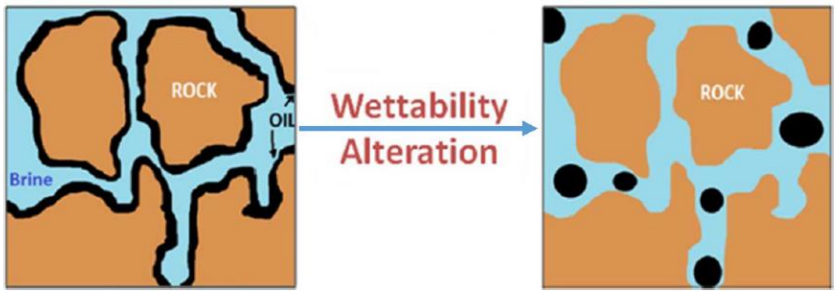

Figure 2-4 Schematic of improved permeability due to wettability alteration of rock from oil-wet to water-wet (ShamsiJazeyi et al., 2014).

Various kinds of surfactants have been widely used to alter the wettability and enhance the oil recovery in conventional and unconventional reservoirs (Alvarez and Schechter, 2017; Negin et al., 2017). The unconventional oil reservoirs typically have extremely low porosity, permeability, and oil recovery. The surfactants were reported to increase oil recovery by altering the matrix wettability and fluid flow behaviors in fractured reservoirs (Kathel and Mohanty, 2013; Mirchi et al., 2015). Meanwhile, spontaneous imbibition occurs in the fractured reservoirs. In this process, the wetting phase penetrates into the rock matrix and displaces the oil phase. Thus, the spontaneous imbibition in the reservoir rock enhances oil recovery. The surfactants have been widely used as chemical agents to enhance the oil recovery in conventional reservoirs, such as sandstone and carbonate reservoirs (Jarrahian et al., 2012; Salehi et al., 2008). An important mechanism of wettability alteration by surfactants is the cleaning mechanism that surfactants can remove the oil-

wet layer on the rock surface. This mechanism can alter the wettability of rock surfaces from oil-wet to water-wet. The cationic surfactants are preferentially used for carbonate reservoirs and anionic surfactants are usually used for sandstone rocks because of their charges (Esmaeilzadeh et al., 2011). The crude oil has negatively charged organic components, which can adsorb on the surface of positively charged minerals. The positively charged surfactants will reduce the adsorption of anionic components on rock surface due to the ion-pair formation interactions (Standnes and Austad, 2003). Thus, the crude oil is removed from the rock surface. Besides, desorption of the oleic phase from rock surface will alter the wettability from oil-wet to water-wet (Standnes et al., 2002; Standnes and Austad, 2003). The mechanism of this process is shown in Figure 2-5.

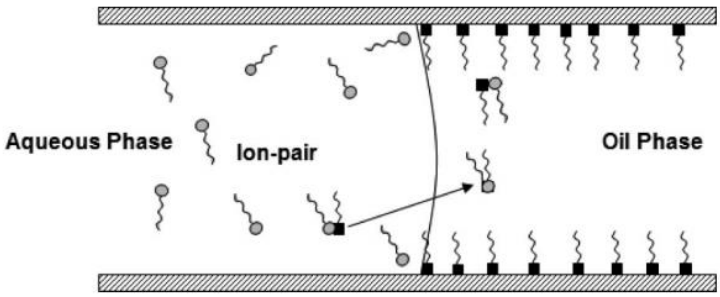

Figure 2-5 Schematic of wettability alteration mechanism by cationic surfactant (Salehi et al., 2008).

However, anionic surfactants are unable to detach the oleic phase from the rock surface due to their negative charges. Instead, the anionic surfactants can reduce the capillary forces due to the interaction between their hydrophobic tails and the oil phase (Hou et al., 2015). Moreover, the nonionic surfactants can be adsorbed on rock surface through the polarization of electrons and ion exchange. The cationic surfactants have high efficiency in altering the wettability of rock surfaces than anionic and nonionic surfactants. The wettability alteration of oil-wet sandstone and carbonate

rocks can be explained by the mechanism of polar interactions, surface precipitation, and acid/base interactions due to the adsorption of surfactants on negatively charged minerals (Hou et al., 2016).

2. EOR Mechanisms of Supercritical CO_2

2.1. Miscible and Immiscible EOR

The immiscible supercritical CO_2 enhanced oil recovery is dominated by oil swelling and viscosity reduction. CO_2 dissolution in the crude oil can result in a significant reduction in viscosity and an extraction effect for crude oil. Those effects improved the oil recovery (Perera et al., 2016). The solubility of CO_2 in crude oil is impacted by pressure, temperature, and oil gravity. The solubility of CO_2 increases with pressure and API gravity. However, it decreases with temperature. As the pressure is lower than the critical temperature, the oil composition, and liquefaction pressure also significantly impact the solubility (Emera and Sarma, 2007). Besides, the authors also developed correlations for CO_2 solubility in crude oil. The solubility correlations were derived under different temperature conditions.

For temperatures higher than the critical temperature:

$$S_{CO_2} = 2.238 - 0.33y + 3.23y^{0.6474} - 4.8y^{0.25656}$$

For temperatures lower than the critical temperature:

$$S_{CO_2} = 0.033 - 1.14y - 0.7716y^2 + 0.217y^2 - 0.02183y^4$$

where $y = \gamma(\frac{T^{0.8}}{P_s})\exp(\frac{1}{M})$, γ is the specific gravity, T is the temperature (°F), P_s is the saturation pressure (psi), P_{liq} is the CO_2 liquefaction pressure, M is molecular weight of crude oil, and S_{CO2} is solubility (mol/mol).

The miscible flooding occurs as the pressure is higher than the minimum miscibility pressure

(MMP). The main advantage of miscible CO_2 EOR is its high oil recovery. The mass transfer between CO_2 and crude oil is able to create a completely miscible zone in the oil reservoir with oil in the front and CO_2 in the back. CO_2 has a low miscibility pressure with light crude oil than other gases, such as N_2 and CH_4 (Zhang, 2016). The MMP of crude and CO_2 generally varies from 2500 psi to 3300 psi (Alfarge et al., 2017). Song et al. (2013) conducted laboratory studies of water, immiscible, and miscible CO_2 injection for Bakken rocks (Song and Yang, 2013). Their results show that water flooding has a higher oil recovery than immiscible CO_2 Huff-n-Puff. However, the miscible CO_2 Huff-n-Puff has a much higher oil recovery. Hawthrone et al. (2013; 2019b) experimentally investigated the oil recovery from Bakken tight and shale rocks (Hawthorne et al., 2019b, 2013). They proposed that the diffusion process is the main mechanism for miscible CO_2 enhanced oil recovery from fractured tight and shale reservoirs. Alharthy et al. (2015) experimentally investigated the oil recovery in Bakken rocks from different types of gases, such as C_1-C_2, N_2, and CO_2 (Alharthy et al., 2018). Their results suggested that the oil recovery in the Middle Bakken cores could be 90%. However, the oil recovery is approximately 40% for Upper and Lower Bakken shale samples.

2.2. Flooding and Huff-n-Puff

2.2.1. CO_2 Huff-n-Puff

CO_2 huff-n-puff is a widely used method to improve the oil recovery in tight and shale reservoirs (Li et al., 2017; Zhang et al., 2018). The CO_2 can be dissolved in crude oil and result in swelling and viscosity reduction effects under reservoir conditions. Huff-n-puff processes use one well as injection well and production well. There are mainly three stages: gas injection stage, soaking stage, and the production stage.

The CO_2 huff-n-puff method has been applied to EOR for unconventional rocks in the past decade. Fakher and Imqam (2020) experimental studies the oil recovery of shale rocks using the CO_2 cyclic injection method (Fakher and Imqam, 2020). They concluded that oil recovery increases with injection pressure and temperature. However, the increasing temperature reduces the CO_2 adsorption capacity on shale rocks. Li et al. (2019) explored the CO_2 EOR on shale cores by combining huff-n-puff experiments and nuclear magnetic resonance methods (Li et al., 2019). Results suggested that fractures can significantly increase oil recovery, and the recovered oil in the first cycle is primarily from macro and mesopores. In order to increase the stability of CO_2 huff-n-puff, the cosolvents were added. Gong et al. (2020) used ethanol as a cosolvent in CO_2 cyclic injection (Gong et al., 2020). Their results suggest that the CO_2/ethanol has better performance on EOR than pure CO_2. The ethanol enhances oil recovery by reducing the interfacial tension and accelerating the CO_2 diffusion in the oil phase.

2.2.2 CO_2 Flooding

CO_2 injection processes have different types of injection patterns such as continuous CO_2 injection, CO_2 flooding coupled with a soaking period, and CO_2 flooding coupled with pressure maintenance (Zhou et al., 2019). Chen et al. (2018) performed flooding experiments on different low permeability rocks using water, surfactant solution, CO_2, and nitrogen (Chen et al., 2018). The CO_2 flooding yields the highest oil recovery, followed by nitrogen, surfactant, and water. Zhu et al. (2020) conducted miscible CO_2 flooding experiments on different shale and sandstone rocks (Zhu et al., 2020). The fluid distribution was measured using the NMR method. Their results show that the porosity of immobile oil is lower than free oil in shale rocks. The oil recovery in sandstone is much higher than that in shale rocks. The oil recovery process in shale rocks is slow due to the adsorbed immobile oil on clay and organic matter. Zhang (2016) performed miscible flooding

experiments and simulation on different Bakken tight rocks with an average porosity of 7.5% and permeability of 0.0018mD (Zhang, 2016). The results indicated that the oil recovery was higher than 70%. The numerical model suggested that the vaporization of light hydrocarbon components into CO_2 is a major recovery mechanism.

CHAPTER III

SPONTANEOUS IMBIBITION AND OIL RECOVERY FROM SURFACTANTS SPONTANEOUS IMBIBITION FOR TIGHT ROCKS

1. Introduction

In the fractured reservoirs, imbibition is an important process to improve oil and gas recovery from the matrix (Mirzaei-Paiaman, 2015; Standnes, 2004). The spontaneous imbibition mechanisms in rock and coal are key issues that need to be focused upon to improve recovery in the development of the tight oil (Olatunji et al., 2018; Wang and Sheng, 2018), shale and tight gas (Lai et al., 2019; Xu et al., 2018; Yang et al., 2017), and coalbed methane (Shen et al., 2018; Wu et al., 2018). Spontaneous imbibition is the process of a wetting phase displacing a non-wetting phase in a porous media in the presence of capillary pressure. Depending upon the flow directions of wetting and non-wetting phases, spontaneous imbibition can be divided into co-current imbibition and counter-current imbibition. Assuming that a rock sample is water-wet, co-current imbibition occurs when the water and oil flow in the same direction through the inlet, whereas counter-current imbibition occurs as the water and oil flow in opposite directions (Alyafei and Blunt, 2018; Foley et al., 2017). Some experiments and numerical studies show that the recovery rate and displacement efficiency of co-current are much higher than those of counter-current (Chen et al., 2003; Pooladi-Darvish and Firoozabadi, 2000). However, counter-current spontaneous imbibition is normally regarded as the dominated imbibition mechanism in fractured reservoirs (Haugen et al., 2014; Mattax and Kyte, 1962; Xu et al., 2017).

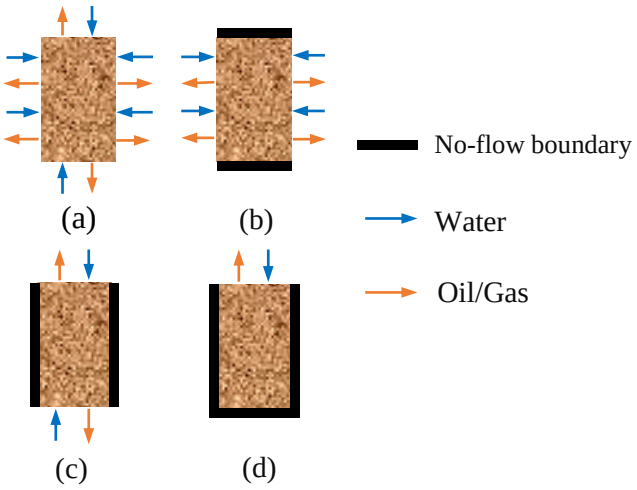

Figure 3-1 Schematic of four boundary conditions: (a) all faces open (AFO); (b) two ends closed (TEC); (c) two ends open (TEO); (d) one end open (OEO).

For counter-current spontaneous imbibition, a pre-saturated core plug is submerged in water. Depending upon boundary conditions of a core plug, there are several kinds of counter-current spontaneous imbibition: (1) all faces open (AFO), (2) two ends closed (TEC), (3) two ends open (TEO), and (4) one end open (OEO). The schematic of four kinds of spontaneous imbibition are presented in Figure 3-1. Boundary conditions have great impacts on imbibition performances (Yildiz et al., 2006). AFO is a commonly used method in spontaneous imbibition experiments because it is the easiest to conduct and with highest recovery rate (Lyu et al., 2019; Mason et al., 2009). However, the flow patterns of the AFO boundary condition are complicated due to the coexistence of co-current and counter-current flow through the inlets. Therefore, the established mathematical models cannot be applied to AFO imbibition (Mason and Morrow, 2013). Boundary conditions will impact contact surface between core and water and have significant effects on recovery rate. Cheng et al. (2018) and Lyu et al. (2019) demonstrated that the AFO imbibition has the highest recovery rate and TEO has the lowest recovery rate. However, boundary conditions

have negligible impact on the ultimate recovery factor (Standnes, 2004; Yildiz et al., 2006). In addition, other factors, such as permeability, relative permeability, capillary pressure, initial water saturation, fluid viscosity, interfacial tension, and wettability, also have effects on the imbibition process (Graue and Fernø, 2011; Jing et al., 2019; Pan et al., 2018; Qin et al., 2019, 2017).

The spontaneous imbibition is usually modeled by a set of differential equations. The solutions of those equations require functions of capillary pressure and relative permeability to the wetting phase and non-wetting phase. Matching of a mathematical model with the experimental results is a new method to obtain relative permeability and capillary pressure. Li et al. (2006) performed spontaneous imbibition simulation with the OEO boundary condition (Li et al., 2006). They derived a mathematical model without considering the gravity effect. Then the brine/air capillary pressure and relative permeability were obtained by matching the model with experiments. Schmid et al. (2011) derived a set of semianalytical solutions for one-dimensional imbibition (Schmid et al., 2011). In order to derive the analytical solutions, the water front position was obtained experimentally as a function of square root of time. Alyafei et al. (2016) and Schmid et al. (2016) derived a closed form of analytical solutions for spontaneous imbibition based on fractional flow theory (Alyafei et al., 2016; Schmid et al., 2016). Mathematical models are important in order to understand the mechanisms of spontaneous imbibition. Haugen et al. 2014) proposed models to scale relative permeability and capillary pressure for imbibition of cores with TEC and OEO boundary conditions (Haugen et al., 2014). Alyafei and Blunt (2018) conducted one-dimensional water co-current imbibition on sandstones and obtained the relative permeability and capillary pressure (Alyafei and Blunt, 2018). While there have been various models focusing on linear imbibition, there are very few research studies about modeling imbibition with complex boundary conditions such as TEC and AFO. Besides, the gravity effects on spontaneous imbibition

have not been well studied.

Recently, low-field nuclear magnetic resonance (NMR) techniques were introduced to analyze the spontaneous imbibition to observe fluid distribution and core petrophysical properties. NMR transverse relaxation time (T_2) of the saturated cores can be converted into pore size distribution, porosity, and fluid distribution at the pore scale (Lyu et al., 2019; Prather et al., 2016; Song et al., 2015). Ling et al. (2017) used NMR T_2 to monitor the oil saturation changes behind spontaneous imbibition front (Liang et al., 2017). Their results indicated that the smaller the average pore size the more rapid the saturation changes behind imbibition front. Cheng et al. (2018) investigated the residual oil distribution for oil/water displacement using spontaneous imbibition combined with NMR and MRI technologies (Cheng et al., 2018). Their results demonstrated that oil in micropores is preferentially expelled by water due to high capillary pressure. Another important implication of NMR is to detect the movable fluid distribution. Lyu et al. (2018) studied the movable water distribution in tight rocks using the centrifugal method. Their results show the movable fluid is controlled by pore size and the connectivity between pores (Lyu et al., 2018). Gao and Li (2015) measured movable fluid percentage for different cores and concluded the movable fluid percentage goes higher as the permeability increases (Gao and Li, 2015). NMR provides a fast and nondestructive technique and has become a common experimental method in imbibition interpretation and analysis of core properties.

Tight oil and gas are becoming an increasingly important energy sources in North America. Bakken formation is one of the largest unconventional reservoirs with respect to its oil and gas reserves. The Middle Bakken Formation mainly consists of limestone and sandstone. The Upper and Lower Bakken members are tight shale which are the sources of hydrocarbons in the Middle Bakken member. Productivity of the Middle Bakken formation is becoming increasingly higher

with the application of multistage hydraulic fracturing and horizontal drilling. However, the recovery factors of the reservoirs are still low due to the extremely low permeability and porosity.

Recently, many studies have demonstrated that the Middle Bakken member is a typical tight layer with ultralow porosity (Sonnenberg and Pramudito, 2009). The measured size of the microstructures was found to vary from nanometer to micrometer and typically includes some natural fractures (Liu et al., 2018; Zhang et al., 2019b). In addition, Cho et al. (2016) analyzed the pore size distributions of Bakken rocks (Cho et al., 2016). The results indicated that the Middle Bakken samples show both unimodal and bimodal pore size distribution curves. In addition, they studied mineralogical composition using X-Ray diffraction (XRD) technology. The results demonstrated that the dominant minerals are quartz followed by dolomite and calcite.

In addition, the enhanced oil recovery technologies are of great interest to both academia and petroleum industry due to the low oil recovery of tight formations. Surfactant is one of the most commonly chemicals in unconventional reservoir EOR process. The surfactant can adsorb onto the rock surface and change the wettability of rock from oil-wet to water-wet. Surfactants are amphiphilic compounds that have both hydrophobic and hydrophilic groups, which can effectively change the wettability of the rock surfaces and reduce the oil-water IFT (Liu et al., 2019). In the fractured reservoirs, imbibition is a crucial process to enhance oil recovery from the matrix (Mirzaei-Paiaman, 2015; Morrow and Mason, 2001). Spontaneous imbibition is the process of a wetting phase displacing a non-wetting phase in the presence of capillary pressure. Counter-current spontaneous imbibition is the most important imbibition type in fractured reservoirs (Haugen et al., 2014; Mattax and Kyte, 1962; Xu et al., 2017). Thus, the spontaneous imbibition mechanisms in rock are key issues that need to be focused upon to improve recovery of the tight oil (Wang and Sheng, 2018). Recently, many studies confirm that surfactant can significantly improve oil

recovery by use of surfactant imbibition. Wang et al. (2014) performed spontaneous imbibition experiments on Bakken rocks using different types of surfactants including anionic and nonionic surfactants (Wang et al., 2014). Their results demonstrated that a nonionic surfactant (SNA) can significantly improve oil recovery. Olatunji et al. (2018) conducted surfactant imbibition experiments on Middle Bakken rocks (Olatunji et al., 2018). Their results indicated that the oil recovery was low during brine imbibition, whereas surfactant solutions recovered approximately 30–45% of the oil.

In this work, we experimentally and numerically explored the spontaneous imbibition with OEO and TEC boundary conditions. Accurate experiments of brine imbibing into air-filled cores were carried out with continuous recording of mass changes using a high precision balance. The pore size distribution and fluid distribution in cores were obtained from the NMR method. Furthermore, new methods to determine capillary force and relative permeability were proposed by matching mathematical models with spontaneous imbibition experiments with OEO and TEC boundary conditions.

Even there have been many studies related to improve oil recovery by applying different surfactants. There are very few studies that consider the effects of pore structure and mineralogical composition on surfactant EOR process. Thus, spontaneous imbibition experiments with different surfactants solutions and brine were carried out on Bakken and Berea rock samples. The microstructures and pore size distributions of Bakken samples were obtained from SEM and nitrogen adsorption methods. In addition, the mineralogical compositions of samples were obtained from XRD method. Effects of pore size distribution, mineralogy, and surfactants on oil recovery were analyzed.

2. Experimental Procedures

2.1. Rocks and Fluids

Eight core plugs were selected to conduct spontaneous imbibition experiments. Four Bakken cores were obtained from the Middle Member of the Bakken Formation in North Dakota, USA. Four Berea cores were cut from outcrops in Cleveland Quarries, Ohio, USA. All of those core plugs were drilled perpendicular to bedding. The XRD mineralogical analysis using X-ray diffraction (XRD) was conducted for the core samples and are shown in Table 3-1.

Table 3-1 Mineralogical composition of Berea and Bakken samples

Samples	Kaolonite (wt %)	Illite (wt %)	Chlorite (wt %)	Quartz (wt %)	Calcite (wt %)	Dolomite (wt %)	Feldspar (wt %)	Pyrite (wt %)	Halite (wt %)
Berea cores	5			88		2	5		
Bakken1		9	3	39	10	22	15	1	1
Bakken2									
Bakken3		11	4	38	14	15	15	2	1
Bakken4									

As indicated in Table 3-1, the dominant mineral of Berea cores is quartz. However, the major minerals of the Middle Bakken samples are quartz, dolomite, feldspar, and calcite. Middle Bakken cores are light gray limestone. Berea cores are fine-grained, clay-cemented quartz sandstone. Core sample preparation includes extracting cores with toluene and ethanol and drying core samples in an oven at 105°C. After the cleaning and drying of core samples, routine analysis such as measuring mass, diameter length, helium porosity, and helium permeability was performed. The petrophysical properties of those samples are presented in Table 3-2.

Table 3-2 Summary of the petrophysical properties of core plugs

Samples	Diameter (cm)	Length (cm)	Permeability (mD)	Porosity (%)
Bakken1	3.78	2.12	0.49	8.4
Bakken2	3.79	3.15	7.80	5.1
Bakken3	3.78	1.86	8.00	3.6
Bakken4	3.77	4.29	0.13	4.9
Berea1	3.94	5.08	99.8	22.1
Berea2	3.90	4.91	80.4	23.4
Berea3	3.95	4.55	10.7	23.1
Berea4	3.96	4.61	61.2	23.8

As shown in Table 3-2, Middle Bakken samples are tight rocks and have lower porosity and permeability than Berea samples. All experiments were conducted at ambient conditions, 23 °C and atmospheric pressure (100 KPa). The brine solution is 1wt% NaCl and 1wt% KCl to prevent the swelling problem. The density of brine is 1.011 g/cm^3 and its viscosity is 0.896 mPa·s (Zhang and Han, 1996). The air density is 0.0012 g/cm^3 and its viscosity is 0.018 mPa·s (Lemmon and Jacobsen, 2004).

2.2. Imbibition Experiments

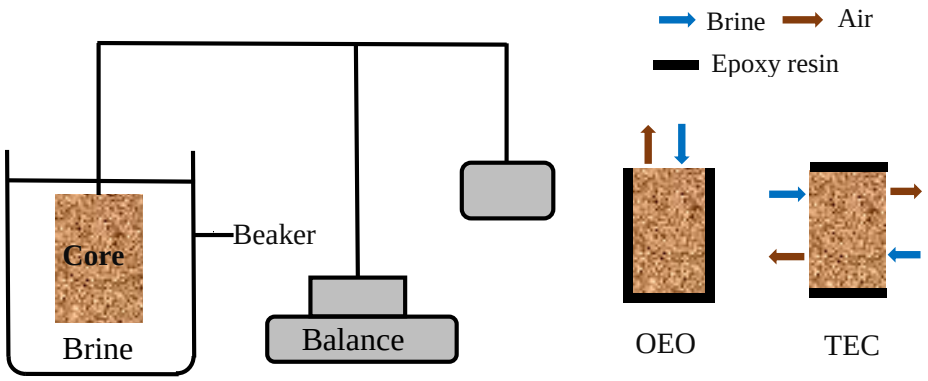

Figure 3-2 Schematic of the experimental setup.

The schematic of the experimental apparatus is presented in Figure 3-2. The mass of core samples is continuously recorded using a high precision balance with 0.001g accuracy. Archimedes' principle shows that the magnitude of the buoyant force in the core plug is equal to the weight of the brine it displaces, which is a constant. It can be verified that the increase of the mass equals the mass of the brine that is imbibed into the core minus the mass of the air displaced out of the core. Two sets of experiments with different boundary conditions were carried out. In the first set, one end open (OEO) spontaneous imbibition experiments were conducted on core plugs Bakken1, Bakken4, Berea3, and Berea4. In the second set, two ends closed (TEC) imbibition experiments were performed on cores Bakken2, Bakken3, Berea1, and Berea2. To ensure that only counter-current imbibition occurred, core plugs were sealed with epoxy resin. For OEO imbibition, the bottom face and cylindrical surface were sealed with epoxy resin. For TEC imbibition, the top and bottom faces of cores were sealed with epoxy resin.

2.3. NMR Experiments

The nuclear magnetic resonance (NMR) tests for cores at fully brine-saturated conditions (or pre imbibition) and after imbibition conditions were carried out. The experiments include following steps: (1) The ZYB-II Vacuum Saturation Device was used to vacuum the cores for 24 hours and then saturating cores with brine at 20 MPa for seven days. Then the mass of the cores were measured. (2) Raw NMR data of 100% brine-saturated cores were measured. (3) The cores were dried in an oven at 105℃. (4) Brine imbibition experiments with different boundary conditions were performed. (5) NMR T_2 distributions of Berea and Bakken samples were measured as imbibition experiments completed. NMR measurements were carried out with low field (2 MHz) NMR equipment (Oxford Instruments Geospec2 Rock Core Analyzer). NMR measurements were

conducted with an in-built Oxford Instruments pre-emphasis testing EDDYCM pulse sequence (Bush, 2019). The NMR measurement parameters for Bakken samples are as follows: 150 *ms* waiting time, 4600 number of echoes, 200 μs echo time and 64 number of scans. The NMR measurement parameters for Berea samples are as follows: 1500 *ms* waiting time, 66700 number of echoes, 100 μs echo time, and 64 number of scans. The laboratory temperature and magnet temperature of NMR spectrometer were 23 °C and 20 °C, respectively.

3. Imbibition Models

3.1. OEO Spontaneous Imbibition

Counter-current imbibition with OEO boundary condition is a one-dimensional flow. Although air is compressible, the experiments were conducted at atmospheric pressure. The air is compressed at the short initial period of spontaneous imbibition (Li et al., 2006). Pressure change in the air phase is negligible, with little or no air volume change (Alyafei et al., 2016). Thus, incompressible flow in a homogeneous porous media is assumed. The wetting phase (water) conservation equation can be written as

$$\frac{\partial v_w}{\partial x} = -\phi \frac{\partial S_w}{\partial t} \tag{3.1}$$

Considering the experimental setup in this paper, gravity is regarded as driving force. The Darcy velocity of wetting phase is

$$v_w = \frac{k k_{rw}}{\mu_w}\left(-\frac{\partial P_w}{\partial x} + g\rho_w\right) \tag{3.2}$$

The Darcy velocity of non-wetting phase (air) is

$$v_g = \frac{k k_{rg}}{\mu_g}\left(-\frac{\partial P_g}{\partial x} + g\rho_g\right) \tag{3.3}$$

For counter-current spontaneous imbibition, total flow rate of water and air is zero.

$$v_w + v_g = 0 \tag{3.4}$$

The mobility of water and gas can be expressed as $\lambda_w = k_{rw}/\mu_w$ and $\lambda_g = k_{rg}/\mu_g$, respectively. Combining Eq. (3.2) and Eq. (3.4), the water velocity is rewritten as

$$v_w = \frac{k\lambda_w\lambda_g}{\lambda_w + \lambda_g}[\frac{\partial P_c}{\partial x} + (\rho_w - \rho_g)g] \tag{3.5}$$

Substituting Eq. (3.5) into Eq. (3.1) yields

$$\frac{\partial}{\partial x}[\frac{k\lambda_w\lambda_g}{\lambda_w + \lambda_g}\frac{\partial P_c}{\partial x} + \frac{k\lambda_w\lambda_g}{\lambda_w + \lambda_g}(\rho_w - \rho_g)g] = -\phi\frac{\partial S_w}{\partial t} \tag{3.6}$$

The capillary pressure is $Pc = Pg - Pw$ and a function of water saturation.

Eq. (3.6) can be rewritten as

$$\frac{\partial}{\partial x}[D_{sw}\frac{\partial S_w}{\partial x} + G_{sw}(\rho_w - \rho_g)g] = -\phi\frac{\partial S_w}{\partial t} \tag{3.7}$$

where D_{sw} and G_{sw} denote nonlinear coefficients due to the capillary pressure and gravity.

$$D_{Sw} = \frac{k\lambda_w\lambda_g}{\lambda_w + \lambda_g}\frac{dp_c}{dS_w} \tag{3.8}$$

$$G_{sw} = \frac{k\lambda_w\lambda_g}{\lambda_w + \lambda_g} \tag{3.9}$$

Eq. (3.7) is the governing equation of OEO counter-current spontaneous imbibition. If the gravity is negligible, Eq. (3.7) is simplified as

$$\frac{\partial}{\partial x}[D_{sw}\frac{\partial S_w}{\partial x}] = -\phi\frac{\partial S_w}{\partial t} \tag{3.10}$$

The boundary conditions are given as

$$S_w(x = 0, t) = S_{w,\max} \tag{3.11}$$

$$\left.\frac{\partial S_w}{\partial x}\right|_{x=L} = 0 \tag{3.12}$$

The initial conditions are expressed as

$$S_w(x, t=0) = S_{wi} \tag{3.13}$$

where $S_{w,\,max}$ is the maximum water saturation, S_{wi} is the initial water saturation, and L is the length of the core plug.

Both numerical and analytical methods are capable of obtaining the solutions of Eq. (3.10) by matching model results with the specific experiments (Alyafei et al., 2016; Foley et al., 2017; Li et al., 2006). However, there is no known exact solution of nonlinear Eq. (3.7), which considers gravity effect. Thus, the finite difference method was used to obtain the numerical solutions. The time steps and grid spacing need to be small in order to minimize the error. In this paper, a time step of 2 seconds and a grid spacing of 0.1 *mm* were used to accurately capture the water imbibing into cores.

3.2. TEC Spontaneous Imbibition

Considering the experimental setup in this paper, the TEC counter-current imbibition is a horizontal radial flow. The water conservation equation is expressed as

$$\frac{1}{r}\frac{\partial}{\partial r}(rv) = -\frac{\partial}{\partial t}(\phi S_w) \tag{3.14}$$

Water phase Darcy velocity is

$$v_w = -\frac{kk_{rw}}{\mu_w}\frac{\partial P_w}{\partial r} \tag{3.15}$$

Gas phase (air) Darcy velocity is

$$v_g = -\frac{kk_{rg}}{\mu_g}\frac{\partial P_g}{\partial r} \tag{3.16}$$

Combining Eqs. (3.15), (3.16), and (3.4), the water velocity is rewritten as

$$v_w = \frac{k\lambda_w\lambda_g}{\lambda_w + \lambda_g}\frac{\partial P_c}{\partial r} \tag{3.17}$$

Substituting Eq. (3.17) into Eq. (3.14) yields

$$\frac{1}{r}\frac{\partial}{\partial r}(rD_{sw}\frac{\partial S_w}{\partial r}) = -\phi\frac{\partial S_w}{\partial t} \tag{3.18}$$

where D_{sw} is a nonlinear coefficient shown in Eq. (3.8).

The boundary conditions are shown as

$$S_w(r = r_e, t) = S_{w,\max} \tag{3.19}$$

$$\left.\frac{\partial S_w}{\partial x}\right|_{r=0} = 0 \tag{3.20}$$

The initial condition is written as

$$S_w(r, t = 0) = S_{wi} \tag{3.21}$$

where r_e is the radius of the core plug.

Eq. (3.18) is the governing equation of TEC counter-current spontaneous imbibition. The finite difference method was used to obtain the numerical solutions. In order to capture the significant water saturation change at the imbibition front, it is necessary to define smaller grids at the core plug center. One method is to use non-uniform grids that grid spacing increases exponentially and transform cylindrical coordinate into Cartesian coordinate. In this paper, the space size is 0.1 *mm* in Cartesian coordinate and the time step is 2 seconds.

3.3. Capillary Pressure and Relative Permeability

In this paper, a power law was used for relative permeability curve. Other models such as Brook-Corey and Van Genuchten models could also be used (Schmid et al., 2016, 2011). However,

the power law is a simple and most commonly used model in the modelling of spontaneous imbibition (Alyafei et al., 2016; Wang and Sheng, 2018). The power law could be written as

$$k_{rw} = k_{rw,\max}\left(\frac{S_w - S_{wi}}{1 - S_{wi} - S_{gr}}\right)^{N_{Krw}} \tag{3.22}$$

$$k_{rg} = k_{rg,\max}\left(\frac{1 - S_w - S_{gr}}{1 - S_{wi} - S_{gr}}\right)^{N_{Krg}} \tag{3.23}$$

where k_{rw} is the water relative permeability, $k_{rw,max}$ is the maximum water relative permeability, S_w is the water saturation, S_{wi} is the initial water saturation, S_{gr} is the residual gas saturation, N_{Krw} is the water relative permeability exponent, k_{rg} is the gas relative permeability, $k_{rg,max}$ is the maximum gas relative permeability, and N_{Krg} is the gas relative permeability exponent.

A power law can be used to express the capillary pressure as shown in following form (Alyafei et al., 2016)

$$p_c = p_{c,entry}\left(\frac{S_w - S_{wi}}{1 - S_{wi} - S_{gr}}\right)^{N_{Pc}} \tag{3.24}$$

where $P_{c,entry}$ is the entry capillary, S_w is the water saturation, S_{wi} is the initial water saturation, S_{gr} is the residual gas saturation, and N_{pc} is the capillary pressure exponent.

This power law has an intrinsic flaw for numerical method. At the imbibition front, S_w goes to S_{wi} and the capillary pressure goes to infinity. The power law does not make physical sense and dpc/dSw in Eq. (3.8) does not exist. Thus, we assume an exponential form for capillary pressure

$$p_c = p_{c,\max}\exp\left[-b\left(\frac{S_w - S_{wi}}{1 - S_{wi} - S_{gr}}\right)\right] \tag{3.25}$$

where $p_{c,max}$ is the maximum capillary pressure, S_w is the water saturation, S_{wi} is the initial water saturation, S_{gr} is the residual gas saturation, and β is a capillary pressure exponent.

The water saturation can be obtained by solving Eqs. (3.7), (3.10), and (3.18) numerically.

The imbibed water volume can be calculated by integrating water saturation within the core. We adjusted the following parameters: $k_{rw,max}$, N_{Krw}, $k_{rg,max}$, N_{Krg}, $p_{c,max}$, and β to the match between the numerical solutions and experimental results.

4. Results and Discussion

4.1. NMR Pore Size and Fluid Distribution

An important application of NMR T_2 analysis is to transform NMR T_2 into pore size distribution (PSD). NMR T_2 response can be converted to pore size using the following equation (Dunn et al., 2002; Liu et al., 2018; Yao et al., 2010; Yuan et al., 2018)

$$\frac{1}{T_2} = \rho\left(\frac{S}{V}\right)_{pore} = \rho\frac{c}{R} \tag{3.26}$$

where ρ is the surface relaxivity, S/V is the ratio of pore surface area to the pore volume, and R is the pore radius. C is 1, 2 and 3 for planar, cylindrical and spherical pores, respectively. In this paper, pores are assumed to be cylinder and C is 2. Eq. (3.26) shows the smaller the pore the shorter the NMR relaxation time.

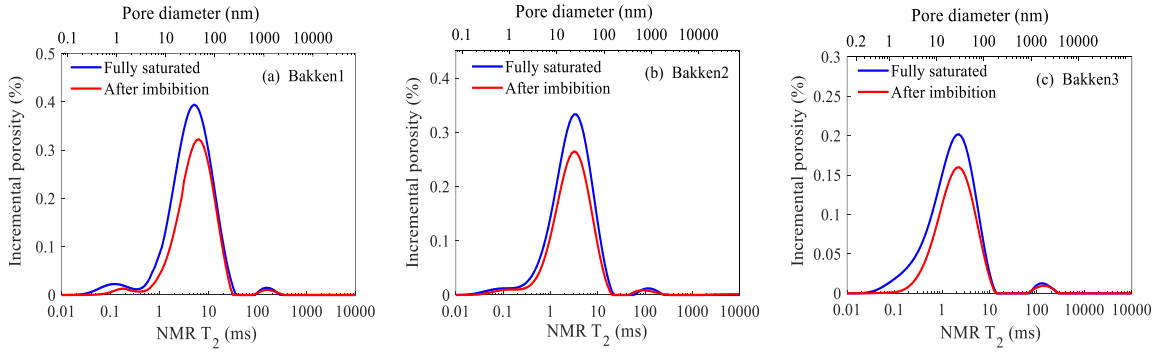

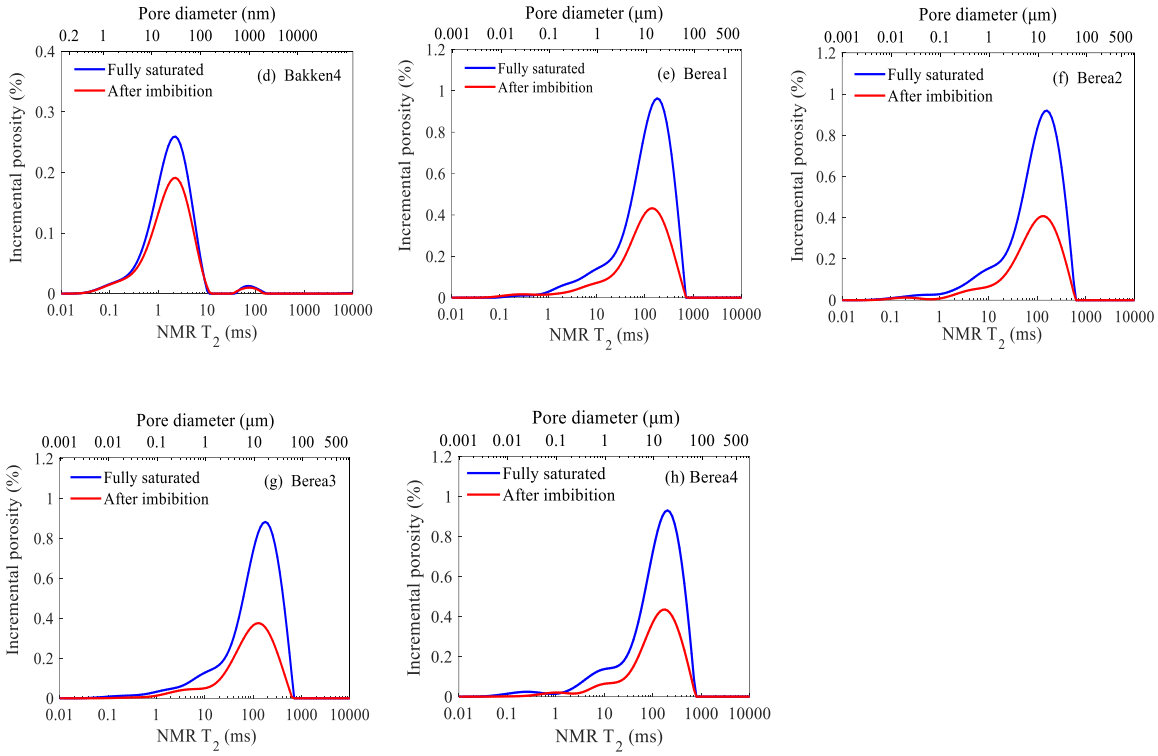

Figure 3-3 NMR T_2 and pore size distribution for Middle Bakken and Berea cores.

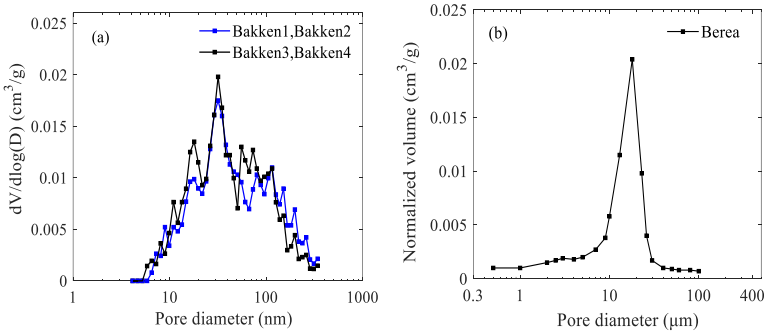

Figure 3-4 Pore size distribution of samples. (a) Middle Bakken samples from nitrogen adsorption;(b) Berea samples from mercury intrusion by Cardoso and Balaban (2015.

The pore size and T_2 distribution for Middle Bakken and Berea cores are presented in Figure 3-3. Two common features can be seen from the T_2 distribution. First, the signal of NMR T_2 shows a unimodal pattern. Second, the NMR T_2 signal after brine imbibition is much lower than when

the core is fully brine-saturated.

In order to calculate NMR pore size distribution, the surface relaxivity should be calculated by comparing NMR T_2 distribution with PSD obtained from nitrogen adsorption or mercury intrusion. The peak of PSD measured from mercury intrusion is approximately proportional to the peak of T_2 distribution measured from NMR (Minagawa et al., 2008). The equation is expressed as

$$R_{peak} = \rho c T_{2,peak} \tag{3.27}$$

where R_{peak} is the peak of PSD from mercury intrusion or nitrogen adsorption, $T_{2,peak}$ is the peak of NMR T_2 distribution.

Nitrogen gas adsorption is able to detect micro (<2 nm) to mesopores (2-50 nm), while mercury intrusion is capable of characterizing meso to macropores (>50 nm). The PSD of Berea outcrop samples is shown in Figure 3-4b reported by Cardoso and Balaban (Cardoso and Balaban, 2015). The Rpeak of the pore diameter distribution is 18 μm. The surface relaxivity of Berea samples calculated from Eq. (3.27) is 23.7 μm/s. However, the Middle Bakken is tight formation and most of its pores are mesopores. Nitrogen adsorption is a common method to analyze tight formation PSD (Sang et al., 2018; Wang et al., 2017, 2016). The PSD obtained from nitrogen adsorption method can be used to calculate NMR surface relaxivity of tight rocks (Saidian and Prasad, 2015; Yuan et al., 2018). The PSD of Bakken samples were measured using the nitrogen adsorption method (Figure 3-4a). Bakken1 and Bakken2 were obtained from the same depth and Bakken3 and Bakken4 were obtained from another depth. The surface relaxivities of Bakken samples were calculated by matching Rpeak from N2 adsorption with T2, peak from NMR. The surface relaxivity is 3.4 μm/s for Bakken3 and Bakken4. The surface relaxivity is 1.8 μm/s for Bakken1 and Bakken2. After the surface relaxivities were obtained, NMR transformed pore size

was calculated using Eq. (3.27). Surface relaxivities of Berea and Middle Bakken cores are strikingly different. This significant difference can be attributed to NMR measurement parameters. NMR settings such as spectrometer frequency, waiting time, and the temperature have significant impacts on surface relaxivity (Godefroy et al., 2002; Xu et al., 2015). The surface relaxivities differences between Middle Bakken samples are due to their mineralogical composition. The types and contents of paramagnetic minerals such as Fe-bearing chlorite, pyrite, and siderite have impacts on surface relaxivity (Yuan and Rezaee, 2019). Samples Bakken3 and Bakken4 have larger surface relaxivities than Bakken1 and Bakken2 due to their high contents of paramagnetic minerals, chlorite and pyrite shown in Table 3-1.

As presented in Figure 3-3, NMR pore diameters of Bakken cores range from 0.3 nm to 200 nm. Bakken samples are dominated by mesopores with only a small percentage of micropores and macrpores. In addition, the pore diameter differences between Bakken samples are small. Those results are close with the Middle Bakken PSD from the mercury injection method by using unimodal PSD (Cho et al., 2016). However, PSD from transformed NMR show that Bakken samples exhibit a common feature that small content of water is present in fractures with width ranges from 0.6 to 2 μm. This is because the Middle Bakken formation has a large numbers of natural fractures. The nitrogen adsorption method is probably not capable of detecting those fractures. Because the samples used for nitrogen adsorption were crushed into 60-100 mesh fragment. The crushing process probably destroyed large fractures. For Bakken samples, NMR T_2 after imbibition indicates that water is capable of entering into the pores (1-200 nm) and fractures (0.6-2 μm). Both Bakken and Berea samples show a common feature that PSD curves are unimodal. The main difference is that Berea cores are dominated by macropores with diameters range from 0.1- 60 μm which are much larger than the pores sizes of Bakken samples.

4.2. OEO Imbibition

The OEO imbibition is a linear imbibition. Considering the experimental setup, the gravity was considered in the mathematical model (Eq. (3.7)). The recovery factor F can be calculated from the following equation

$$F = 1 - \frac{m}{(\rho_w - \rho_g)\phi} \tag{3.28}$$

where m is the mass change of the core, ρ_w is brine density, ρ_g is air density, and $\emptyset$ is core porosity.

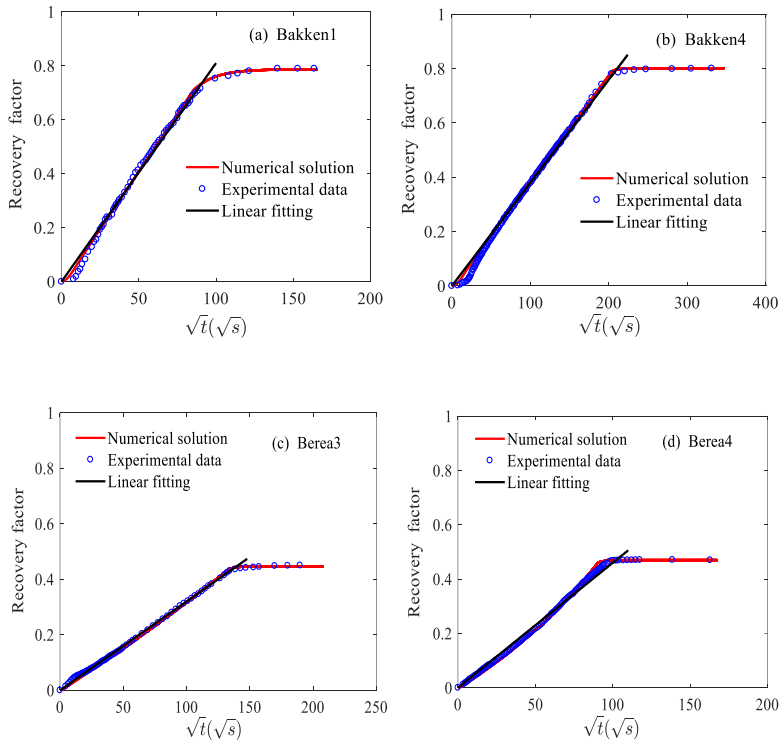

Figure 3-5 Recovery factors of OEO spontaneous imbibition as a function of $\sqrt{t}$.

Table 3-3 Parameters for imbibition history matching and linear fitting

Samples	Sw_{max}	Krw_{max}	N_{Krw}	Krg_{max}	N_{krg}	Pc_{max} (KPa)	b	C ($s^{-0.5}$)	R^2
Bakken1	0.79	0.80	4	1	5	335	8.0	0.0081	0.989
Bakken4	0.80	0.40	8	1	5	460	2.5	0.0038	0.991
Berea3	0.45	0.70	6	1	4	10	2.1	0.0032	0.994
Berea4	0.47	0.68	8	1	4	14	4.3	0.0046	0.996
Bakken2	0.84	0.80	2	1	5	120	2.0	0.0131	0.895
Bakken3	0.78	0.40	8	1	5	370	2.4	0.0121	0.955
Berea1	0.47	0.70	2	1	4	20.5	2.0	0.0197	0.960
Berea2	0.47	0.67	2	1	4	19.5	2.0	0.0175	0.962

Experimental results, numerical solutions, and linear fittings are shown in Figure 3-5. By adjusting relative permeability and capillary pressure, the numerical model results were matched with the experimental data using the Approaching Method. The parameters for history matching, the slopes (C) and correlation coefficients (R^2) of linear fitting are presented in Table 3-3. Experimental results of all samples show a similar pattern. In all OEO experiments, imbibition curves have two stages: (1) At the early stage, the recovery factor increases rapidly and shows a linear relationship with the square root of time. However, samples Bakken1 and Bakken2 show a delay effect compared with numerical solutions, this phenomenon was possibly caused by the resistance of Bakken samples' oil-wet surface to wettability alteration by brine. (2) At the late stage, the recovery factor shows a sharp inflection point and quickly reaches the maximum value because the imbibition front reaches the bottom end of the core plug. The linear fitting of recovery factor of OEO imbibition indicates a good linear relationship between the recovery factor and $\sqrt{t}$.

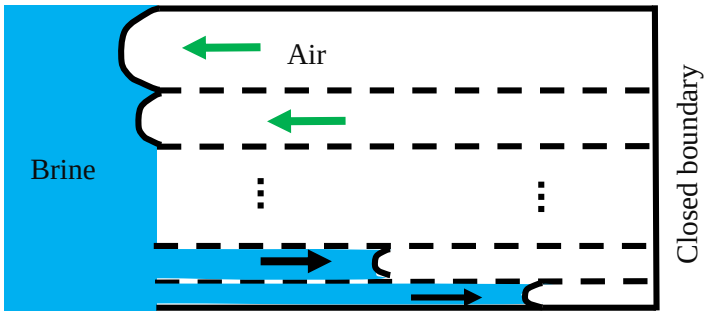

Figure 3-6 Schematic of interacting capillary bundle for counter-current imbibition.

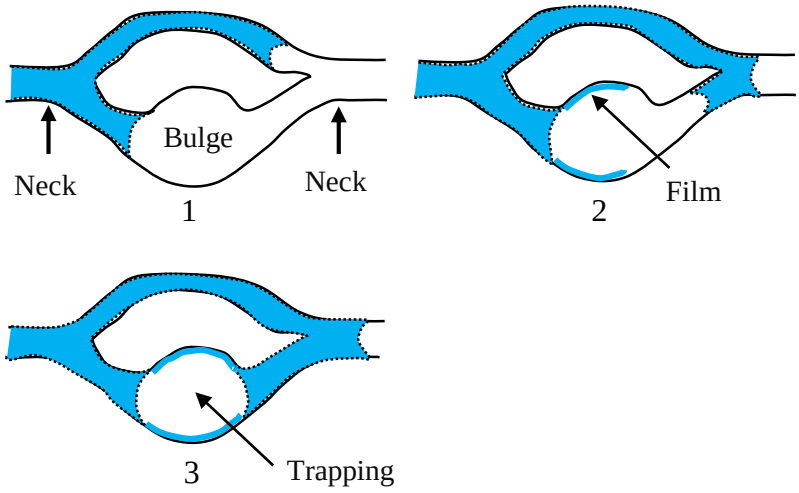

Figure 3-7 Illustration of trapping of non-wetting phase.

The ultimate recovery factors of Berea3 and Berea4 are 0.45 and 0.47, respectively (Figure 3-5). However, recovery factors of Bakken1 and Bakken4 are much higher which are 0.79 and 0.8, respectively. Two factors may cause higher recovery factors in Bakken samples. First, the Middle Bakken formation is tight and naturally fractured (Liu et al., 2018; Olatunji et al., 2018). Pore structures of the Bakken samples are dominated by extremely small mesopores (Figure 3-3). The wetting phase is easy to be imbibed into smaller pores than into larger pores due to high capillary pressure (Sang et al., 2018). This phenomenon can be seen from an interacting capillary model

presented by Dong et al. (2005) that the wetting phase was imbibed into the smallest capillaries first and later into capillaries with increasing diameters (Dong et al., 2005). Based on this model, we presented a schematic diagram of counter-current spontaneous imbibition with interacting capillaries as shown in Figure 3-6. The left end is the inlet and the right end is the no flow boundary. Due to the capillary difference between large and small capillaries, the wetting phase imbibes into smaller capillaries and the non-wetting phase flows out of the larger capillaries. A large quantity of mesopores may cause high recovery factors of the Middle Bakken samples. Second, the non-wetting phase is much easier to be trapped in larger pores. Immiscible displacement experiments of a string of pore doublets conducted by Chatzis and Dullien show that the entrapment of the non-wetting phase is easy to occur in large pores, especially the bulge sandwiched between the two neck pores (Chatzis and Dullien, 1983). This phenomenon can be explained by spreading and instability of bulk films ahead of the interface. This typical mechanism of non-wetting phase entrapment is presented in Figure 3-7. The flow in smaller pores is faster than flow in larger pores. The non-wetting phase is much easier to be trapped in bulge than in smaller pores. Thus a large quantity of large macropores in Berea samples (Figure 3-3) may cause low recovery factors of Berea cores.

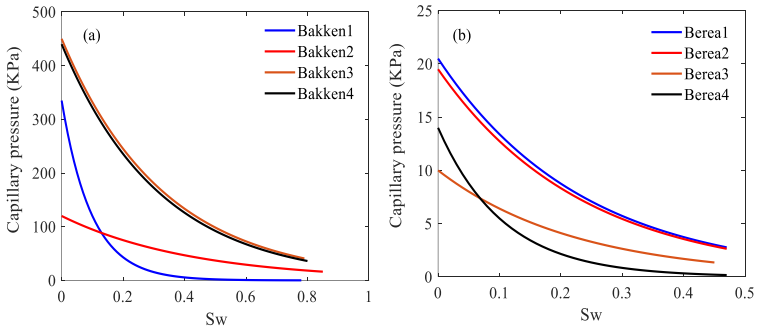

Figure 3-8 Capillary pressure curves of eight cores.

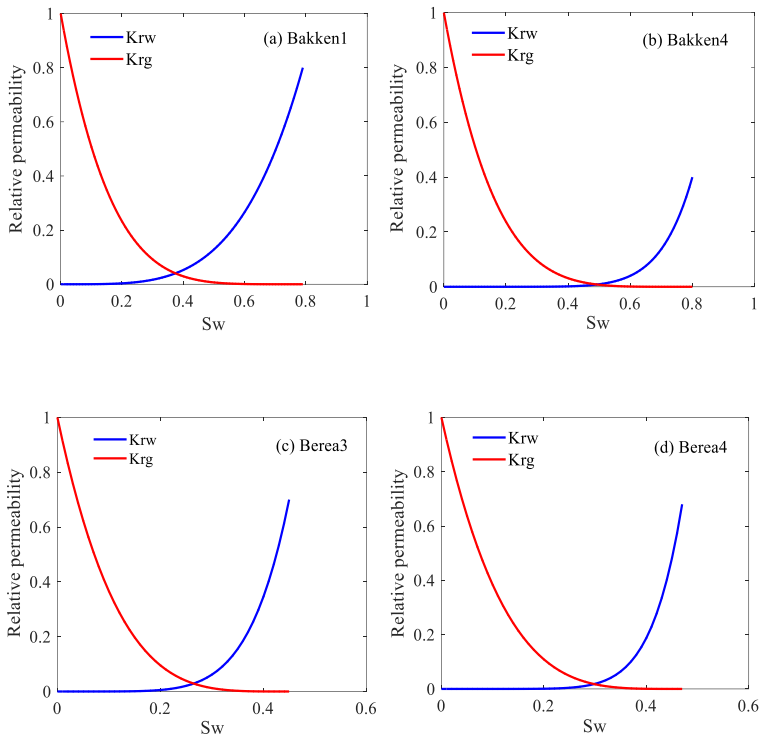

Figure 3-9 Relative permeability curves of cores for OEO imbibition.

Both the capillary and relative permeability can be obtained by matching mathematical models with experimental results. Considering the experimental setup, the mathematical model used is Eq. (3.7) which considers the gravity effect and is more accurate than the model in Eq. (3.10). The parameters $k_{rw,max}$, N_{Krw}, $k_{rg,max}$, N_{Krg}, and $p_{c,max}$ were obtained from the matching and are shown in Table 3-3. The capillary pressure and relative permeability curves are shown in Figure 3-8 and Figure 3-9. The obtained maximal capillary pressure of Bakken1 and Bakken4 are approximately 335 KPa and 460 KPa, respectively. Song and Yang (2017) indicated that the maximal gas-liquid capillary pressure of tight Bakken formation is approximately 240-350 KPa (Song and Yang, 2017). Those results are consistent with results in Figure 3-8. Whereas the maximal capillary pressure of Berea samples is much lower at about 10-14 KPa. This is similar to the result in literature that the maximum capillary pressure of air-liquid for Berea cores is around

8 KPa (Li et al., 2006). For spontaneous imbibition using dry rocks, the water saturation of the relative permeability curve vary from 0 to maximal water saturation (Alyafei et al., 2016; Alyafei and Blunt, 2018). The capillary force is the major driving force for spontaneous imbibition. The relative permeability curves for spontaneous imbibition and flooding experiments are probably different due to differences of driving forces and water saturation.

4.3. Effect of Gravity on Imbibition

The driving force of spontaneous imbibition is dominated by capillary forces. The gravity is usually neglected for spontaneous imbibition modeling (Alyafei and Blunt, 2018; Li et al., 2006). In fact, gravity may impact the imbibition process and is one of the major concerns in the study of spontaneous imbibition (Mirzaei-Paiaman, 2015; Prey and Lefebvre, 1978). In the experimental setup, brine can be vertically imbibe into cores through the top face. In such a case, gravity force contributes to the acceleration of the spontaneous imbibition process.

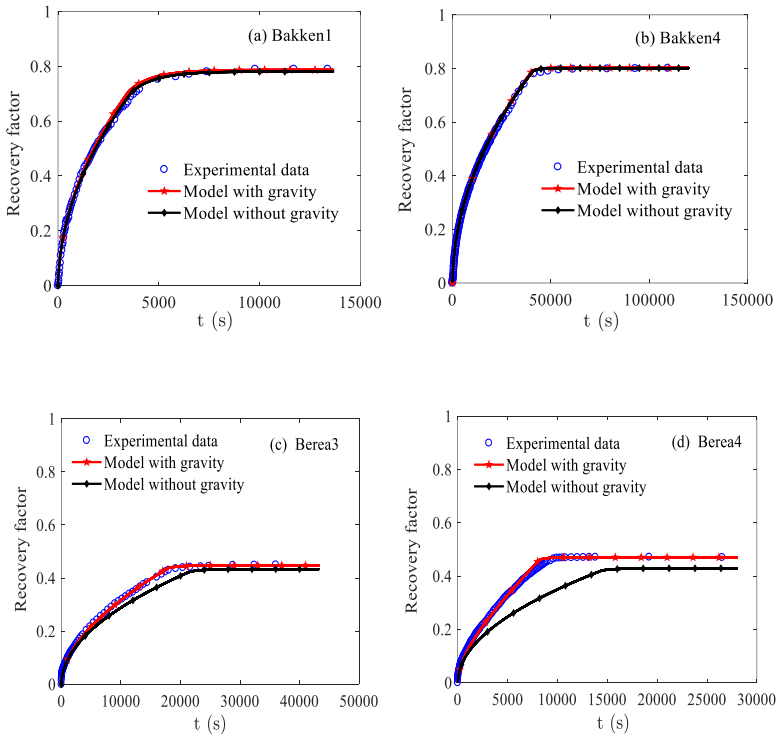

Figure 3-10 Recovery factors of experiments and models (with and without gravity) as a function of time.

The recovery factor profiles of experiments and models considering and neglecting gravity are shown in Figure 3-10. In order to study the recovery in absence of gravity, the cores were assumed to have the same capillary pressure and relative permeability obtained from the history matching (Figure 3-8 and Figure 3-9). For samples Bakken1 and Bakken4, recovery performances of the model with gravity are consistent with those of neglecting gravity. However, the recovery curves of samples Berea3 and Berea4 show a large deviation as the gravity is neglected. The deviation is small at the early stage and increases with time. The neglecting of gravity force would cause underestimation of both recovery rate and ultimate recovery factor. As can be seen from Figure 3-10d, recovery of Berea4 reaches the equilibrium point at the time of 15,000 seconds for the case of neglecting gravity force. However, the recovery of case with gravity force effect reaches the equilibrium point at time of approximately 10,000 seconds. In addition, the ultimate recovery factor in absence of gravity is about 0.4 which is lower than the experimental recovery factor of 0.48. Those results confirm that the spontaneous imbibition of Berea cores is a capillary-gravity dominated process. However, the imbibition processes of Bakken samples are dominated by capillary force. The capillary force of Bakken samples is much higher than that of Berea samples (Figure 3-8). By comparing capillary pressure and permeability data, it can be further concluded that spontaneous imbibitions in tight rocks are dominated by the capillary force. However, spontaneous imbibitions in high permeability rocks are controlled both by capillary force and gravity force. The gravity effect must be considered in the analysis of imbibition in high permeability rocks.

4.4. TEC Imbibition

For TEC imbibition, the top and bottom faces of the Bakken2, Bakken3, Berea1, and Berea2 were sealed with epoxy resin. Thus, the TEC imbibition experiments for those cores are radial flow. Even though there have been many experimental studies on the TEC imbibition (Cheng et al., 2018; Lyu et al., 2019; Yildiz et al., 2006), there are very few numerical studies focusing on this radial imbibition.

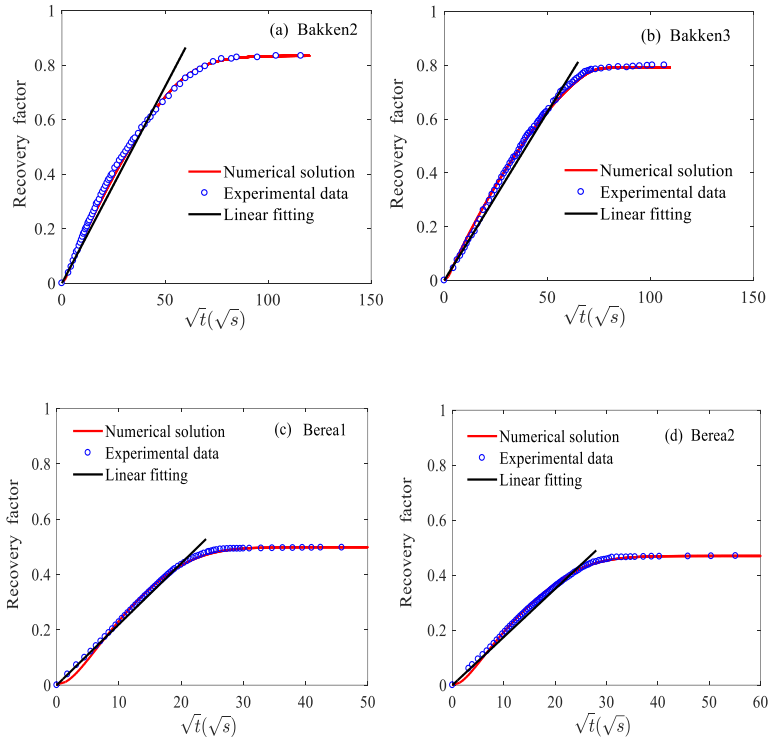

Figure 3-11 Recovery factors of cores for TEC imbibition as a function of $\sqrt{t}$.

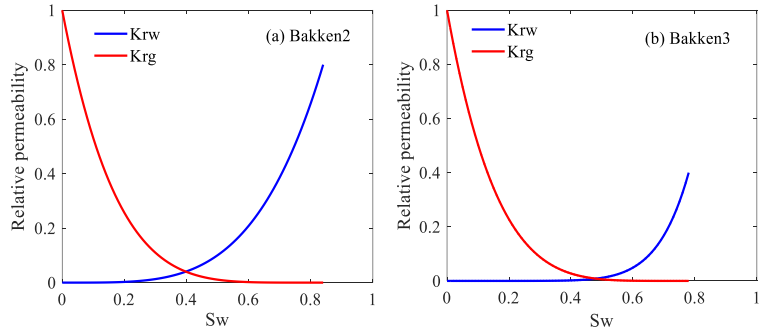

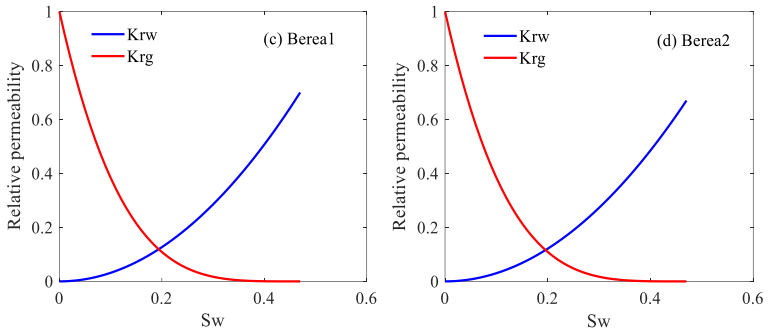

Figure 3-12 Relative permeability curves of cores for TEC imbibition.

Experimental imbibition results, numerical solutions, and linear fitting for TEC imbibition are presented in Figure 3-11. At the early stage, the recovery factor increases rapidly and shows a linear relationship with $\sqrt{t}$. In the late stage, the recovery factor gradually reaches a plateau. The capillary pressure and relative permeability of Middle Bakken and Berea cores are presented in Figure 3-8 and Figure 3-12, respectively. The Young-Laplace equation indicates that capillary pressure is proportional to the reciprocal of pore radius. The capillary pressures of Bakken samples are much higher than those of Berea samples. This is because the Bakken samples are tight rocks and the pore diameters are smaller than those of Berea samples (Figure 3-3). The parameters of numerical solutions and linear fitting are shown in Table 3-3. It is observed that correlation coefficients of TEC imbibition experiments were presented.

5. Materials and Methods for Surfactant EOR

5.1. Rocks and Surfactants

Eight core plugs (six Bakken cores, and two Berea cores) were selected to conduct spontaneous imbibition experiments. Six Bakken cores were obtained from the Middle Member of the Bakken Formation in Mckenzie County, North Dakota. Samples Bakken5 and Bakken6 are obtained from well #1 at the depth of 11096 ft. Samples Bakken1~4 are obtained from well #2

with depth ranging from 10791 to 10801 ft. Two Berea cores were cut from outcrops in Cleveland Quarries, Ohio. Core sample preparation includes extracting cores with toluene and methanol for 20 days and drying core samples in an oven for 7 days. After the cleaning and drying of core samples, diameter length, porosity, and permeability were tested. Petrophysical properties of studied samples are shown in Table 3-4.

Table 3-4 Summary of the petrophysical properties of core plugs

Samples	Depth (ft)	Length(cm)	Diameter (cm)	Permeability (mD)	Porosity
Bakken1	10801	3.19	3.96	0.004	0.042
Bakken2	10791	3.17	3.95	0.002	0.038
Bakken3	10791	3.14	3.96	0.002	0.036
Bakken4	10796	3.32	3.95	0.005	0.068
Bakken5	11096	4.07	3.75	0.051	0.053
Bakken6	11096	2.37	3.78	0.064	0.057
Berea1		6.68	3.96	57.60	0.20
Berea2		6.94	3.95	64.10	0.19

As shown in Table 3-4, The Middle Bakken samples are tight rocks and have low porosity and permeability. Air permeabilities of Bakken samples range from 0.002 to 0.064 mD. Porosity of Bakken samples varies from 0.036 to 0.068. However, Berea samples are high permeability and porosity rocks.

5.2. SEM and XRD Analysis

The SEM method was used to observe microstructures of Bakken samples. SEM images of studied samples are presented in Figure 3-12.

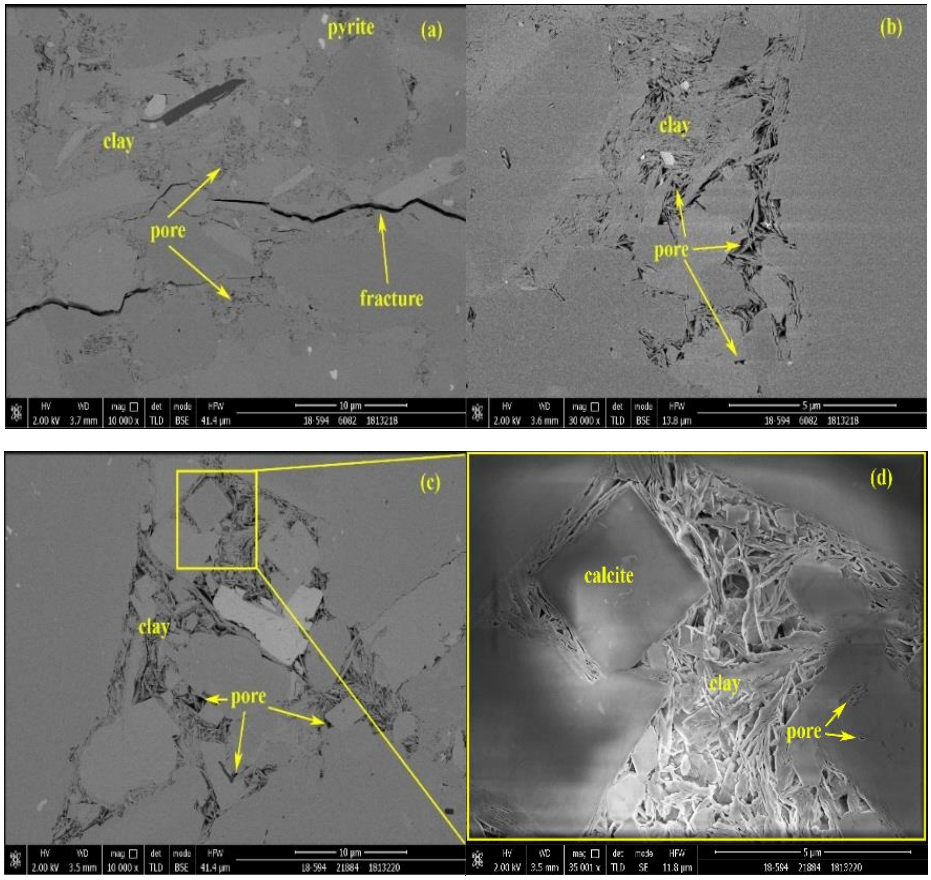

Figure 3-13 SEM images of studied samples. (a~b) Bakken 5 and 6. (c~d) Bakken 2 and 3.

The SEM images (Figure 3-13) indicate that Bakken5 and 6 are characterized by fractures, laminated clays, and large amounts of pores in nanometer. Width of the fractures and pores ranges from nanometers to micrometers. Samples Bakken2 and 3 exhibit large quantity of slit-pores inside the clays. No obvious fracture was observed in samples Bakken 2 and 3.

The mineralogical analysis using X-ray diffraction (XRD) was conducted for the core samples and are shown in Table 3-5.

Table 3-5 Mineralogical composition of Middle Bakken and Berea cores

Samples	Kaolonite (wt %)	Illite (wt %)	Mx I/S (wt %)	Chlorite (wt %)	Quartz (wt %)	Calcite (wt %)	Dolomite (wt %)	Feldspar (wt %)	Pyrite (wt %)
Bakken1		7	1		36	20	20	15	1
Bakken2		16	1	1	33	3	24	19	3
Bakken3									
Bakken4		6	1	1	42	5	25	19	1
Bakken5		11	2	1	30	14	28	12	2
Bakken6									
Berea	5				88		2	5	

As indicated in Table 3-5, the major minerals of the Middle Bakken samples are quartz, dolomite, feldspar, and calcite. The Middle Bakken cores are light gray limestone. However, Berea cores are fine-grained, clay-cemented quartz sandstone. The dominant mineral of Berea cores is quartz.

5.3. Surfactants and Solutions

The brine solution used for the experiments is 2 wt% NaCl to prevent clay swelling problem. Surfactants used for the experiments are commercial surfactants. MERPOL-HCS (HCS) is a nonionic surfactant from Stepan Company. SOLOTERRA-964 (964) and Sodium dodecyl sulfate (SDS) are anionic surfactants. Cetyltrimethylammonium bromide (CTAB) is a cationic surfactant. The surfactant solutions are made of 0.1 wt% surfactants and 2 wt% NaCl.

5.4. Imbibition Experiments

The Middle Bakken Formation has high salinity, high-temperature, and high-pressure

conditions. To simplify the experimental method, spontaneous experiments were performed in imbibition cells under low temperature and low salinity conditions. Before the imbibition experiments, the cores were fully saturated with Bakken oil. The experimental steps are as following: (1) The ZYB-II Vacuum Saturation Device was used to vacuum the cores for 24 h to remove the air in the cores. (2) Saturated cores with Bakken crude oil at 20 MPa for 20 days. The cores are fully saturated until the pressure doesn't change. (3) Core were aged in Bakken crude oil in the oven (60 °C) for 1 month before imbibition experiments. (4) The cores were placed at the bottom of the cells with 0.05 mL accuracy. Cells were filled with brine or different surfactant solutions. (5) The displaced oil volume was recorded with time until no oil was displaced out. All experiments were conducted with all face open boundary conditions in an oven at 60 °C. The image of the experimental apparatus is presented in Figure 3-14.

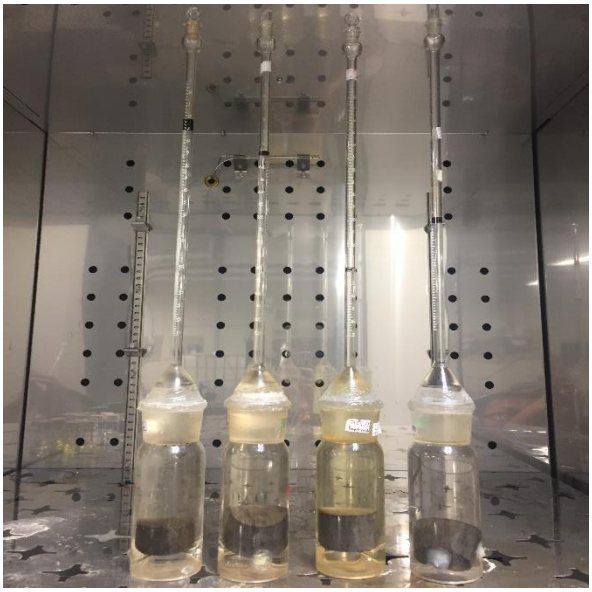

Figure 3-14 Image of experimental apparatus. Experiments were conducted in an oven at 60 ℃.

6. Results and Discussion

6.1. Pore Size Distribution

Pore size distribution (PSD) is crucial to the recovery process of oil in tight rocks. Nitrogen adsorption is a common method to test the PSD of Bakken samples. PSDs of Bakken samples from nitrogen adsorption method is shown in Figure 3-15a. However, Berea samples are high permeability and porosity rocks. Mercury is capable of detecting PSD of Berea samples. Figure 3-15b represents PSD of Berea outcrop samples reported by Cardoso and Balaban (2015).

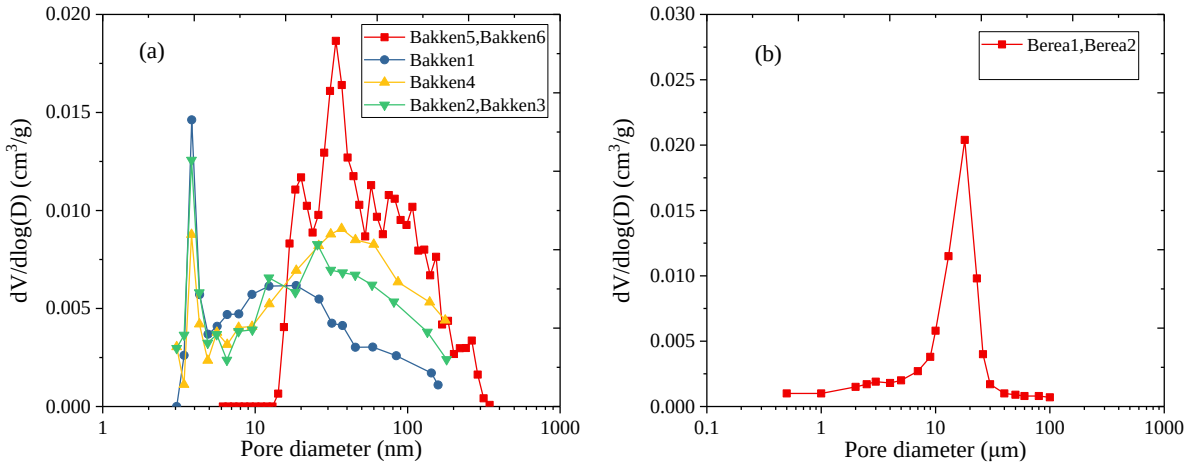

Figure 3-15 Pore size distribution of studied samples. (a) Bakken samples. (b) Berea samples from mercury intrusion by Cardoso and Balaban (2015).

Pore structures were analyzed and the following observations were reached: (1) The Middle Bakken samples have large amounts of nanopores with diameter ranging from 3~300 nm. However, diameter of Berea samples ranges from 0.5-100 μm. (2) Bakken5 and 6 show a unimodal PSD, whereas Bakken 1~4 exhibit bimodal PSDs which are similar with the results of Cho et al. (2016). (3) Samples Bakken5 and 6 are from well #1 and have larger average pore diameter than samples Bakken 1~ 4 from well #2. Meanwhile, samples Bakken 1~ 4 show larger portions of mesopores (3~20 nm) than Bakken 5 and Bakken6.

6.2. Surfactant Imbibition Experiment

The spontaneous imbibition study consists of four groups of experiments with brine, 0.1 wt% SDS (anionic), 0.1 wt% CTAB (cationic), and 0.1 wt% HCS (nonionic). Samples used in the experiments are Bakken 1~4 and they are all from the same well with small depth variation (10791-10801 ft). The recovered oil is presented as percentage of the original oil in place (OOIP) shown in Figure 3-16.

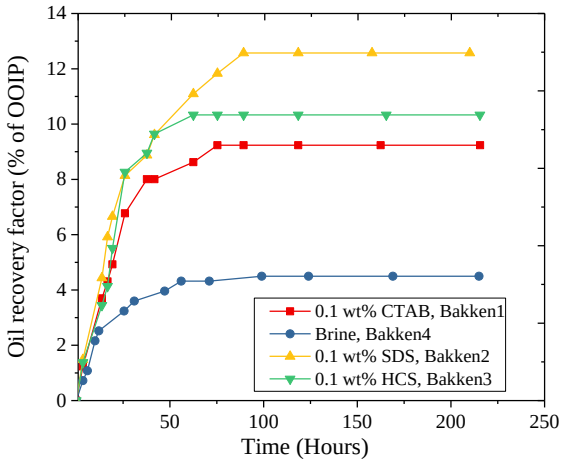

Figure 3-16 Oil recoveries of Bakken 1~4 (well #1) spontaneous imbibition experiments with and without various surfactants added.

It can be observed from Figure 3-15 that the brine alone was not able to produce much oil through spontaneous imbibition experiment. The ultimate recovery factor of brine imbibition is only 4.3%OOIP. However, recovery factors of surfactant-assisted imbibition are much higher than that of brine imbibition. The anionic surfactant (SDS) yields 3 times of recovery factor than brine. The recovery factors of nonionic (HCS) and cationic (CTAB) are around 2 times of that of brine. As the concentration of those surfactants are same, the reason why anionic surfactant yields highest oil recovery is its higher efficiency on wettability alternation. The oil recovery may be impacted by wettability and interfacial tension (IFT). However, the wettability is the controlling factor to

improvement oil recovery for tight rocks (Liu et al., 2019; Sheng, 2017). The wettability alternation is mainly caused by adsorption of surfactant at rock surface and oil-water interface. Clay is capable of adsorbing large quantity of surfactants through hydrogen bonding due to much higher hydroxyl density on its surface than other minerals (Zhong et al., 2019b). Bakken samples have similar PSDs. However, they have large differences considering mineralogical composition. Clay content of Bakken 2 and Bakken3 is much higher than that of Bakken1 and Bakken4 as shown in Table 3-5. Thus, high oil recovery factors of Bakken2 and Bakken3 can be explained by wettability alternation caused by higher adsorption of surfactants at Middle Bakken's minerals especially clays.

To study the effect of pore size on oil recovery. Spontaneous imbibition experiments using Bakken and Berea sandstones were conducted. The average pore diameter of Berea cores is significantly larger than that of Bakken samples (Figure 3-14). Oil recovery of Berea2 through brine imbibition is 47%OOIP which is much higher than that of Bakken6 and Bakken4 because of its larger average pore size. The average pore diameter of Berea cores is approximately 21 μm. In contrast, average pore diameter of Bakken6 and Bakken4 are approximately 40 and 28 nm, respectively. Ultimate oil recovery of Bakken6 is 15%OOIP which is higher than Bakken1's recovery of 4.3%OOIP. Mineralogical compositions of Bakken samples are similar, thus the effect of minerals is not considered. In addition, PSDs of samples Bakken1~4 show bimodal distributions. There are large quantities of extremely small pores with diameters around 4 nm. Oil recoveries of Bakken1~4 are extremely low due to a large portion of pores in nanometer. Furthermore, spontaneous imbibition experiments with 0.1wt % anionic surfactant (964) were conducted on Bakken5 and Barea1. The results are presented in Figure 3-17.

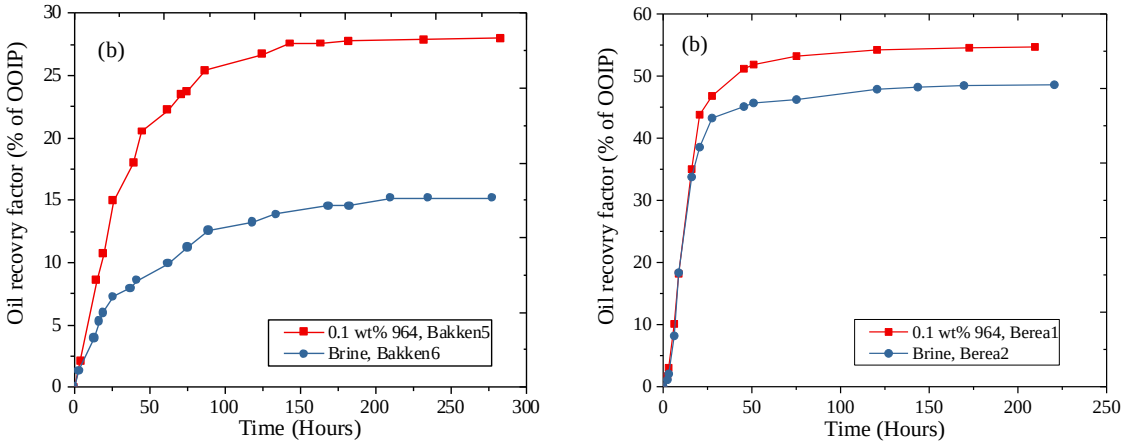

Figure 3-17 Oil recovery process of samples with different pore size distribution. (a) Bakken5, 6 from well #1. (b) Berea samples.

As shown in Figure 3-17, oil recovery is dramatically improved by surfactant solution. Oil recovery of Bakken5 is approximately 2 times of that of Bakken6. However, oil recovery of Berea1 is slightly improved. This is because Bakken5 and Bakken6 have higher clay content than Berea samples shown in Table 3-5. Anionic surfactant (964) can change the wettability of Bakken6 from oil wet to water wet due to its high adsorption capacity on clay surface as discussed above, thus significantly improved oil recovery.

7. Summary

New methods to obtain capillary pressure and relative permeability were proposed by matching mathematical models with imbibition experiments with different boundary conditions. Surfactant imbibition experiments were carried out on tight Bakken rocks. Based onthe experiments and numerical models, the following conclusions were drawn:

(1) NMR pore size distributions show that Bakken rocks have a large percentage of mesopores and a small amount of micropores, macropores, and fractures. Pore diameters range from 0.3 nm to 200 nm. Widths of the fractures range from 0.6 μm to 2 μm. However, Berea rocks

are dominated by macropores with diameters range from 0.07 μm to 70 μm.

(2) Recovery factor of OEO imbibition exhibits a linear relationship with $\sqrt{t}$. However, the recovery factor TEC imbibition shows a good relationship with $\sqrt{t}$ at its initial stage and a poor linear relationship with$\sqrt{t}$ at its late stage.

(3) For OEO and TEC spontaneous imbibition, the imbibition models are consistent with the experiments. The capillary and relative permeability were obtained from the matching. Recovery factors and capillary pressure of Bakken rocks are much higher than those of Berea rocks.

(4) The Gravity has insignificant effects on the recoveries of tight rocks. However, it has significant impacts on the recoveries of high permeability rocks.

(5) While the oil recovery by water imbibition is around 4.3~15%OOIP, the surfactant-assisted imbibition recovery varies from 9%~28%OOIP. In addition, the anionic surfactant yields higher oil recovery factors than cationic and nonionic surfactants.

(6) For studied samples, oil recoveries of cores by surfactant solutions and brine are significantly impacted by average pore size. The larger the pore size the higher the recovery factor. Surfactant can significantly improve oil recovery due to their high adsorption capacity on clay surface.

CHAPTER IV

EXPERIMENTAL AND NUMERICAL STUDIES OF FLOW AND STORAGE MECHANISMS OF SHALE OIL RESERVOIRS

1. Introduction

Shale oil and gas reservoirs have become important complements to conventional reservoirs due to the growing global energy demands and the reducing reserves of producing conventional sandstone and carbonate reservoirs (Liu et al., 2017; Nguyen et al., 2018; Zhang et al., 2019a). Shale gas and oil reservoirs have been widely explored in North American shale plays with the application of hydraulic fracturing in horizontal wells such as Permian, Bakken, Barnett, and Eagle Ford shale plays (Hughes, 2013; Middleton et al., 2017; Tian et al., 2019a). Additionally, shale formation is also a possible medium to serve as the cap rock for CO_2 sequestration due to its small pore size, kerogen, and low permeability (Jiang et al., 2016; Tian et al., 2019b; Wang et al., 2018; Zhou et al., 2018). Nevertheless, the development and utilization of the shale reservoir is challenging due to its low permeability, complicated storage and flow mechanisms of water and oil (Hawthorne et al., 2019a; Iglauer et al., 2015; Jia et al., 2018).

Shale rocks are typically a complex and heterogeneous system, with both inorganic matrix and organic matter (Saif et al., 2017; Song et al., 2018; Wang et al., 2016). The inorganic matrix is composed of various content of minerals such as quartz, dolomite, calcite, and clay. The inorganic pores in organic matter range from nanometer to micrometer. The organic matter is composed of amorphous carbon skeleton and inorganic pores with diameters range from angstroms to micrometers (Bousige et al., 2016). The organic matter is randomly distributed within the inorganic minerals. The coexistence of inorganic minerals and organic matter leads to the

wettability heterogeneity, which potentially impacts the water and oil storage in shale rocks. Wang et al. (2018) characterized the wettabilities of organic pores, inorganic pores, and microfractures in Longmaxi shale by combining nuclear magnetic resonance (NMR) and field-emission scanning electron microscopy (FE-SEM). Their results indicated that the organic pores are oil-wet and inorganic pores and microfractures are water-wet and mixed-wet, respectively (Wang et al., 2018). Additionally, the TOC also affects the wettability of shale rock. The water contact angle increases dramatically with the TOC (Arif et al., 2017). Similar results were reported in some literatures (Roychaudhuri et al., 2013; Siddiqui et al., 2018; Yassin et al., 2017). The wettability of shale surface changes from water-wet into oil-wet with the increase of TOC (Su et al., 2018). Finally, the water content significantly impacts the CO_2 sequestration and oil recovery (Cui et al., 2019; Fernø et al., 2015; Jia et al., 2019; Plug and Bruining, 2007; Soltanian et al., 2018). In order to study the wettability and storage of water in shale rocks, spontaneous imbibition is a widely used method to explore the water wettability and storage in shale rocks (Dehghanpour et al., 2013; Lan et al., 2015; Wang et al., 2018). This method has a limitation of determining the maximum water volume in shale rocks due to the existence of residual air in the rocks.

Oil in shale rocks is typically present in three forms including free, adsorbed, and dissolved (absorbed) oils. Free oil exists in inorganic and organic pores and is free to flow. Adsorption refers to a surface phenomenon. In shale rocks, inorganic matrix and kerogen are porous and both are capable of adsorbing hydrocarbons on their surface (Heller and Zoback, 2014; Wu et al., 2019). Dissolved oil refers to the hydrocarbons that dissolved in the kerogen skeleton. Organic matter is capable of absorbing hydrocarbons in its bulk. This part of the oil in kerogen occurs in a dissolved form which is also named absorbed oil (Sang et al., 2018). Characterizations of the inorganic pores and kerogen are crucial for evaluating the shale oil reservoirs, especially the mechanisms by which

oil is stored in them. Shale oil rocks generally have low porosity, so any process that increases porosity in these rocks would serve to probably improve their storage capacity (Fishman et al., 2012).

The organic matter significantly impacts the oil storage capacity of shale. The organic porosity is created within kerogen as a result of the maturation process during and after oil generation (Jarvie et al., 2007). Should such a mechanism lead to the creation of secondary organic pores, and if that porosity is capable of storing oil in shale oil reservoirs (Loucks et al., 2012), then organic porosity would play a necessary, and possibly a key role in shale oil systems. Measurements of large numbers of shale samples suggested that the organic porosity shows an increase with R_o (0.4%-1.0%) and exhibits an exponential relationship with R_o (Modica and Lapierre, 2012). In addition, the total porosity and specific surface area of shale oil samples are also impacted by thermal maturity and total organic content. While the shale porosity and specific area increase with TOC, the specific surface area increases significantly with thermal maturity as R_o<1.4% indicating that the maturation of kerogen may create a large number of nanopores (Song et al., 2019). However, literature indicated that organic pores are not purely a product of thermal maturation but may partly come from primary pores (Löhr et al., 2015). In summary, there have been many studies related to characterizing the storage capacity of organic pores. Nevertheless, there has been no comprehensive tests of the dissolved hydrocarbons within the kerogen matrix and how it evolves with kerogen maturity due to the lack of reliable experimental methods.

Shale formation has been considered as a feasible formation for supercritical CO_2 (sCO_2) injections, which simultaneously implement CO_2 sequestration and enhancing hydrocarbon recovery. Recently, many articles have been published regarding sCO_2 injection for organic-rich shale rocks. Jin et al. (2017) investigated the sCO_2 injection and measured the adsorption of CO_2

in Bakken shale rocks (Jin et al., 2017). Their results demonstrated that the adsorption of CO_2 in Bakken shale is very high, which reached approximately 16 mg/g, and that oil recovery ranges from 15-65%. In addition, the adsorption of CO_2 in shale rocks increases significantly with the TOC, indicating shale is probably feasible target for CO_2 sequestration (Ross and Marc Bustin, 2009; Tao and Clarens, 2013). Experimental results also suggested that a higher TOC led to higher CO_2 wettability on shale rocks (Pan et al., 2018).

The shale formation typically has high contents of water, oil, and kerogen, which significantly impact the oil recovery and CO_2 sequestration in shale reservoirs. The organic matter probably adsorbs and absorbs a large quantity of oil and CO_2 (Charoensuppanimit et al., 2016; Pan et al., 2019). Should the kerogen be able to store CO_2 and oil, then the mass transfer between kerogen and pore structure is a potentially critical mechanism of CO_2 sequestration and producing oil from kerogen. Some research has been conducted on the transport mechanisms of hydrocarbons in kerogen using molecular dynamics simulation. The diffusion coefficient of hydrocarbons in kerogen is impacted by hydrocarbon structure, kerogen structure, and temperature (Falk et al., 2015; S. Wang et al., 2016). Additionally, some literatures have investigated the mechanisms of multiple phase flow in pore structures of shale rocks (Fernø et al., 2015; Liu et al., 2018; Song et al., 2018). Nevertheless, the mechanisms, especially how water, oil, and CO_2 storage and transport in the different types of pores and kerogen, are still ambiguous. There are no kinetic equations to model the mass transfer between pore structures and kerogen.

In this work, TOC, pore structure characteristics, mineralogical composition, and kerogen maturity of shale samples were obtained from a comprehensive petrophysical analysis. Then water and oil vacuum-imbibition experiments were conducted with crushed spherical-shaped shale samples. The water storage capacity in inorganic pores was obtained from water vacuum-

imbibition. In addition, the volumes of oil that are stored in inorganic pores, organic pores, and dissolved in kerogen matrix were determined from oil vacuum-imbibition experiments. The effects of TOC and R_o on kerogen storage capacity were analyzed. Finally, mathematical models for water and oil vacuum-imbibition were proposed for the first time in this paper. A kinetic equation of mass transfer between pore structure and kerogen was derived from a novel pore-kerogen double diffuse layer (PKDDL) model. This paper proposes new methods to evaluate the storage and transfer mechanisms of water and oil in shale, which are of critical importance for evaluating and utilizing shale reservoirs.

2. Materials and Methods

2.1. Experimental Principle

For vacuum imbibition tests, the imbibed volumes of oil and brine are different due to the wettability heterogeneity of pore structures. The inorganic pores in the inorganic matrix are water-wet/mix-wet and that organic pores in kerogen are oil-wet (Pan et al., 2018; Su et al., 2018; Wang et al., 2018). Brine is able to be imbibed into inorganic pores but is not able to be imbibed into kerogen due to the strong oil-wet surface of the kerogen maceral. The water storage capacity approximately equals the volume of inorganic pores. However, the oil is able to be imbibed into both inorganic pores and organic pores. Therefore, the maximum volume of imbibed water equals the volume of inorganic pores. The maximum volume of imbibed oil represents the total oil in inorganic pores and kerogen. Thus, the difference between the imbibed volumes of brine and oil is the oil volume in the kerogen. This part of oil typically includes the oil in organic pores and the dissolved oil in kerogen. While the imbibition process in pore structure is a very fast process, the diffusion process from the pore structure into kerogen is a rather slow process. If the imbibed oil volume is plotted against log t, then the inflection point of this imbibition curve approximately

equals the total pore volume (inorganic pores and organic pores). The difference between the total pore volume and inorganic pore volume represents the organic pore volume. Similarly, the dissolved oil volume can be obtained by the difference between the total oil in kerogen and oil in the organic pore volume.

2.2. Experimental Setup

Before imbibition tests, shale samples were cut from whole cores and crushed into particles. The particles were polished by use of sandpapers to obtain spherical-shaped particles. The average diameter of crushed particles is approximately 1 cm. The first advantage of using 1 cm particles is the preservation of original pores and natural fractures. The second advantage of using crushed samples is their larger contact areas with oil and brine which reduces the experimental time. Then the shale samples were cleaned with toluene and ethanol in Soxhlet extractor to remove the residual oil and salts, followed by drying the shale samples in an oven at 100℃.

The apparatus for the vacuum imbibition experiment was designed and its schematic diagram is shown in Figure 4-1. This setup mainly consists of two steel cells (around 50 ml), a molecular vacuum pump, and two burettes (readability of 0.005 ml). The experimental temperature was controlled at 24℃. The procedures of the experiment are as follows:

(1) The spherical-shaped samples were divided into two parts and then filled into two steel cells for imbibition tests. One imbibition cell was used for brine imbibition and the other one was used for oil imbibition. The brine used in the experiment is 8 wt% potassium chloride (KCl) solution. The oil used in imbibition is n-dodecane (>99.9%).

(2) The steel cells were vacuumed to remove the residual air in the sample. The molecular vacuum pump is able to vacuum the cells and samples to the extremely low pressure of approximately 0.001Pa.

(3) The valves were opened to connect the burettes with cells. The brine and oil were imbibed into the test cells. The liquid quickly filled the void volume between particles within a few seconds, which is very short compared with experimental time. Then liquid imbibition in rock samples occurs. The volumes of imbibed oil and brine were recorded with time. The liquid volume that imbibed into the shale sample was calculated from the difference between the total imbibed liquid volume and the void volume in the cell.

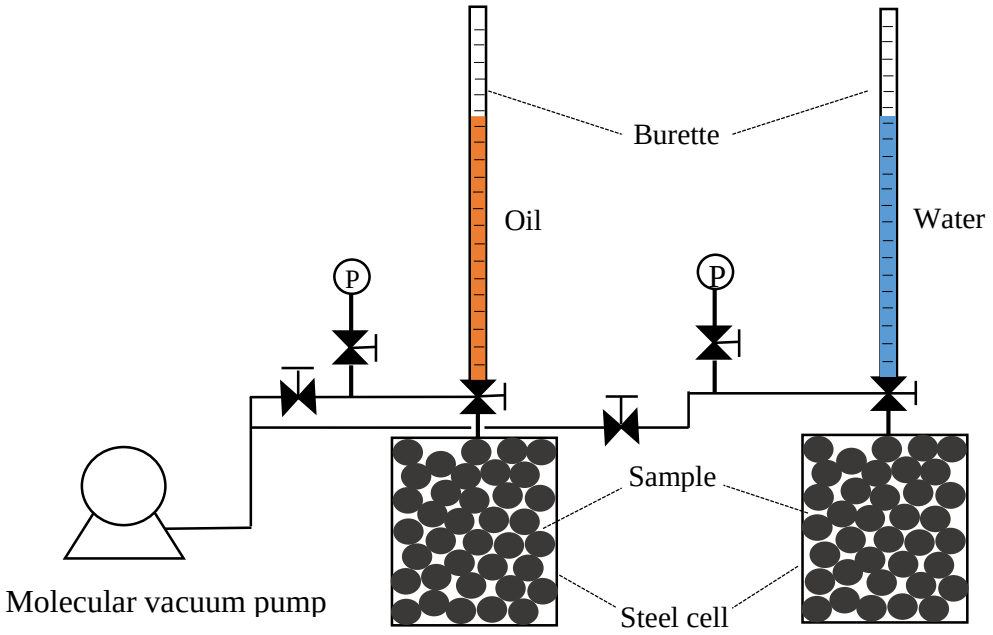

Figure 4-1 Schematic of vacuum imbibition experiment.

2.3. Rock and Fluid Properties

2.3.1. Fluids for Experiments

To prevent the adsorption of water on clay and the swelling problem of clay, a high concentration of brine solution was used as the test fluid. The 6 wt% of KCl solution can effectively prevent the swelling problem of the shale rock (Dehghanpour et al., 2013). The brine used in is 8 wt% of KCl solution, which is capable of avoiding the swelling problem. The viscosity of the 8

wt% KCL solution at 24℃ is 0.890 mP·s (Zhang and Han, 1996). The n-dodecane is used as light oil rather than crude oil because of the complex compositions of crude oil. Moreover, transport of C_{12} in shale oil rocks is similar to that of the light oil produced from shale oil reservoirs (Hawthorne et al., 2019a). The viscosity of the n-dodecane at 24℃ is 1.344 mP·s (Caudwell et al., 2004).

2.3.2. Petrophysical Properties of Samples

Eight shale samples were collected from one shale oil exploration well in Es3 Shahejie Formation in the Jiyang Depression in Bohai Bay Basin, East China. Shahejie Formation has been the target in recent years due to a large amount of oil trapped in the shale, which generally includes four members: Es1, Es2, Es3, and Es4 from top to bottom. The Es3 and Es4 members are the main source rocks among them (Xie et al., 2019). The density and helium permeability were tested using core plugs drilled from the whole core. Shale samples used in imbibition experiments were cut from the same whole core and crushed into spherical-shaped particles with average radii of approximately 0.5 cm. The average radius, permeability, and density for each sample are shown in Table 4-1. These shale samples are very tight with permeability varying from 0.007 to 0.032 mD.

Table 4-1 Petrophysical properties of the shale samples

Samples	D1	D2	D3	D4	D5	D6	D7	D8
Mean radius (cm)	0.52	0.46	0.51	0.47	0.48	0.53	0.45	0.53
Permeability (mD)	0.010	0.012	0.022	0.025	0.015	0.032	0.007	0.009
Density (g/cm^3)	2.34	2.45	2.47	2.42	2.48	2.53	2.32	2.33

2.3.3. SEM and N_2 adsorption analysis

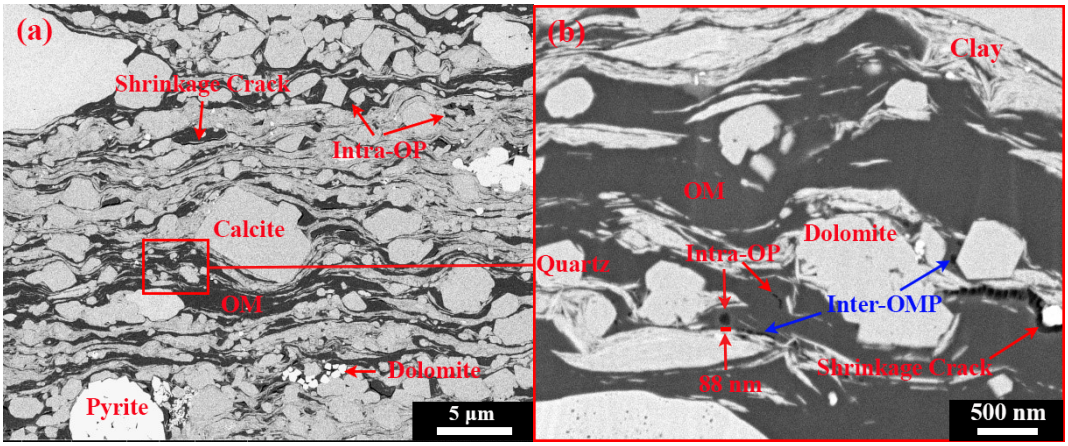

Figure 4-2 SEM images of shale sample from Shahejia Formation. Intra-OP: Organic Pore; Inter-OMP: Organic-Mineral Pore; OM: Organic Matter.

Figure 4-2 shows SEM images of a shale sample from Es3 Shahejie Formation. In the SEM images, darker areas are organic matter. In contrast, the lighter gray areas are inorganic mineral matrix primarily composed of dolomite, calcite, quartz, and clays. It was observed that the organic layers are obviously large scale lamina layers surrounded by mineral grains. These images show that the pore structures in the oil shale samples are in nanometers. In Figure 4-2b, two types of organic pores are observed: intra-organic pores, referring to pores within organic matter, and inter-organic-mineral pores, referring to pores between organic matter and minerals. Observed organic pores are typically nanopores, which are shaped circularly and irregularly. Additionally, shrinkage cracks were observed due to the loss of hydrocarbons in bulk kerogen.

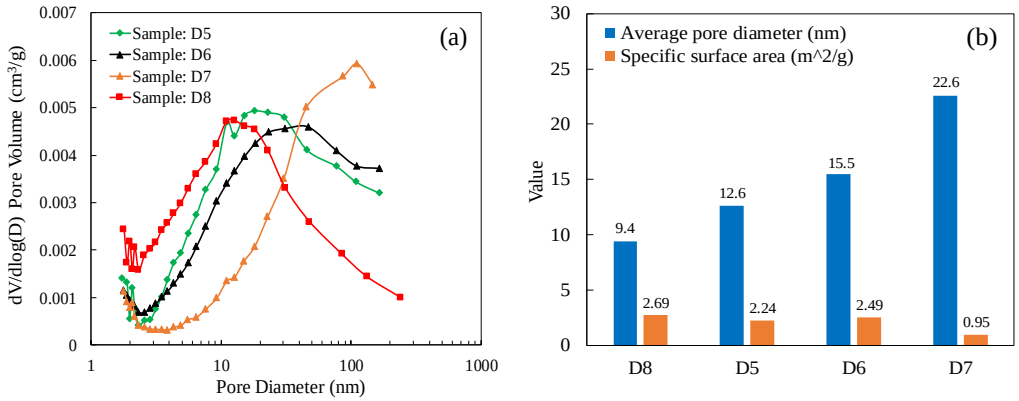

Figure 4-3 Pore structure analysis for four shale samples from N_2 adsorption method. (a) Pore size distribution, (b) Average pore diameter and specific surface area.

Figure 4-3 shows the pore size distribution, average pore diameter, and specific surface of four shale samples. The results from N_2 adsorption method indicate pore diameters of samples typically vary from 2 to 200 nm, which is very small. The average pore widths of samples D8, D5, D6, and D7 are 9.4, 12.6, 15.5, and 22.6 nm, respectively, which show an increasing trend. However, their specific surface areas are 2.69, 2.24, 2.49, and 0.95 m^2/g, respectively, which exhibit a decreasing trend. This result is consistent with the results from literatures that the specific surface area decreases with the pore size (Berthonneau et al., 2018; Luhmann et al., 2017). Those samples' average pore diameter is approximately 15.0 nm and average specific area is 2.1 m^2/g.

2.3.4. X-Ray Diffraction (XRD) Analysis

Table 4-2 Mineralogical composition of the shale samples (wt%)

Samples	Quartz	Calcite	Dolomite	Pyrite	Feldspar	Mixed-layer illite/smectite	Illite	Kaolinite	Chlorite
D1	20	39	5	4	5	10	17	-	-
D2	6	87	-	-	-	2	5	-	-
D3	16	54	8	5	1	9	6	-	-
D4	7	77	4	-	-	3	6	2	1
D5	7	70	16	-	-	1	5	1	-
D6	17	34	19	4	6	3	16	-	-
D7	40	36	14	4	-	2	13	-	-
D8	17	53	4	4	-	7	15	-	-

The lithology of shale rock samples is generally described as organic-rich mudstone. The XRD technique was used to investigate the minerals in samples D1~D8. The mineralogical composition of the studied samples is shown in Table 4-2. Shale samples are mainly composed of calcite, followed by quartz, clay, and dolomite with average contents of approximately 56.3 wt%, 16.2 wt%, and 15.8 wt%, respectively. The dominate clay minerals are illite followed by mixed-layer illite/smectite with average contents of 10.4 wt% and 4.6 wt%, respectively.

2.4. Mathematical Models

2.4.1. Water Vacuum Imbibition in Shale

For vacuum imbibition, the liquid and vapor phases reach a thermodynamic equilibrium at the meniscus in porous media. The evaporation of liquid in nanopore occurs within a few seconds (Jatukaran et al., 2018). This evaporation time is negligible compared with the experimental time, which takes hundreds to thousands of hours. To better understand the mechanisms of vacuum imbibition, a diagram of a single tube is shown in Figure 4-4.

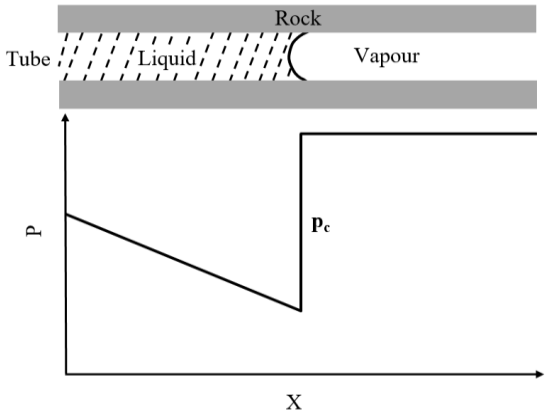

Figure 4-4 Schematic of vacuum imbibition in a capillary tube and its pressure profile.

Figure 4-4 shows a nanotube and its pressure profile. The pressure increases dramatically at the meniscus due to the existence of capillary pressure. At such a condition, the meniscus moves towards the end of the tube at the presence of capillary pressure until the tube is fully saturated with liquid (Dong et al., 2005). The vapor pressure in nanopores can be predicted by Kelvin equation as (Jatukaran et al., 2018; Powles, 1985)

$$\ln\frac{p_v}{p_s}=\frac{2\gamma V_m\cos\theta}{RT}\left(\frac{1}{r_1}+\frac{1}{r_2}\right) \tag{4.1}$$

where p_v is the actual vapor pressure, p_s is the saturated vapor pressure when the surface is flat, γ is the surface tension, V_m is the molar volume of the liquid, θ is the contact angle, R is the universal gas constant, r_1 and r_2 are radii of the meniscus, and T is temperature.

The governing equation of water flow in the inorganic pore is obtained by combining Darcy's law with the mass conservation equation. The imbibition experiments were carried out at ambient pressure. The compressibility of fluids could be neglected at ambient pressure (Alyafei et al., 2016). The mass conservation equation of water could be written as

$$\frac{\partial v_w}{\partial r}=-\phi_i\frac{\partial S_w}{\partial t} \tag{4.2}$$

The dominated force of imbibition in tight shale rock is the capillary pressure. The effect of gravity on the imbibition in tight rocks is insignificant and negligible (Zhang et al., 2019b). Thus, the gravity is not considered in the experiments and mathematical models. The Darcy velocity of water is written as follows

$$v_w = -K\frac{k_{rw}}{\mu_w}\frac{\partial p_w}{\partial r} \tag{4.3}$$

The capillary force is $p_c = p_v - p_w$, where p_w is the water pressure, p_v is the vapor pressure, which could be treated as constants for a specific sample at constant temperatures.

Therefore, the water velocity is rewritten as

$$v_w = K\frac{k_{rw}}{\mu_w}\frac{\partial p_c}{\partial r} \tag{4.4}$$

The governing equation of the water phase can be expressed as

$$\frac{1}{r^m}\frac{\partial}{\partial r}\left(r^m K\frac{k_{rw}}{\mu_w}\frac{\partial p_c}{\partial r}\right) = -\phi_i\frac{\partial S_w}{\partial t} \tag{4.5}$$

where K is the permeability of the rock, k_{rw} is the water relative permeability, μ_w is the viscosity of the oil, p_c is the capillary pressure, ϕ_i is the inorganic porosity, and m =0, 1, or 2 represents the samples with the slab, cylindrical, or spherical shapes, respectively. The rocks samples are assumed to be spherical-shaped, and the m is 2.

By use of the chain rule of derivatives, Eq. (4.5) is rewritten as

$$\frac{1}{r^2}\frac{\partial}{\partial r}\left(r^2 G_w\frac{\partial S_w}{\partial r}\right) = -\frac{\partial}{\partial t}(\phi_i S_w) \tag{4.6}$$

where $G_w = K\frac{k_{rw}}{\mu_w}\frac{\partial p_c}{\partial S_w}$ is a function of water saturation.

The relative permeability k_{rw} is treated to be 1 due to no vapor flow in the pore structure for

vacuum imbibition experiments. Capillary pressure is a function of the wetting phase saturation and could be expressed in an exponential form (Zhang et al., 2019b)

$$p_c = P_{c,\max} \exp\left[-\beta \left(\frac{S_w - S_{wi}}{1 - S_{wi} - S_{gr}} \right) \right] \tag{4.7}$$

where a_0 and b_0 are constants, $P_{c,max}$ is the maximum capillary pressure, S_w is the water saturation, S_{wi} is the initial water saturation, S_{gr} is the residual gas saturation, and β is a capillary pressure exponent. However, the liquid fully saturated the cores at the end of experiment. This exponential law was modified to match a final condition of zero capillary pressure as S_w=1. A modified capillary equation is given as

$$p_c = a_w \exp(-b_w S_w) - a_w \exp(-b_w) \tag{4.8}$$

The initial condition is expressed as

$$S_w\big|_{t=0} = 0 \tag{4.9}$$

The boundary conditions are given

$$\begin{cases} \left.\dfrac{\partial S_w}{\partial r}\right|_{r=0} = 0 \\ S_w\big|_{r=R} = 1 \end{cases} \tag{4.10}$$

The finite difference method was applied to obtain the numerical solutions of the Eq. (4.6). We adjusted a_w and b_w to match the numerical solutions and experimental results.

2.4.2. Oil Vacuum Imbibition in Shale

The mathematical model for oil vacuum imbibition is briefly described as follows:

(1) The oil flow in inorganic and organic pores at the presence of capillary pressure.

(2) Oil diffuses from pore structure into kerogen. This diffusion leads to the dissolution (absorption) of oil in kerogen.

(3) Oil adsorption on the surfaces of minerals and kerogen occurs after the oil filled the inorganic and organic pores. Therefore, the adsorption process of oil on minerals and kerogen was neglected.

The schematic of this mathematical model is shown in Figure 4-5. The total pore volume equals the total volume of free oil and adsorbed oil on minerals and kerogen surfaces.

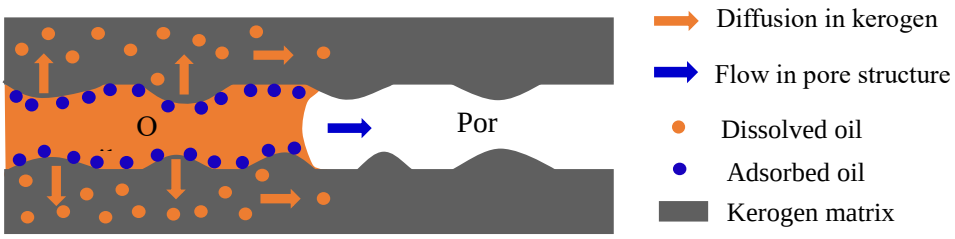

Figure 4-5 Schematic of oil storage and vacuum imbibition in shale pore structure and kerogen.

The dissolution of solute in a solution can be modeled by the Noyes-Whitney equation as follows (Hattori et al., 2013)

$$\frac{dC}{dt} = \frac{DA}{Vh}(C_{sd} - C) \tag{4.11}$$

where D is the diffusion coefficient of the solute in solution (m^2/s), A is the effective contact area between solute and solution (m^2), V is the volume of solution (m^3), h is the thickness of the diffusion layer (m), C_{sd} is the concentration of saturated solute in solution (mol/m^3), and C is the concentration of solute in the solution bulk (mol/m^3).

Based on this theory, we propose a pore-kerogen diffuse double layer model (PKDDL) for oil diffusing from pores into kerogen. In this model, diffusion leads to the dissolution and absorption of hydrocarbon in kerogen. The oil molecules diffuse through the diffuse layer and into bulk kerogen. Figure 4-6 shows the schematic of the PKDDL model.

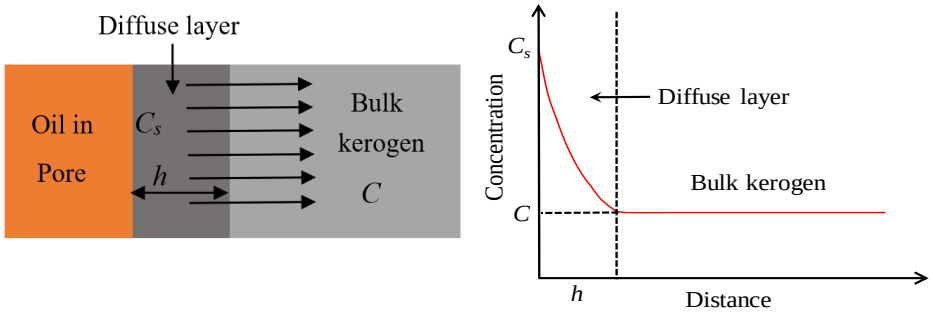

Figure 4-6 PKDDL model and hydrocarbon concentration in kerogen.

When the oil dissolves, oil molecules pass through the diffuse layer and further into the bulk kerogen until the bulk kerogen is completely saturated with oil. Variables in this model are as follows:

C_s is the concentration of oil in the contact surface between kerogen and oil in pores which also represents the saturated dissolved oil concentration in kerogen, C is the concentration of oil in bulk kerogen, and h is the thickness of the diffuse layer.

Mathematical description of PKDDL model is shown below

$$V_k \frac{dC}{dt} = \frac{D_k A}{h}(C_s - C) \tag{4.12}$$

where D_k is the effective diffusion coefficient of oil in kerogen (m^2/s) and V_k is the volume of kerogen which is written as

$$V_k = V_{rock} F \tag{4.13}$$

V_{rock} is the volume of rock and F is the volume fraction of kerogen. The volume fraction of kerogen is expressed as

$$F = TOC \frac{\rho_{rock}}{\rho_k} S_f \tag{4.14}$$

where TOC is the total organic content, ρ_{rock} is the density of rock, ρ_k is the density of dry kerogen

without dissolved oil, and S_f is the swelling factor of kerogen. The determination of swelling factors and density of kerogen are complicated issues. Because of this complication, an average swelling factor of 1.3 was used (Ertas et al., 2006; Larsen and Li, 1994), and a widely-used average density of 1.25 g/cm^3 was selected (Okiongbo et al., 2005).

The effective contact area between pore and kerogen is given as

$$A = V_{rock}\phi_t S_o EeF \tag{4.15}$$

where ϕ_t is the total porosity including inorganic and organic pores, S_o is the oil saturation in pores, E is the specific surface area of pores (m^{-1}), and e is the fractions of pore surface area contacting with kerogen.

The PKDDL model is rewritten as follows

$$F\frac{dC}{dt} = D_k\frac{\phi_t EeF}{h}(C_s - C)S_o \tag{4.16}$$

Multiplying the molar volume of oil in both sides of this equation yields

$$F\frac{dCV_m}{dt} = D_k\frac{\phi_t EeF}{h}(C_s V_m - CV_m)S_o \tag{4.17}$$

where V_m is the molar volume of oil (m^3/mol).

The PKDDL model is rewritten as follow

$$F\frac{dC_k}{dt} = J(C_{ks} - C_k)S_o \tag{4.18}$$

$$J = D_k\frac{\phi_t EeF}{h} \tag{4.19}$$

where J is the dissolution rate constant (s^{-1}), S_o is the oil saturation in pore structure, C_k is the dissolved oil saturation in kerogen, which is dimensionless and represents the dissolved oil volume per unit volume of kerogen (cm^3/cm^3), and C_{ks} represents the saturated dissolved oil saturation in

kerogen (maximal oil saturation).

The conservation equation for oil in the pore structure is expressed as

$$\frac{1}{r^m}\frac{\partial}{\partial r}(r^m K\frac{k_{ro}}{\mu_o}\frac{\partial p_c}{\partial r})+J(C_{ks}-C_k)S_o=-\phi_t\frac{\partial S_o}{\partial t} \tag{4.20}$$

where k_{ro} is the oil relative permeability, μ_o is the viscosity of the oil, and ϕ_t is the total porosity. m=2 for the spherical-shaped samples in.

If the diffusion of oil from rock surface into the deeper matrix is considered, the conservation law for oil in kerogen is written as follows

$$\frac{1}{r^m}\frac{\partial}{\partial r}(r^m D_k F\frac{\partial C_k}{\partial r})-J(C_{ks}-C_k)S_o=-F\frac{\partial C_k}{\partial t} \tag{4.21}$$

For the imbibition, the oil diffusion from the rock surface into the deeper matrix is neglected due to the extremely low diffusion coefficient. Therefore, conservation equations for oil transport in pore and kerogen are written as follows

$$\frac{1}{r^2}\frac{\partial}{\partial r}(r^2 G_o\frac{\partial S_o}{\partial r})+J(C_{ks}-C_k)S_o=-\phi_t\frac{\partial S_o}{\partial t} \tag{4.22}$$

$$J(C_{ks}-C_k)S_o=F\frac{\partial C_k}{\partial t} \tag{4.23}$$

where $G_o=K\frac{k_{ro}}{\mu_o}\frac{\partial p_c}{\partial S_o}$ is a function of oil saturation and k_{ro} is assigned to be 1 because there is no vapor flow in pores.

Oil capillary pressure is given similarly to water capillary pressure as

$$p_c=a_0\exp(-b_0 S_o)-a_0\exp(-b_0) \tag{4.24}$$

The initial conditions are as follows

$$\begin{cases} S_o\big|_{t=0} = 0 \\ C_k\big|_{t=0} = 0 \end{cases} \tag{4.25}$$

The boundary conditions are given as

$$\begin{cases} \left.\dfrac{\partial S_o}{\partial r}\right|_{r=0} = 0 \\ S_o\big|_{r=R} = 1 \end{cases} \tag{4.26}$$

Eqs. (4.22) and (4.23) are governing equations for oil transports in pore structure and kerogen, which is a system of nonlinear partial differential equations. The finite difference method was used to obtain the numerical solutions of this model. The numerical solutions and experimental results were matched by dissolution rate constant (*J)* and capillary force parameters (a_o and b_o). The capillary forces and dissolution rate constants were obtained from the matching.

3. Results and Discussion

3.1. Water Transport in Inorganic Pores

To better present the imbibition process, a parameter V, which represents the ratio of imbibed liquid volume to rock volume, is defined as $V=V_{liquid}/V_{rock}$.

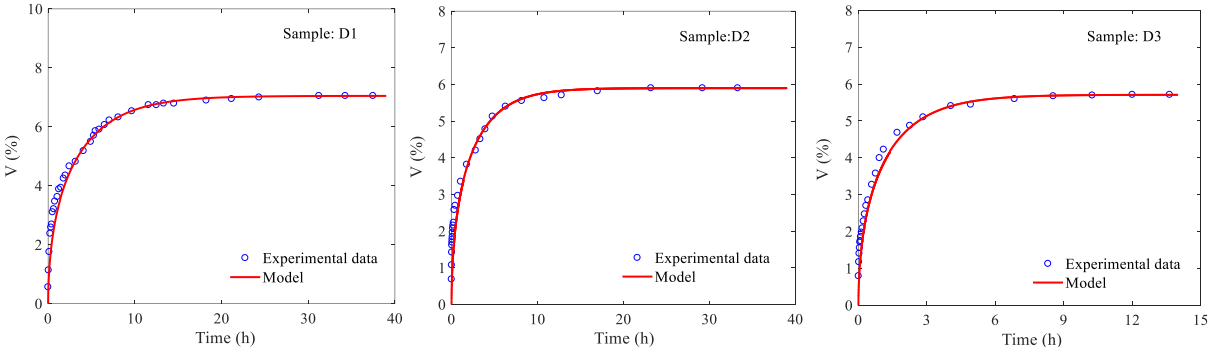

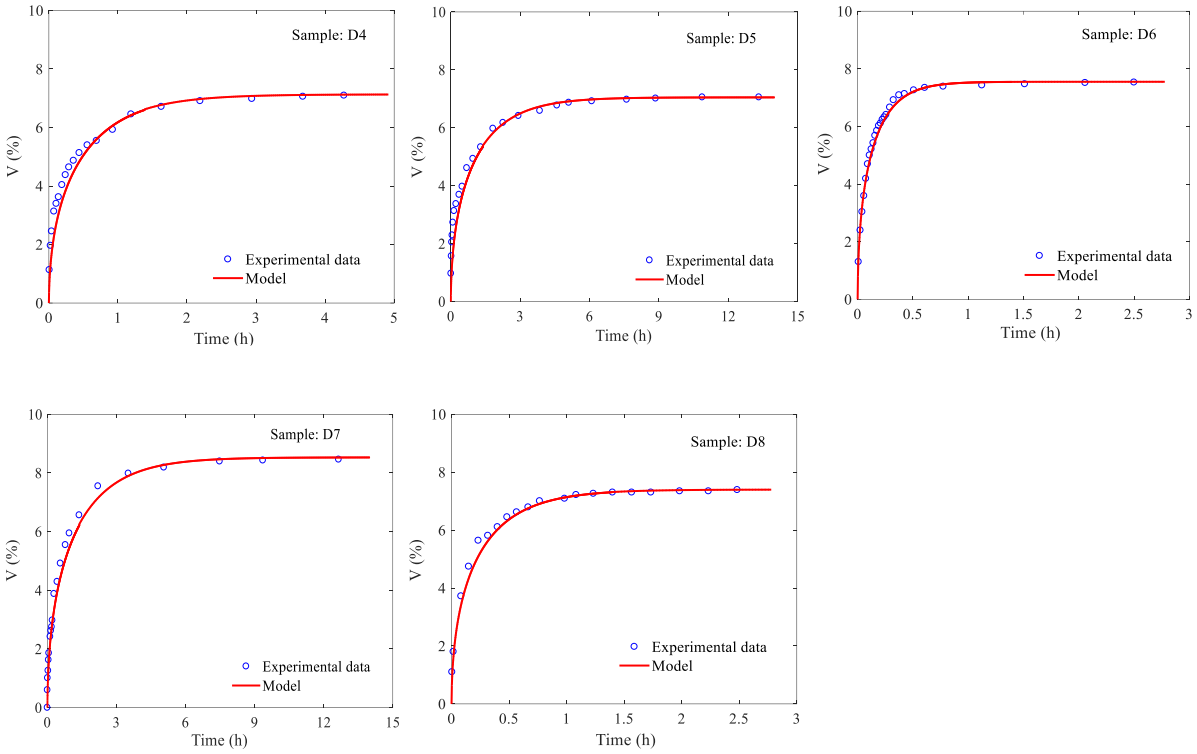

Figure 4-7 Water vacuum imbibition profiles in shale samples D1~D8.

Figure 4-7 shows the experimental and numerical results of brine vacuum imbibition. The vacuum imbibition experiment will approach stabilization after a certain time. The value of V at the equilibrium state represents the inorganic porosity, which indicates the water storage capacity. The results show that the inorganic porosity of shale samples ranges from 5.71% to 8.53%. The imbibition time varies from 0.5 to 20 hours. The water imbibition rate in core samples is impacted by boundary conditions, permeability, capillary force, and fluid viscosity (Birdsell et al., 2015; Pan et al., 2019; Qin et al., 2019; Standnes, 2004). Capillary force is the primary driving force for the vacuum imbibition process. It is well-known that the capillary at the pore scale is approximated by $2\gamma\cos(\theta)/r$, where γ, θ, and r is surface tension, contact angle, and the average pore radius of the pore, respectively. We adjusted the capillary force by changing a_w and b_w in Eq. (4.6) to match the model with experiments. The parameters used for matching are shown in Table

4-3. The results indicate that the numerical solutions of the model were in good agreement with the results of experiments. In addition, the results also suggest that samples D6 and D8 have larger capillary pressure and their imbibition times are shorter than that of the other samples. The Lucas-Washburn equation indicates that the larger the pore size the higher the imbibition rate (Cummins et al., 2017). However, experimental results in Figure 4-7 indicate that the imbibition rates of samples D5~D8 are not increased with the pore size shown in Figure 4-3. This potentially because of the heterogeneity of shale rocks, which composed of various contents of minerals, kerogen, and microfractures. The clay content, total organic content and the thermal maturity of kerogen have significant impacts on the wettability of shale rocks and potentially impact the imbibition rate (Begum et al., 2019; Siddiqui et al., 2018; Wang et al., 2018). Besides, results from literatures suggest that the imbibition rate is promoted by fractures and also impacted by pore connectivity, which could not be detected by use of the N_2 adsorption method (Jing et al., 2019; Kibria et al., 2018). Thus, the imbibition rate of shale could be controlled by both pore structures, minerals, and kerogen.

Table 4-3 Parameters of water vacuum imbibition

Samples	D1	D2	D3	D4	D5	D6	D7	D8
a_w (KPa)	9.1	12.0	13.0	21.0	18.0	55.0	35.0	58.0
b_w	0.04	0.08	0.09	0.13	0.11	0.18	0.11	0.44
ϕ_i (%)	7.05	5.90	5.71	7.13	7.05	7.55	8.53	7.40

3.2. Oil Transport in Pores and Kerogen

The oil transport mechanism in shale rock is more complicated than brine due to the existence of organic matter. For the vacuum imbibition experiments, the flow mechanisms mainly include capillary flow in the pores (inorganic and organic) and diffusion in kerogen. The rate and ability of the oil diffusion from inorganic pores to kerogen are of great interest due to the limited

study in this area.

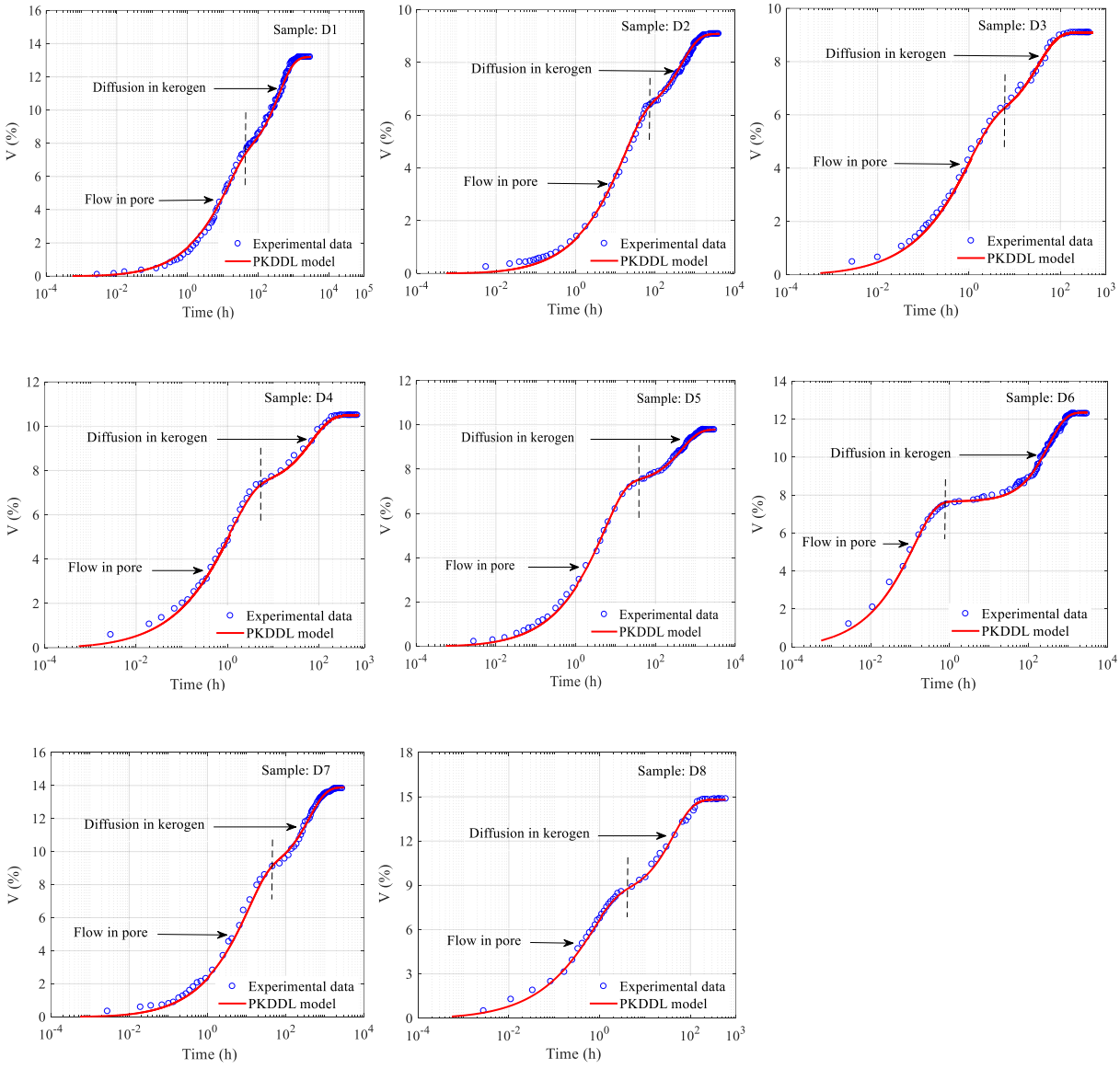

Figure 4-8 Oil vacuum imbibition in shale samples D1~D8.

Figure 4-8 shows the results of oil vacuum imbibition profiles for eight shale samples. V represents the ratio of imbibed oil volume to shale rock volume. The relationship between V and time is plotted on a semi-logarithmic coordinate. The results indicate that oil imbibition in shale samples show two stages. In the first stage, the oil was imbibed rapidly at the presence of capillary force. Capillary flow in pore structure is dominant until oil fully filled the

inorganic and organic pores. In the later stage, the oil was slowly imbibed into shale rocks. The the diffusion process, which is mainly controlled by the diffusion from pores to kerogen, dominates until the kerogen was fully saturated with oil. The inflection points, which are marked by dashed lines, can be easily recognized from the semilogarithmic coordinate and represent the total porosity including inorganic and organic pores. Figure 4-8 also shows that the experimental time of oil imbibition varies from 200-1500 hrs, which are much longer than that of water imbibition. The diffusion of oil from pore structure into kerogen is much lower than capillary flow in pore structure. The PKDDL model was matched with the experimental results by tuning the parameters. We adjusted a_o and b_o to match the early stage and then adjusted D_k and J to match the later stage of the imbibition experiments. The results suggest that the PKDDL model is verified with the experimental results. The parameters for the simulation of each shale sample using the PKDDL model are shown in Table 4-4.

To support above discussion, sample D8 was chosen as an example to analyze the oil transport in pores and kerogen. The inflection point of sample D8 occurs approximately at 4 hrs (Figure 4-8). Figure 4-9 visualizes the oil saturation in pore structure and dissolved oil saturation in kerogen for sample D8. The results indicate that the oil approximately fully filled the pore structure at the time of 4 hrs. However, the dissolved oil saturation in kerogen is less than 0.05, which is lower than 1% of the maximum dissolved oil saturation. The diffusion process is too slow to impact the capillary flow in pore structures. Hence, the inflection points can precisely represent the total porosity of shale rocks.

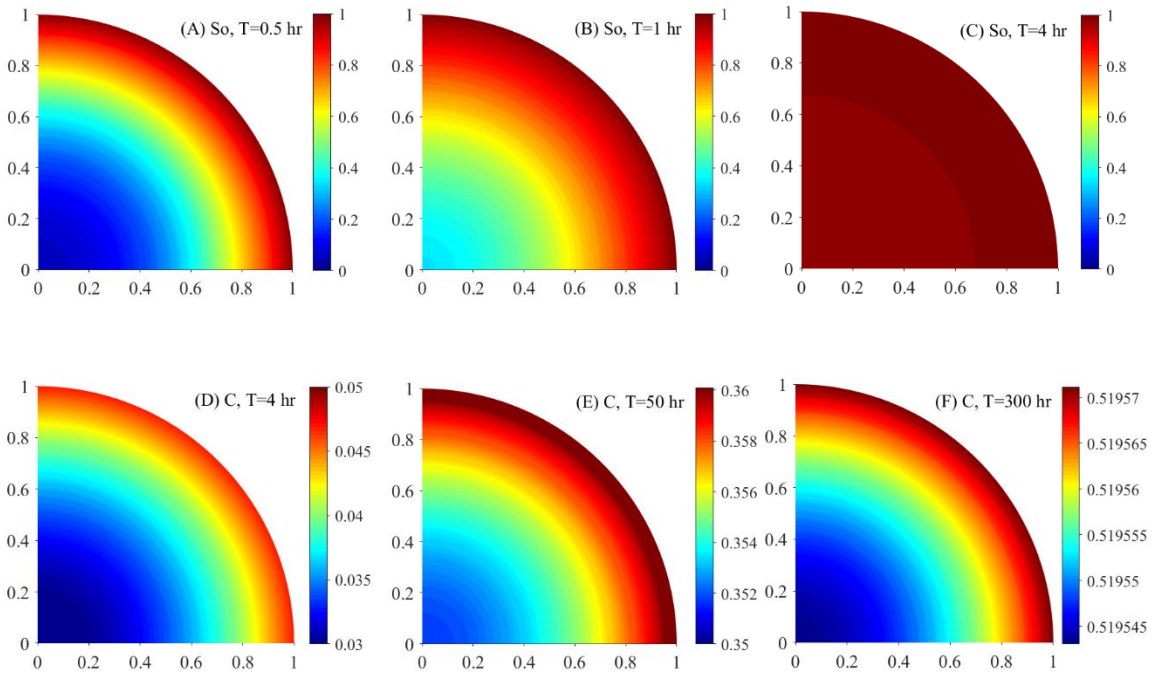

Figure 4-9 Visualization of oil flowing into the pores and diffusing into the kerogen: case study of sample D8. A-C: Relation of oil saturation (S_o) in pore structure and dimensionless radial distance; D-F: Relation between dissolved oil saturation (C) in kerogen and dimensionless radial distance.

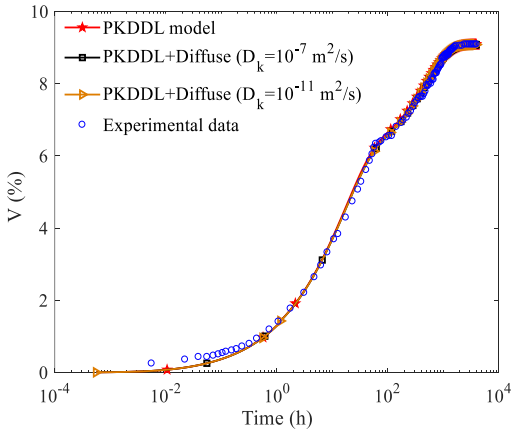

Figure 4-10 Comparison of experimental results and mathematical models with and without considering the diffusion from the rock surface into the deeper kerogen matrix for sample D2.

Figure 4-10 shows the accuracy analysis of the PKDDL model using sample D2 as an example. Mathematical models that considering and neglecting oil diffusion from the rock surface into the deeper matrix were compared. The diffusion of hydrocarbon in kerogen is extremely slow due to the ultralow diffusion coefficients of approximately 10^{-8} -10^{-12} m^2/s (Falk et al., 2015; Wang et al., 2017). The result of PKDDL model in Eqs. (4.22) and (4.23) is consistent with the results of mathematical model that consider the oil diffusion from the surface into the deeper matrix with D_k of 10^{-7} and 10^{-11} m^2/s, respectively, in Eqs. (4.21) and (4.22). The effect of oil diffusion from rock surface into deeper matrix is negligible due to extremely low diffusion coefficients. The PKDDL model is accurate to simulate the oil transfer in shale. Thus, oil diffusing from the rock surface into the deeper kerogen matrix was not considered in the modelling.

Table 4-4 Parameters for the simulation of oil vacuum imbibition in shale samples

Samples	a_o (KPa)	b_o	J (s^{-1})	ϕ_i (%)	ϕ_t (%)	F (%)	C_{ks}
D1	10.00	0.05	4.84×10^{-10}	7.05	7.35	6.88	0.85
D2	11.10	0.02	3.18×10^{-10}	5.90	6.20	6.76	0.72
D3	20.90	0.11	3.26×10^{-9}	5.71	5.91	3.77	0.85
D4	21.10	0.08	1.50×10^{-9}	7.13	7.37	3.71	0.84
D5	8.00	0.08	2.58×10^{-10}	7.05	7.31	4.24	0.58
D6	76.00	0.14	4.39×10^{-10}	7.55	7.66	5.21	0.93
D7	10.00	0.07	4.35×10^{-10}	8.53	9.02	8.65	0.56
D8	150.0	0.08	8.09×10^{-9}	7.40	8.41	13.30	0.52

3.3. Effect of R_o and TOC on Storage

The RockEval pyrolysis is a widely used technique to characterize organic matter in the source rock. While some studies from RockEval pyrolysis and N_2 adsorption have suggested that the thermal maturity R_o and TOC may impact oil storage in the inorganic pores and organic matter in shale (Li et al., 2018; Li et al., 2019; Song et al., 2019), the effects of TOC and R_o on the storage

capacity of kerogen have not been systematically studied.

The RockEval pyrolysis results, TOC, and R_o of studied shale samples are presented in Table 4-5. The vitrinite reflectance was tested, which typically represents the thermal maturity of kerogen (Fishman et al., 2012; Modica and Lapierre, 2012). The results suggest that R_o is 0.62- 1.05%. The TOC varies in the range of 1.59% to 5.97%. For kerogen of these eight shale samples, 6 samples are type II kerogen and 2 samples are type III kerogen.

Table 4-5 RockEval Pyrolysis data, TOC, and R_o for the studied shale samples

Samples	Kerogen type	Toc (%)	R_o (%)	S_1 (mg/g)	S_2 (mg/g)	S_3 (mg/g)	T_{max} (℃)	HI	OI	PI
D1	II	2.84	0.75	3.24	9.79	0.48	439	345	17	0.32
D2	II	2.28	0.79	2.29	8.53	0.21	442	374	9	0.26
D3	II	1.59	0.81	1.73	3.22	0.33	433	203	21	0.49
D4	II	1.60	0.80	2.80	5.28	0.42	419	330	26	0.49
D5	II	1.78	0.83	3.30	5.45	0.42	419	306	24	0.56
D6	III	1.90	0.62	0.60	2.81	0.26	437	148	14	0.20
D7	III	2.50	1.02	0.09	4.36	0.27	447	126	8	0.02
D8	II	5.97	1.05	0.26	20.96	0.21	447	351	4	0.01

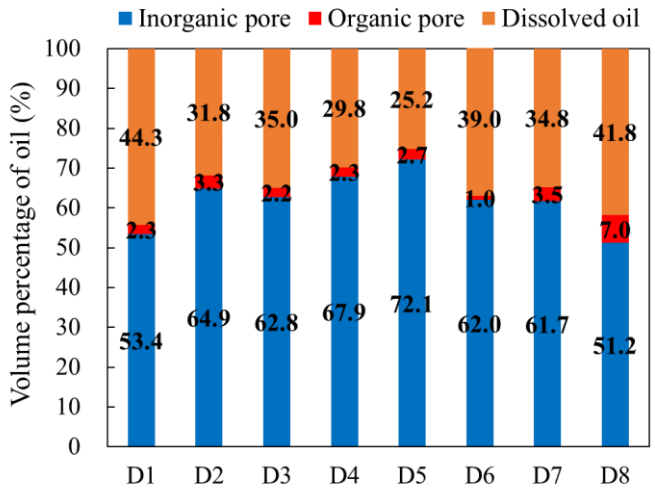

Figure 4-11 Oil percentages in the inorganic pores, organic pores, and dissolved oil in kerogen for Shahejie Formation shale rocks.

Figure 4-11 shows the oil percentages in the inorganic pores, organic pores, and dissolved oil in kerogen. The results indicate that oil volume storing in organic pores is very small approximately 1.0-7.0% of total oil. The dissolved oil in kerogen is 25.3-44.3% of total oil and is the dominant form of oil in kerogen. The total of oil in the organic pores and dissolved oil in kerogen accounts for 27.9-48.8% of total oil. On the other hand, the percentage of oil in the inorganic pores is around 51.2-72.1%. The percentage of oil in each medium could be affected by inorganic porosity, TOC, and kerogen thermal maturity. Results show that oil in inorganic pores includes free oil in pores and adsorbed oil on minerals (Wang et al., 2015). In addition, the adsorption capacity of kerogen is much higher than that of clay minerals (Sang et al., 2018). The vacuum imbibition tests are not possible to separate adsorbed oil and free oil in inorganic pores. Nevertheless, the effect of minerals on imbibed liquid volume is not considered because mineral pores are fully filled with fluids at the end of vacuum imbibition tests. The oil in kerogen includes free oil in organic pores and adsorbed oil in the kerogen matrix, which are significantly impacted by TOC and kerogen thermal maturity. In general, higher TOC shales trend to have higher oil storage capacity in kerogen. A higher thermal maturity also leads to a higher oil storage capacity in organic pores (Fishman et al., 2012; Modica and Lapierre, 2012).

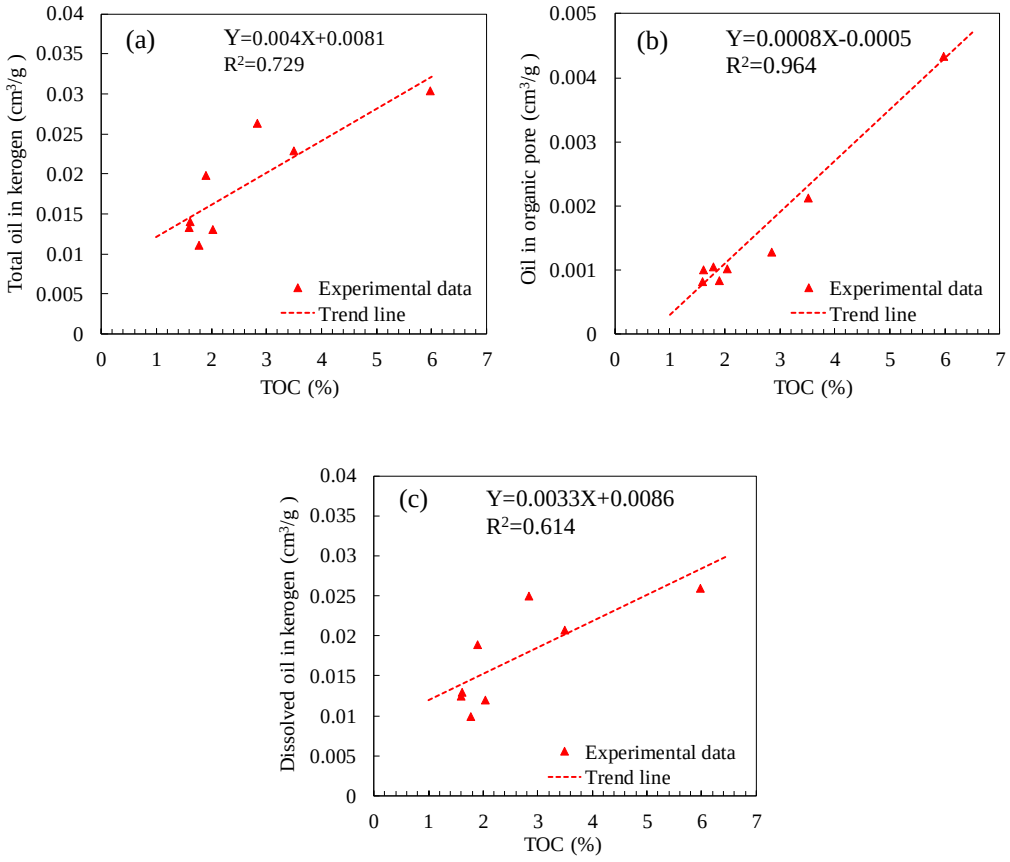

Figure 4-12 Relationship between the volume of different kinds of oil in kerogen and TOC: (a) total oil in kerogen, (b) oil in organic pores, and (c) dissolved oil in kerogen.

Figure 4-12 shows the trends of total oil in kerogen, oil in organic pores, and dissolved oil with the TOC in each gram of shale rocks. The results suggest the total oil volume storage in kerogen increases with the TOC. The higher the TOC, the larger the volume of total oil in kerogen. In addition, both the dissolved oil and oil in organic pores exhibit an incremental trend with the TOC. This is potential because the higher the TOC, the larger the volume of kerogen matrix and organic pores. Consequently, the volumes of oil in organic pores and dissolved oil increase with the TOC. Additionally, it can be seen from Figure 4-12 that the oil in organic pores is much lower than oil in inorganic pores and dissolved oil in kerogen. The results are consistent with SEM images in Fig 2, which indicate a low quantity of organic pores in studied shale rocks. Results of

linear fitting indicate that the correlation coefficients vary from 0.614 to 0.964. The dissolved oil exhibits the lowest correlation coefficient with the TOC. This is potential because the oil storage capacity of kerogen is not only impacted by TOC but also by kerogen thermal maturity. The contents of alkyl and aromatic carbons in kerogen change with thermal maturity and probably results in a variation of hydrocarbon storage capacity (Agrawal and Sharma, 2018; Wei et al., 2005).

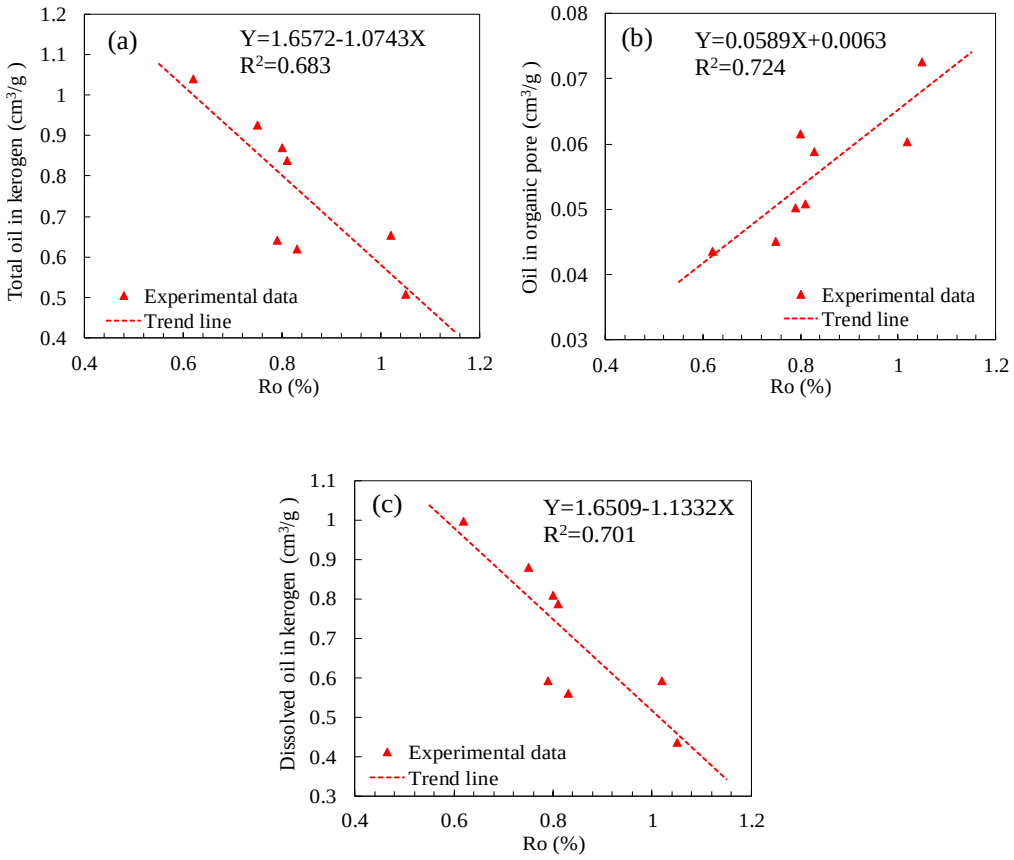

Figure 4-13 Relationship between the volumes of different kinds of oil in kerogen and Ro: (a) total oil in kerogen, (b) oil in organic pores, and (c) dissolved oil in kerogen.

Figure 4-13 shows the trends of (a) total oil in kerogen, (b) oil in organic pores, and (c) dissolved oil with R_o in each gram of kerogen. Figure 4-13b suggests that oil volume in organic pores are very small and tends to increase with thermal maturity. This is because kerogen porosity trends to increase with thermal maturity. The kerogen porosity generally shows an exponential

relationship with thermal maturity and this relationship is comparatively a linear relationship with R_o ranging from 0.5% to 1.1% (Modica and Lapierre, 2012), which is consistent with the results in our work. In addition to the oil in organic pores, much oil will be dissolved in the kerogen macerals. Figure 4-13c shows the volume of dissolved oil in kerogen with R_o. The results suggest the dissolved oil volume decreases with thermal maturity. The majority of oil in kerogen is in the form of dissolved oil within kerogen macerals. In the hydrocarbon generation period, the organic matter maturity increased and then released the hydrocarbon. It has been found that the maturation of kerogen leads to an increase in aromatic and a decrease in aliphatic carbon chains (Kelemen et al., 2007; Longbottom et al., 2016; Wei et al., 2005). Additionally, the maturation also results in a decrease in H/C ratio (Craddock et al., 2018). The rule of 'Like Dissolves Like' shows that chemicals with similar structures are more likely soluble (Montes et al., 2003). Consequently, the kerogen with high thermal maturity potentially has a larger amount of aromatic carbon chains, which has a lower ability in dissolving and absorbing alkanes, such as n-dodecane. The total oil volume in kerogen and thermal maturity are presented in Figure 4-13a. The results indicate that the total oil in kerogen tends to decrease with R_o, indicating the oil storage capacity of kerogen decreases with the thermal maturity.

4. Summary

Comprehensive rock characterizations and accurate brine/oil vacuum imbibition experiments were performed on shale rocks to investigate the storage and transport mechanisms of water and oil. Novel mathematical models were proposed to interpret the water and oil vacuum imbibition in shale. The following conclusions were drawn from the experimental and numerical studies:

1. Shale samples are very tight with a permeability of 0.007 - 0.032 mD, an average pore

diameter of 15.0 nm, and a total organic content of 1.59 - 5.97 wt%. The most abundant kerogen in these samples is type II with a thermal maturity of approximately 0.62-1.05 %.

2. For the shale rocks, the organic matter is strong oil-wet. The water is mainly stored in the inorganic pores, which account for 5.90 - 8.53% of rock's bulk volume.

3. The possible oil in inorganic pores comprises of 51.2 - 72.1% (average 62.0%) of total oil. Oil in organic pores accounts for 1.0 - 7.0% (average 3.0%) of total oil. Dissolved oil attributes to 25.2 - 44.3% (average 35.0%) of total oil. The oil present in kerogen is mainly in the form of dissolved oil.

4. For shale samples, the volume of total oil stored in kerogen generally increases with TOC. The amount of oil in organic pore increases with thermal maturity. However, the amount of dissolved oil decreases with thermal maturity. The total oil storage capacity of kerogen decreases with thermal maturity.

5. Mathematical models for brine and oil vacuum imbibition are consistent with the experimental data. The water imbibition in shale is a capillary flow. The oil imbibition in shale is a combination of capillary flow and diffusion. The pore-kerogen double diffuse layer (PKDDL) model is accurate to interpret the diffusion of oil from pores into kerogen. This diffusion leads to the dissolution (absorption) of oil in kerogen. The dissolution rate constants vary from 8.09×10^{-9} to 2.58×10^{-10} s^{-1}.

CHAPTER V

MECHANISMS OF MISCIBLE CO_2 ENHENCED SHALE OIL RECOVERY: A DIFFUSE LAYER MODEL FOR MASS TRANSFER IN ORGANIC MATTER

1. Introduction

The concentration of greenhouse gases in the atmosphere increased significantly during the last decades, especially CO_2, which is believed to contribute to global warming. Thus, it is desirable to directly capture CO_2 from large industrial source points, such as power plants, and store it before it is released into the atmosphere. Recent studies have shown that tight and shale oil formations can serve as cap rocks for CO_2 geological sequestration due to their extremely low porosity and permeability (Huo et al., 2017; Wang et al., 2017). The organic matter (kerogen) and minerals in shale reservoirs have a high adsorption capacity of CO_2 (Jeon et al., 2014; Yueliang Liu et al., 2019; Psarras et al., 2017; Zhang et al., 2020). Supercritical CO_2 geological sequestration in tight and shale formations is also considered to be economical because it simultaneously implements CO_2 sequestration and improves oil recovery. This technology has received serious attention, and increasing numbers of oil and gas producers are implementing CO_2 injection in tight and shale reservoirs (Jia et al., 2019; Jin et al., 2017).

Shale reservoirs typically have varying amounts of kerogen compared to tight reservoirs (L. Zhang et al., 2020). The existence of kerogen makes the pore structure, fluid storage, and mass transfer more complex (Yang et al., 2020). There are a large number of shale plays in the United States, such as Permian, Bakken, Eagle Ford, Marcellus, and Niobrara, which have enabled the United States to become the largest oil producer in the past decade. The Bakken Formation is

considered to be one of the largest tight and shale oil formations in North America and has an estimated 262 billion barrels of oil and 197 trillion cubic feet of gas in place (Gherabati et al., 2019). Both the inorganic and organic pores and kerogen matrix are capable of storing oil and gas (Kuang et al., 2019; Sang et al., 2018, 2016). The organic pores are created within kerogen due to maturation of organic matter during or after hydrocarbon generation (Jarvie et al., 2007). Organic pores in kerogen probably play a key role in shale oil systems because of their capability to store large volumes of hydrocarbons (Loucks et al., 2012). Results from the literature indicate that the storage capacity of organic porosity exhibits an exponentially increasing trend with its thermal maturity (R_o) (Modica and Lapierre, 2012). In addition, a higher total organic content (TOC) potentially results in a higher oil volume in kerogen matrix (Sang et al., 2018). Zhang et al. (2020) investigated the hydrocarbon storage capacity of each medium using the vacuum imbibition method. Their results suggested that oil in inorganic pores, organic pores, and dissolved oil volume in kerogen account for 51.2-72.1%, 1.0-7.0%, and 25.2-44.3% respectively of total oil in shale (Zhang et al., 2020).

Over the past decade, many efforts have been made regarding supercritical CO_2 injection in tight and shale rocks. Results suggested that both inorganic pores and kerogen can serve as feasible media for CO_2 storage (Lafortune et al., 2014; Wei et al., 2020; Yang et al., 2018). The kerogen mainly includes organic pores and carbon skeleton, which is a carbonaceous polymer material resulting from the condensation of organic residues in sedimentary rocks (Weck et al., 2017). The kerogen is capable of adsorbing and absorbing large numbers of hydrocarbons and CO_2 (Charoensuppanimit et al., 2016; Pan et al., 2019). Hydrocarbons and CO_2 can be adsorbed on kerogen surface and dissolved in kerogen matrix (Etminan et al., 2014; Tesson and Firoozabadi, 2019). For the adsorption, the mechanisms of micropores, mesopores, and macropores are different

because different adsorbate molecules diameters correspond to different pore sizes (Sarkisov and Harrison, 2011; Sui and Yao, 2016). CO_2 adsorption experiments on Bakken shale samples show that adsorption of CO_2 increased with pressure and reached a maximum value of 17 mg/g at high temperature and pressure (Jin et al., 2017). The adsorption capacity of CO_2 increased dramatically with the TOC (Aljamaan et al., 2017; Ross and Marc Bustin, 2009; Tao and Clarens, 2013). Experimental results from literature also indicate that a higher TOC results in a higher CO_2 wettability in shale rocks, suggesting that shale is a presumably feasible material for CO_2 sequestration (Pan et al., 2018). The reaction between shale and CO_2, which potentially impacts shale structure, is one of the key issues that significantly affect CO_2 geological sequestration (Wei et al., 2020). Supercritical CO_2 can be dissolved in the aqueous phase and then reacts with minerals, especially carbonate minerals (Humez et al., 2014; Mouzakis et al., 2016). The specific surface area and quantity of micropores dropped, and the average pore size increased after the shale rocks were exposed to supercritical CO_2 (Yin et al., 2016). Experiments also indicated the organic matter content of shale can be slightly decreased due to its reaction with CO_2 (Hawthorne et al., 2019b).

Extraction and diffusion of CO_2 and hydrocarbons occur as supercritical CO_2 is injected into the shale formation. Supercritical CO_2 has been widely used as an industrial solvent in liquid-liquid and liquid-solid extraction, such as extracting caffeine from coffee beans and extracting oil from soybean, sunflower, and canola seeds (Marco et al., 2018; Mendes et al., 2002; Pederssetti et al., 2011). Similarly, CO_2 is also capable of extracting hydrocarbons from organic matter in shale reservoirs. Hawthorne et al. (2019) conducted miscible CO_2 injection in a large number of shales and tight rocks. Results suggested that concentration-gradient driven diffusion is the key mechanism of CO_2 penetration in shale rocks, and the hydrocarbons are fully extracted out of shale and tight rocks (Hawthorne et al., 2019a). As the CO_2 fluid pressure is lower than the minimum

miscible pressure (MMP), the swelling of oil in shale is significant, which contributes to the recovery of oil from cores (Li and Dong, 2009). Zhu et al. (2018) investigated CO_2 diffusion in different shale cores. The diffusion of CO_2 in shale was simulated by a traditional diffusion equation. Their results suggested the effective diffusion coefficients of CO_2 vary from $3.0\text{-}12.5\times10^{-6}$ cm^2/s (Zhu et al., 2018). The huff-n-puff is a widely used method to apply CO_2 injection in tight and shale reservoirs. This process includes three main steps, as follows: the CO_2 is injected at the "huff" step, the well is shut-in at the "soak" step, and oil is produced at the "puff" step (Jia et al., 2019). Yu et al. (2015) conducted sensitivity analyses of CO_2 diffusion coefficients for huff-n-puff in Bakken tight reservoirs. Results suggested that CO_2 diffusion plays a significant role in improving oil recovery in tight reservoirs (Yu et al., 2015). However, the kerogen is always underestimated in the current mathematical models regarding mass transfer of CO_2 and hydrocarbons in shales due to complex mass transfer mechanisms.

In this work, mechanisms of molecular diffusion and extraction for supercritical CO_2 injection in tight and shale rocks were investigated. A novel pore-kerogen diffuse layer model was proposed to capture the mass flux between pores and kerogen matrix in oil shale. Mathematical models of mass transfer in cores and crushed samples were derived. Comprehensive rock characterizations and CO_2 injection experiments were carried out on shales and tight rocks. Mathematical models were matched with experimental results by tuning the necessary parameters.

2. Mathematical Models and Experiments

2.1. Experimental Setup

Hawthorne et al. (2019) and Jin et al. (2017) conducted miscible CO_2 injection and extraction experiments (Hawthorne et al., 2019b; Jin et al., 2017). The schematic of the experimental design is shown in Figure 5-1. The ISCO pump was operated in the constant pressure

mode to inject CO_2 into the 10 mL sample cell at a constant pressure of 34.5 MPa. Core plugs and crushed samples were placed into the sample cell at a temperature of 110 ℃. The pressure and flow rate of the ISCO pump were calibrated before the experiments. The sizes of the extraction cell and the rock samples were also measured and calibrated. The dimensions of the experimental setup and samples are shown in Table 5-1. The rock cores and the crushed samples were not confined, which allowed the CO_2 to flow freely around them. This design is typically used to mimic the flow in fractured tight and shale reservoirs systems. The CO_2 injection experiments on cores and crushed samples were performed separately. The valve behind the sample cell was opened at the soak stage. After the soak period, CO_2 and hydrocarbons were produced via the heated flow restrictor with a rate of 1.5 ml/min. The ISCO pump is capable of pumping the fluid up to 90ml/min. The pressure remained constant during the soak and production processes. Recovered hydrocarbons were collected hourly by slowly depressurizing the CO_2 into a solvent (methylene chloride). Hydrocarbon recovery data in this paper was from previous publications (Hawthorne et al., 2019a; Hawthorne et al., 2019b).

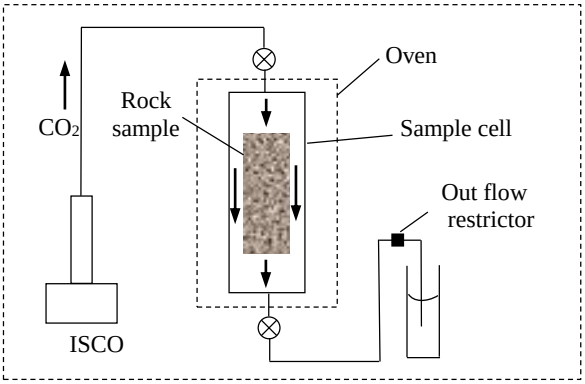

Figure 5-1 Schematic of the experimental setup of miscible CO_2 injection (Hawthorne et al., 2019a; Jin et al., 2017).

Table 5-1 Dimensions of the experimental setup and samples

Items	Diameter (mm)	Length (cm)
Sample cell	15.0	5.6
Core plugs	11.2	4~5
Crushed samples	1-3.4	-

2.2 Sample characterizations

The Bakken oil system generally has four members, from top to bottom: Upper Bakken, Middle Bakken, Lower Bakken, and the Three Forks. The Upper and Lower Bakken are typically shale rocks that have a total organic content of approximately 10%-15% and an average pore radius of 3-7 nm (Jin et al., 2017). The Middle Bakken is mainly tight limestone with a pore diameter of 0.3-200 nm and a porosity of 3.6%-8.4% (Zhang et al., 2019a, 2019b). In work, fourteen samples were collected from wells W1, W2, and W3 in western North Dakota. The acronyms, UBS, MB, and UBS represent the Upper Bakken shale, Middle Bakken, and Lower Bakken shale, respectively. The gas porosity, density, and TOC of the studied samples are shown in Table 5-2. The total organic content data was obtained from the Rock-Eval pyrolysis.

The Rock-Eval pyrolysis and TOC data for samples from well W1 are shown in Table 5-3. Through cross plots of pyrolysis parameters, such as hydrogen index (HI) against oxygen index (OI) and HI against T_{max}, the kerogen type in those Bakken shales has been determined. In general, a Type II marine oil-prone kerogen is the major type of kerogen found in those Bakken shales. The TOC of the collected samples varies from 9.5-11.82wt%.

Table 5-2 Porosity, rock density, and TOC data of studied samples

Samples	Density (g/cm^3)	Porosity (%)	TOC (wt %)
W1LBS1	2.43	8.89	11.38
W1LBS2	2.42	8.53	11.29
W1LBS3	2.43	8.02	10.43
W1UBS1	2.43	9.97	10.29
W1UBS2	2.47	10.29	9.50
W1MB1	2.73	2.30	-
W1MB2	2.74	7.47	-
W1MB3	2.71	9.86	-
W1MB4	2.73	10.02	-
W2LBS1	2.45	2.70	11.82
W2UBS1	2.45	8.80	10.38
W2UBS2	2.41	5.60	10.00
W2MB3	2.71	8.30	-
W3LBS	2.45	8.40	11.30

Table 5-3 Pyrolysis data of Bakken shale samples from well W1

Samples	Kerogen type	TOC (wt%)	S_1 (mg/g)	S_2 (mg/g)	S_3 CO_2 (mg/g)	S_3 CO (mg/g)	T_{max} (℃)	HI	OI	PI
W1LBS1	II	11.38	0.34	12.33	0.17	0.05	460	108	1.55	0.03
W1LBS2	II	11.29	0.5	12.18	0.18	0.06	459	108	1.53	0.04
W1LBS3	II	11.43	0.69	12.20	0.12	0.05	458	107	1.04	0.05
W1UBS1	II	10.29	1.50	12.71	0.23	0.04	461	122	2.22	0.11
W1UBS2	II	9.50	0.46	10.37	0.20	0.04	461	109	2.11	0.04

2.3. Pore-Kerogen Diffuse Layer Model

Figure 5-2 shows scanning electron microscopy (SEM) images of shale and tight rock samples. The Helios650 FIB-SEM equipment is able to provide high-resolution SEM images. The images are with 2.00kv accelerating voltage and 26000 times of magnification. The dark areas are

organic matter, which is capable of adsorbing and absorbing hydrocarbons and CO_2. The light grey areas are minerals, such as quartz, clay, calcite, and dolomite. In general, three types of pores were observed from the SEM images: inorganic pores (between or within minerals), organic pores (within organic matter), and organic-mineral pores (between organic matter and minerals). The schematic of the mass transfer mechanisms between pores and kerogen is shown in Figure 5-3. Hydrocarbons diffusion from kerogen to pores leads the extraction. CO_2 can diffuse into the kerogen and be absorbed by kerogen.

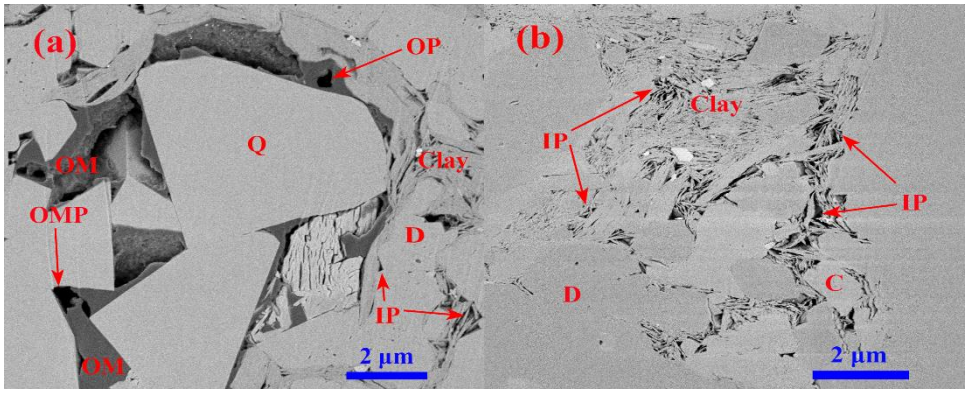

Figure 5-2 SEM images of shale sample (a) and tight rock sample (b). OM (organic matter), OP (organic pore), IP (inorganic pore), OMP (organic-mineral pore), Q (quartz), D (dolomite), C (calcite).

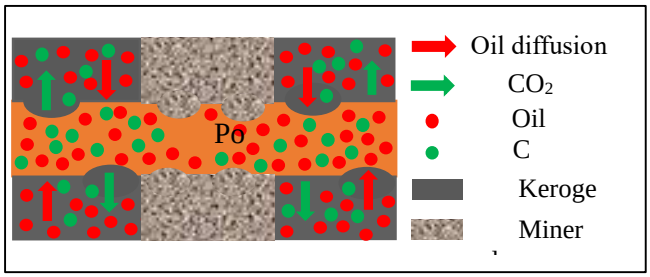

Figure 5-3 Schematic of diffusion in shale rock for CO_2 injection.

The schematic of PKDL model and the hydrocarbon concentration profile in kerogen are illustrated in Figure 5-4. The diffusion flux between kerogen and pores can be determined from

this model. A brief description of this model is given as follows:

(1) The major diffusion resistance occurs in the diffuse layer. This diffusion layer dominates the mass transfer between pores and kerogen.

(2) The hydrocarbons and CO_2 can diffuse through this diffuse layer. The diffusion obeys Fick's law. The diffusion through this diffuse layer is an unsteady-state process, as shown in Figure 5-4.

(3) The hydrocarbon concentration at this contact surface (between kerogen and pores) and hydrocarbon concentration in pores obeys the extraction distribution law.

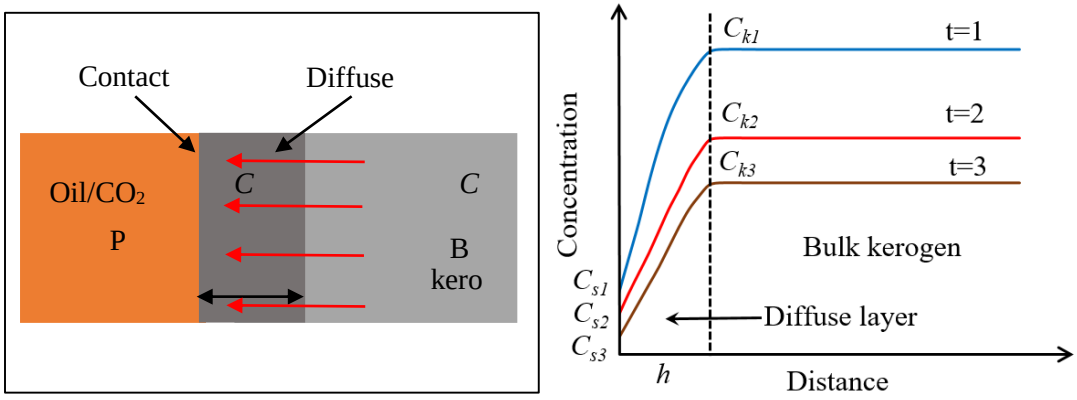

Figure 5-4 Schematic of a pore-kerogen diffuse layer model and hydrocarbon concentration in kerogen.

The main advantage of this model is that the sizes and shapes of the kerogen particles have no impact on extraction and diffusion equations. In this model, oil molecules can be extracted out of the bulk kerogen and diffuse into pores through this diffuse layer. The first assumption is reasonable because of the theory of membrane mass transfer. Several studies suggested that major mass transfer resistance between two immiscible phases mainly happens in a membrane next to the interface (Atchariyawut et al., 2008; Mavroudi et al., 2006; Zeng et al., 2016). In addition, Zhang et al. (2020) investigated the dissolution of hydrocarbon in kerogen and concluded that

hydrocarbon dissolution in kerogen can be simulated by a double diffuse layer model (Zhang et al., 2020). The extraction distribution law applies at the contact surface between pores and kerogen because the supercritical CO_2 and solid kerogen are immiscible. The extraction process occurs as the solubilities of hydrocarbons in supercritical CO_2 and kerogen are different. Extraction of hydrocarbons from kerogen by use of CO_2 is a liquid-solid extraction, which has wide applications in the industry (Wang et al., 2019). The concentration of hydrocarbon at this contact surface can be determined by the distribution law, which can be written as follows:

$$C_s = \frac{C_c}{K_D} \tag{5.1}$$

where C_c is the oil concentration in CO_2 (mol/m^3), C_s is the oil concentration at the contact surface between pores and kerogen (mol/m^3), and K_D is the distribution coefficient.

Both literature and SEM images (Figure 5-2) of shale have confirmed that the kerogen spatial distribution is not continuous (Huang et al., 2020). Thus, the mass transfer between kerogen particles is not considered. Fick's law shows that the mass flux leaving the kerogen can be written as:

$$V_k \frac{\partial C_k}{\partial t} = -\frac{D_k A}{h}(C_k - C_s) \tag{5.2}$$

where D_k is the hydrocarbon diffusion coefficient in kerogen (m^2/s), A is the effective contact area between CO_2 and kerogen (m^2), C_k is the hydrocarbon concentration in bulk kerogen (mol/m^3), h is the diffuse layer thickness (m), and V_k is the kerogen volume (m^3), which is given as:

$$V_k = V_{rock} F \tag{5.3}$$

where V_{rock} is the rock volume and F is the volume fraction of kerogen.

$$F = TOC \frac{\rho_{rock}}{\rho_k} S_f \tag{5.4}$$

where TOC is the total organic content (wt%), ρ_{rock} is the rock density, ρ_k is the density of dry kerogen, and S_f is the swelling factor of kerogen that is saturated with hydrocarbons. Due to the complex work of determining the swelling factor and density, a widely used swelling factor of 1.3 and an average density of 1.25 g/cm^3 were selected in this work (Ertas et al., 2006; Larsen and Li, 1994; Okiongbo et al., 2005). The average value of saturated C_k is approximately 0.73 for type II kerogen in shale oil reservoirs (Zhang et al., 2020).

To reduce the mathematical workload in the simulation, Eq. (5.2) was rewritten into a dimensionless equation by multiplying the molar volume

$$F\frac{\partial C_k V_m}{\partial t} = -D_k \frac{A}{h}(C_k V_m - \frac{V_m C_c}{K_D}) \tag{5.5}$$

where V_m is the molar volume of hydrocarbon (m^3/mol). Eq. (5.5) is rewritten as follows:

$$F\frac{\partial C_K}{\partial t} = -D_k \frac{A}{h}(C_K - \frac{C}{K_D}) \tag{5.6}$$

where C_K is the dissolved oil saturation in kerogen, which represents oil volume in unit volume of kerogen and is dimensionless (m^3/m^3), and C represents the effective oil volume fraction in pores and is dimensionless (m^3/m^3).

The effective contact area (A_{pk}) between pores and kerogen is given as:

$$A_{pk} = V_{rock}\phi_t EGF \tag{5.7}$$

where ϕ_t is the total porosity, which includes inorganic pores and organic pores, E is the specific surface area of pores (m^{-1}), and G is the fractions of pore surface area that has contact with kerogen.

The volume fraction of hydrocarbons has an impact on the effective contact area between CO_2 and kerogen. Thus, the effective contact area between the solvent and kerogen was written as a linear function of oil volume fraction in pores. A modified effective contact area (A) between

CO_2 and kerogen is given as:

$$A = V_{rock}\phi_t EGF(1-C) \tag{5.8}$$

The effective contact area is zero before CO_2 enters the pores (C=1 and oil fully saturated pores). The effective contact area A equals A_{pk} under a condition of C=0, which means pores are fully saturated with CO_2.

Eq. (5.6) is rewritten as follows:

$$F\frac{\partial C_K}{\partial t} = -D_k\frac{\phi_t EGF}{h}(1-C)(C_K - \frac{C}{K_D}) \tag{5.9}$$

$$F\frac{\partial C_K}{\partial t} = -J(1-C)(C_K - \frac{C}{K_D}) \tag{5.10}$$

$$J = D_k\frac{\phi_t EGF}{h} \tag{5.11}$$

where J is an extraction rate coefficient (s^{-1}).

2.4. Samples in Spherical Shape

2.4.1 Spherical Tight Sock

Figure 5-5 shows the schematic of the mass transfer of hydrocarbons and CO_2 for spherical samples. For tight rocks, the mechanism of hydrocarbon recovery for miscible CO_2 injection is a diffusion process. Hydrocarbons diffuse from the deeper matrix to the rock surface. The fluid flow is not considered because the experiments were conducted under constant pressure condition. Thus, the pressure gradient in rocks samples can be neglected.

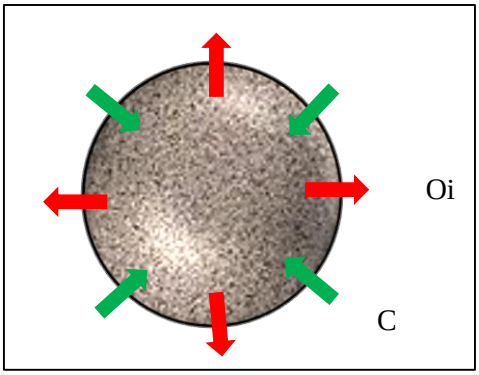

Figure 5-5 Schematic of CO_2 injection in samples with a spherical shape.

The conservation equation of hydrocarbons can be written as:

$$D_e \frac{\partial^2 C}{\partial r^2} + \frac{2D_e}{r}\frac{\partial C}{\partial r} = \phi \frac{\partial C}{\partial t} \tag{5.12}$$

where C is a dimensionless concentration of hydrocarbons in pores, ϕ is the rock porosity (%), and D_e is the effective diffusion coefficient of hydrocarbons in rock (m^2/s). The effective diffusion coefficient is lower than the real diffusion coefficient in bulk liquid and can be expressed as (Jia et al., 2019):

$$D_e = \phi D / \tau \tag{5.13}$$

where D is the diffusion coefficient in the bulk liquid phase (m^2/s) and τ is the diffusive tortuosity factor of the porous media. Theoretical studies have shown that the pore size and pore geometry can significantly impact the effective diffusion coefficient (Elwinger et al., 2017; Hu et al., 2018; Yuan et al., 2014). Other factors, such as temperature, pressure, oil saturation, and permeability also significantly impact the effective diffusion coefficient (Li et al., 2016). Due to the complex pore structure of shale rocks, those factors were not considered, and the effective diffusion coefficients were used in the model.

The boundary conditions and initial condition of this model are given as:

$$\begin{cases} \left.\frac{\partial C}{\partial r}\right|_{r=0} = 0 \\ C\big|_{r=R} = C_o \end{cases} \tag{5.14}$$

$$C\big|_{t=0} = C_i \tag{5.15}$$

where C_0 is the outer boundary condition of hydrocarbons in steel sample cell and C_i is the dimensionless concentration of hydrocarbons in pores at initial time. C_i is approximately 1 for the experiments.

The Eq. (5.12) is a linear partial differential equation and its analytical solution can be written as follows (Polyanin et al., 2015):

$$\frac{C - C_{r=R}}{C_i - C_{r=R}} = \frac{2R}{\pi r}\sum_{n=1}^{\infty}\frac{(-1)^{n+1}}{n}\sin(\frac{n\pi r}{R})\exp(-\frac{D_e n^2\pi^2 t}{\phi R^2}) \tag{5.16}$$

where $C_{r=R}$ is the boundary condition, C_i is the initial condition, and R is the radius of the spherical sample.

The oil recovery can be calculated from the difference between the total oil at the initial condition and the integral of Eq. (5.16). By applying initial and boundary conditions, the analytical solution of hydrocarbon recovery for the spherical tight sample is written as:

$$F_t = 1 - \frac{6}{\pi^2}\sum_{n=1}^{\infty}\frac{1}{n^2}\exp(-\frac{D_e n^2\pi^2 t}{\phi R^2}) \tag{5.17}$$

2.4.2 Spherical Shale Rock

For crushed shale samples, the samples are considered to be spherical-shaped, and the fluid flow in not considered. The conservation equation of hydrocarbon in pores is written as:

$$D_e\frac{\partial^2 C}{\partial r^2} + \frac{2D_e}{r}\frac{\partial C}{\partial r} + J(1-C)(C_K - \frac{C}{K_D}) = \phi_t\frac{\partial C}{\partial t} \tag{5.18}$$

The conservation equation of hydrocarbon in bulk kerogen is given in Eq. (5.10).

$$F\frac{\partial C_K}{\partial t} = -J(1-C)(C_K - \frac{C}{K_D}) \tag{5.10}$$

where J is the extraction rate coefficient, as shown in Eq. (5.11).

The boundary and initial conditions are shown as follows:

$$\begin{cases} \left.\frac{\partial C}{\partial r}\right|_{r=0} = 0 \\ C\big|_{r=R} = C_o \end{cases} \tag{5.19}$$

$$\begin{cases} C\big|_{t=0} = C_i \\ C_K\big|_{t=0} = C_m \end{cases} \tag{5.20}$$

where C_0 is the hydrocarbon concentration in the extraction cell, C_i is the dimensionless concentration of hydrocarbons in pores at initial time, and C_m is the dissolved oil volume fraction in kerogen. C_i is approximately 1 for the experiments. C_m is approximately 0.73 for type II kerogen in shale oil reservoir (Zhang et al., 2020).

2.5. Samples in Cylindrical Shape

2.5.1 Cylindrical Tight Rock

Figure 5-6 shows the mass transfer of hydrocarbons and CO_2 in a cylindrical sample. Hydrocarbons can diffuse out of the sample from the top, bottom, and side faces when all faces are exposed to CO_2. The tight and shale rocks are highly heterogeneous porous media. The permeability and diffusion coefficients can show significant differences in the directions perpendicular and parallel to the bedding because the pore structures, tortuosity, and constrictivity are often anisotropic in nature (Sato et al., 2019; Yang et al., 2016). Thus, it is essential for the model to consider the heterogeneity of the diffusion coefficient. The fluid flow is not considered.

The governing equation of hydrocarbon in pores is given as:

$$D_{er}\frac{\partial^2 C}{\partial r^2}+\frac{D_{er}}{r}\frac{\partial C}{\partial r}+D_{ev}\frac{\partial^2 C}{\partial z^2}=\phi\frac{\partial C}{\partial t} \tag{5.21}$$

where D_{er} is an effective diffusion coefficient in the radial direction (m^2/s), D_{ev} is an effective diffusion coefficient in the vertical direction (m^2/s), r is the radial distance (m), and z is the vertical distance from the rock center (m).

The boundary conditions are

$$\begin{cases}\left.\frac{\partial C}{\partial r}\right|_{r=0}=0,\left.\frac{\partial C}{\partial z}\right|_{z=0}=0\\ C|_{r=R}=C_o, C|_{z=L}=C_o\end{cases} \tag{5.22}$$

where z=0 denotes the middle of the core and z=L represents the top or bottom surface.

The initial conditions are shown in Eq. (5.20).

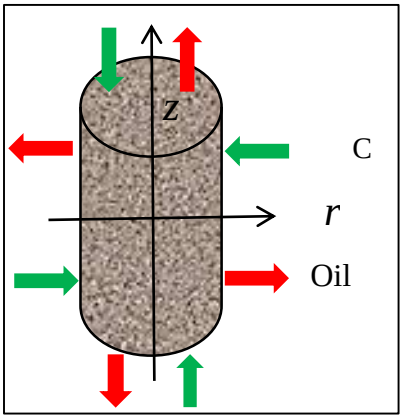

Figure 5-6 Schematic of supercritical CO_2 injection in samples of a cylindrical shape.

2.5.2 Cylindrical shale rock

Shale is also heterogeneous rock and its diffusion coefficients in radial and vertical directions are presumably different. The fluid flow is not considered due to the constant pressure condition. The governing equation of hydrocarbons in pores is written as follows:

$$D_{er}\frac{\partial^2 C}{\partial r^2}+\frac{D_{er}}{r}\frac{\partial C}{\partial r}+D_{ev}\frac{\partial^2 C}{\partial z^2}+J(1-C)(C_K-\frac{C}{K_D})=\phi_t\frac{\partial C}{\partial t} \tag{5.23}$$

The mass conservation equation of hydrocarbons in bulk kerogen is given in Eq. (5.10).

$$F\frac{\partial C_K}{\partial t}=-J(1-C)(C_K-\frac{C}{K_D}) \tag{5.10}$$

where J is the extraction rate coefficient, as shown in Eq. (5.11).

The boundary conditions are shown in Eq. (5.22) and initial conditions are shown in Eq. (5.20).

The mathematical models were solved using an implicit finite difference method in MATLAB. The oil concentration can be obtained from the numerical solutions. The oil volume was obtained from the integral of oil concentration. The mathematical models were matched with the experimental data by adjusting diffusion coefficients, extraction rate coefficients, and distribution coefficients. The distribution coefficients are independent of pore structure and were found to be a constant of approximately 5 for all Bakken shale samples.

3. Results and Discussion

3.1. CO_2 Injection in Tight Rocks

Figure 5-7 shows the hydrocarbon recovery of crushed samples from the Middle Bakken member. Experimental results show that all hydrocarbons have been recovered from crushed tight samples after approximately two hours due to the large contact areas with supercritical CO_2. In addition, results also suggest the numerical solution is consistent with the analytical solution, as shown in Eq. (5.17). The effective diffusion coefficients were obtained from the matching and are shown in Table 5-4. The hydrocarbons diffuse out of rock samples, and CO_2 diffuses into the rock

samples. Diffusion is the main mechanism by which CO_2 is able to penetrate the reservoirs (Hawthorne et al., 2019a). Molecular diffusion coefficients mainly determine the hydrocarbon recovery rates. The effective diffusion coefficients are 1.3-1.5×10^{-7} m^2/s, which are much larger than the diffusion coefficients from the literature under immiscible and much lower temperature conditions (Li and Dong, 2009; Zhu et al., 2018). Since the Bakken crude oil and CO_2 are miscible at a pressure of 34.5MPa and a temperature of 110 ℃ (Hawthorne et al., 2016), it is expected and reasonable that the diffusion coefficients are much higher under higher temperature and miscible conditions (Cadogan et al., 2016).

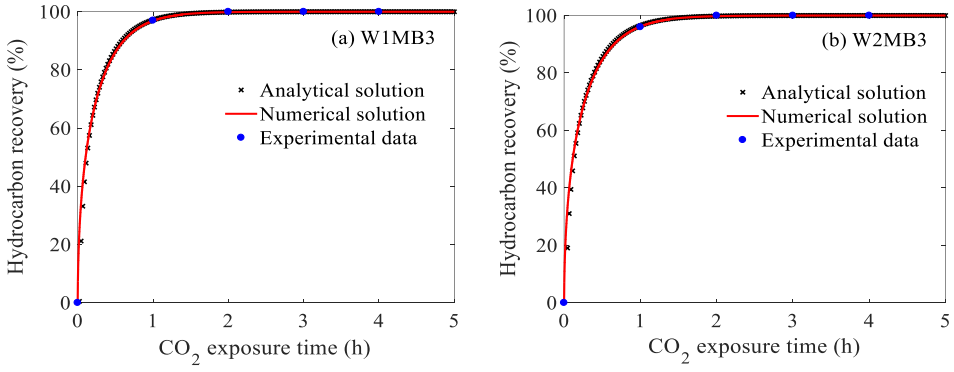

Figure 5-7 Hydrocarbon recovery for spherical tight rock samples from wells W1 and W2.

Table 5-4 Parameters of the history matching for tight spherical tight samples

Samples	Diffusion coefficient (10^{-7} m^2/s)	Diameter (mm)	Porosity (%)
W1MB3	1.5	1.7	9.86
W2MB3	1.3	1.7	5.60

Figure 5-8 shows the hydrocarbon recovery of four Middle Bakken cores. The diameters and lengths of those tight cores were approximately the same. The results indicate that oil recovery increases dramatically at the early stage and yields a recovery of higher than 80% for seven hours. The hydrocarbons were approximately fully recovered after 20 hours. Figure 5-8 shows that the

recovery rate of MB4 is roughly the same as MB3, and higher than MB2 and MB1. The results agree well with the diffusion coefficients (Table 5-5), which show an increasing trend for samples MB1-MB4. The mathematical models are in agreement with the experimental data. The visualization of oil in pores for sample W1MB4 is shown in Figure 5-9. The dimensionless oil concentration is lower than 0.001 after 20 hours, which is consistent with Figure 5-8, where the oil is totally recovered after approximately 18 hours. Moreover, the diffusion coefficients in the vertical direction are approximately 1.2 times that in the radial direction. The reason for the differences is that the cores are drilled parallel to bedding, while the vertical direction is parallel to bedding; the radial is half parallel and half perpendicular to bedding. The diffusion coefficient in the radial direction is expected to be lower than that in the vertical direction due to its lower permeability (Sato et al., 2019). Additionally, the oil concentration drop mainly appears in the radial direction, indicating that the oil is mostly produced from the radial direction rather than the end faces. Though the diffusion coefficient in the radial direction is slightly lower, its contact surface area with CO_2 is much larger.

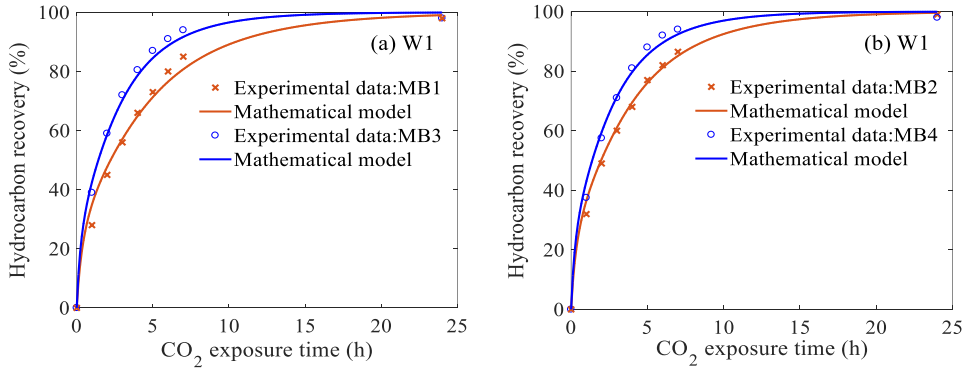

Figure 5-8 Hydrocarbon recovery of tight Bakken core plugs from well W1.

Table 5-5 Parameters of the matching for Middle Bakken cores from well W1

Samples	Diameter (cm)	Length (cm)	Porosity (%)	D_{ev} (10^{-7} m^2/s)	D_{er} (10^{-7} m^2/s)

W1MB1	1.12	4.2	2.30	0.65	0.49
W1MB2	1.12	4.2	7.47	2.30	1.90
W1MB3	1.12	4.2	9.86	4.20	3.60
W1MB4	1.12	4.2	10.20	4.80	4.10

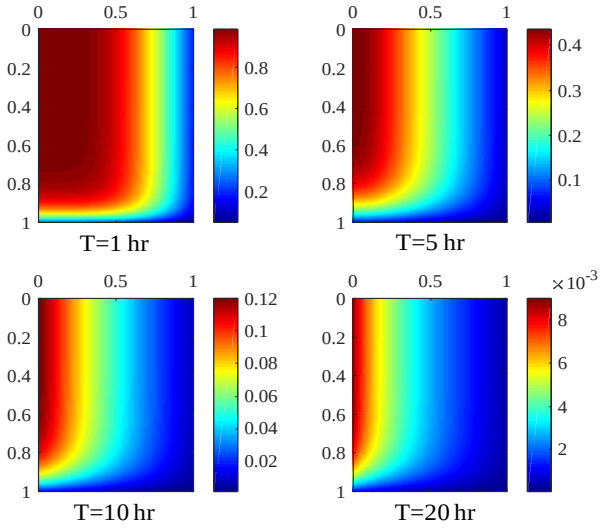

Figure 5-9 Visualization of hydrocarbon dimensionless concentration in tight MB4 sample. The X-axis is the dimensionless radius, the Y-axis is dimensionless half-length, and the original point is the center of the core.

3.2. CO_2 Injection in Shale Rocks

Figure 5-10a displays the history matching of hydrocarbon recovery of crushed shale samples with an average diameter of approximately 1.7 mm. The hydrocarbon recovery increased dramatically before five hours and reached a final value of 100% after 18 hours. The hydrocarbons recovery process in shale is much longer than that in tight Bakken rocks (Figure 5-7). For tight rocks, the hydrocarbons diffuse from the rock center to the rock surface through inorganic pores. In contrast, the recovery of hydrocarbons in shales includes two stages: (1) diffuse out from kerogen matrix to pores (organic pores and inorganic pores) through the diffuse layer (Figure 5-3), and (2) diffuse from rock center to rock surface through pores. Thus, the recovery of hydrocarbons

in shales is slower than that in tight rocks, which only needs approximately two hours (Figure 5-7). Results also confirm that the PKDL model is consistent with the experimental data. The relative errors of the PKDL model are shown in Figure 5-10b. The relative errors range from -5% to 4%, which indicates very small errors between the PKDL model and experiments. Figure 5-11 shows the hydrocarbon concentration in pores and bulk kerogen for sample W1LBS3. The parameters used for the history matching are shown in Table 5-6. The effective diffusion coefficients vary from 1.8-3.3×10^{-7} m^2/s, and the extraction rate coefficients vary from 2.1-4.9×10^{-5} s^{-1}. The driving force for diffusion through the diffuse layer is the concentration gradient between bulk kerogen and the contact surface, as shown in Figure 5-3. The hydrocarbon recovery from kerogen is an extraction process because it occurs when a chemical has different solubilities in two non-miscible phases, such as liquid-liquid and liquid-solid (Chen et al., 2020; Leybros et al., 2017). CO_2 plays a key role as a solvent to extract hydrocarbons from kerogen.

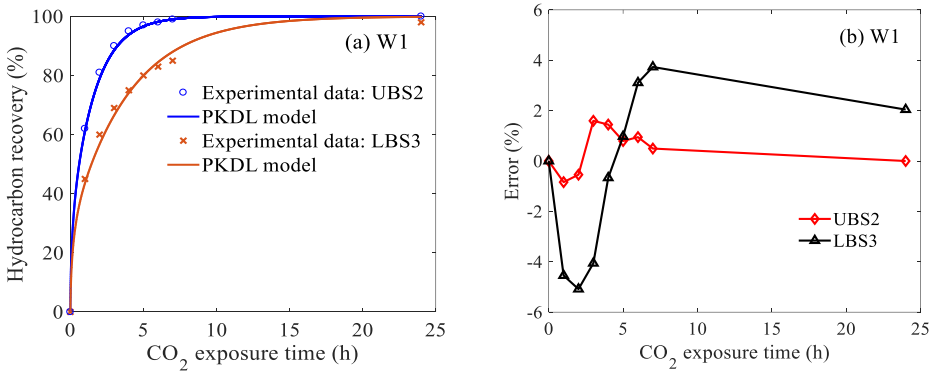

Figure 5-10 History matching using PKDL Model for crushed shale samples from well W1 (a) and relative error (in %) between the PKDL model and experiments (b).

Table 5-6 Parameters of the simulation for spherical Bakken shales

Samples	Diameter (mm)	Porosity (%)	D_e (10^{-7} m^2/s)	J (10^{-5} s^{-1})	F (%)	K_D
W1UBS2	1.7	10.29	3.3	4.9	22.5	5
W1LBS3	1.7	8.02	1.8	2.1	24.4	5

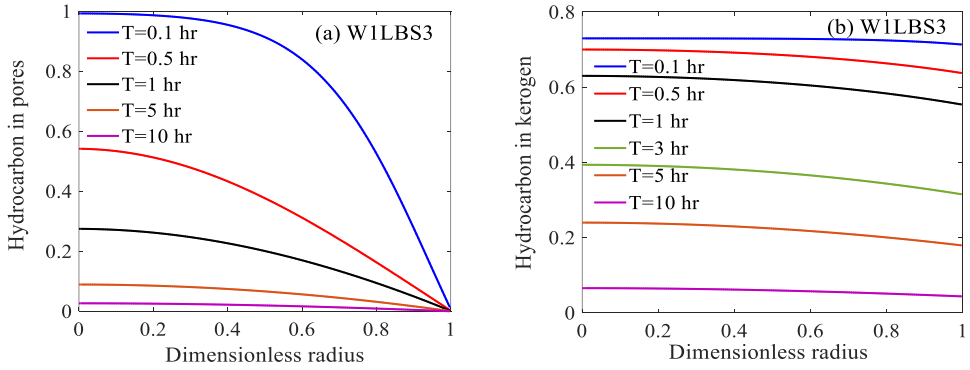

Figure 5-11 Hydrocarbon dimensionless concentration in pores and kerogen of crushed samples.

Figure 5-12 displays the recovery of hydrocarbons in shale samples with a cylindrical shape. The PKDL model was matched with the experimental data. The relative errors of the model are shown in Figure 5-13. The relative errors vary from -4% to 6.8%, which is very small. Those results show that the PKDL model can accurately simulate the hydrocarbon mass transfer between pores and kerogen matrix. The parameters used for history matching are shown in Table 5-7. The effective diffusion coefficients range from $0.61\text{-}2.4\times10^{-7}$ m^2/s. The extraction rates vary from $1.7\text{-}4.9\times10^{-5}$ s^{-1}. The extraction rate coefficients are potentially impacted by rock properties, such as specific surface area, porosity, and TOC, as shown in Eq. (5.11). The hydrocarbon recovery factors of samples vary from 22%-46% for seven hours. The recovery rates of plugs are much slower than spherical samples (Figure 5-10) due to their smaller specific surface areas. The crushed shale samples typically have a higher contact area with CO_2 which leads to higher recovery rates. Recovery factors of shale samples show significant discrepancies. The major reasons for the differences are effective diffusion coefficients and extraction rate coefficients. The higher the diffusion coefficients and extraction coefficients, the higher the recovery rate. Sample W2LBS1 has a lowest recovery of 20% for seven hours because of its low diffusion coefficient, as shown in Table 5-7.

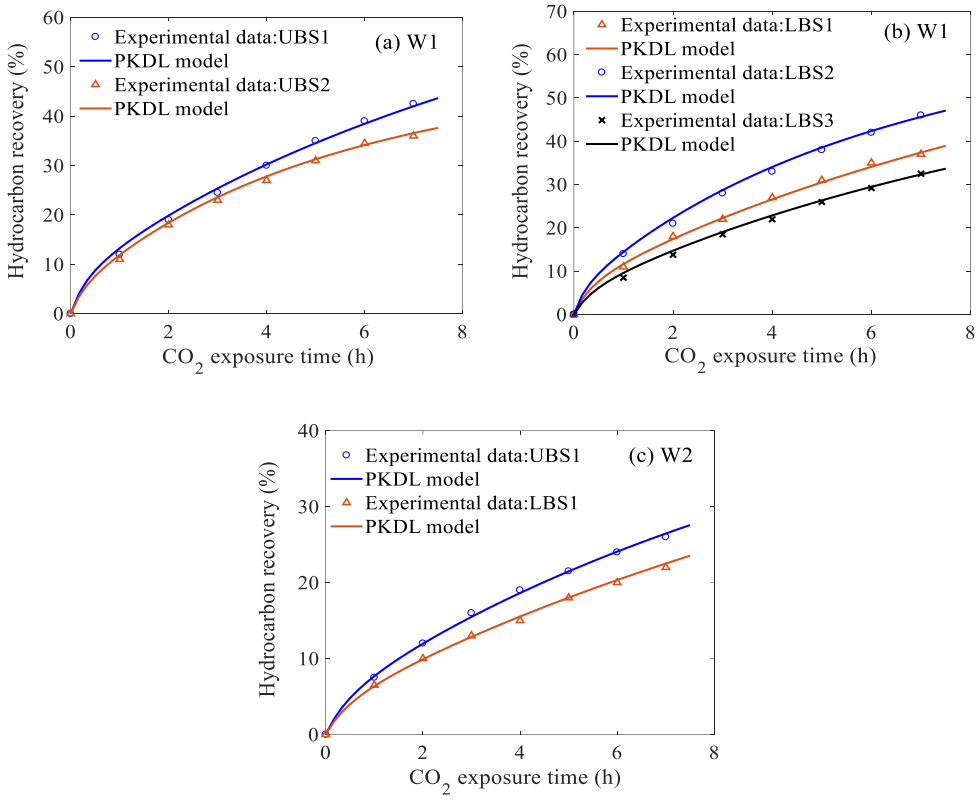

Figure 5-12 Modelling and experiments of hydrocarbon recovery for shale cores from wells W1 and W2.

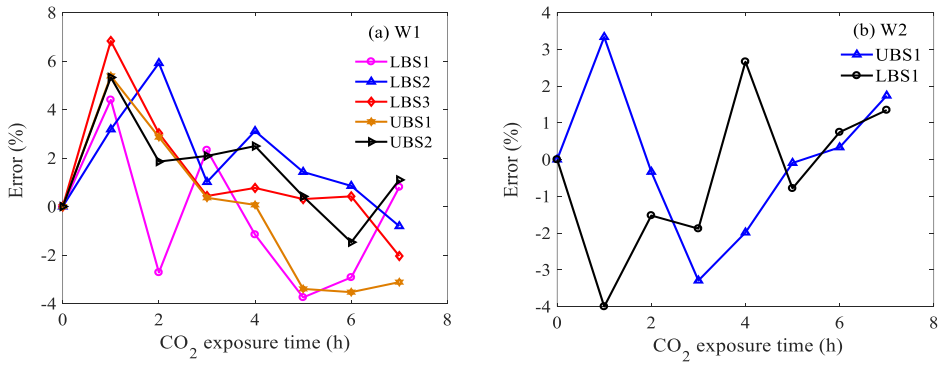

Figure 5-13 Relative error (in %) between the PKDL model and experiments for shale samples from wells W1 and W2.

Table 5-7 Parameters used for the simulation of CO_2 injection in Bakken shale plugs

Samples	Porosity (%)	D_{ev} (10^{-7} m^2/s)	D_{er} (10^{-7} m^2/s)	J (10^{-5} s^{-1})	F (%)	K_D
W1UBS1	9.97	2.35	2.10	1.8	23.96	5
W1UBS2	10.29	1.60	1.20	4.9	22.50	5
W1LBS1	8.89	2.20	1.80	1.7	26.55	5
W1LBS2	8.53	2.70	2.40	4.2	26.25	5
W1LBS3	8.02	1.25	1.18	2.1	24.40	5
W2UBS1	8.80	0.90	0.70	2.0	23.50	5
W2LBS1	8.40	0.91	0.61	1.7	30.29	5

The hydrocarbon recovery in pores and kerogen for sample W1LBS1 is shown in Figure 5-14. The results indicate that the hydrocarbons in pores are recovered prior to the hydrocarbons in kerogen at the early stage, before two hours. The hydrocarbon recovery rate at the early stage is mainly dominated by the diffusion in pores. However, the oil recovery of kerogen exceeds the oil recovery of pores at approximately 10 hours. This is because pores in shale rocks have a diffusion flux from kerogen, as shown in Figure 5-4. The pores serve as the flow paths for the hydrocarbon recovered from kerogen. The hydrocarbon recovery rate at the late stage is not only impacted by extraction coefficients but also by diffusion coefficients. The PKDL model is matched with experimental data by adjusting diffusion coefficients at the early stage and adjusting extraction coefficients at the late stage. The extraction rate coefficients for W1UBS2 and W1LBS3 in cylindrical shapes are the same as with spherical shapes, as shown in Table 5-6 and Table 5-7. This also indicates that the PKDL model is accurate in capturing the mass transfer between pores (inorganic and organic pores) and kerogen matrix. Figure 5-15 displays the visualization of hydrocarbon concentration in pores and kerogen for plug sample W1LBS. It is also observed that oil concentration in pores reduced faster than that in kerogen at the early stage. The hydrocarbon concentration is still high at 50 hours due to the mass flux from kerogen. However, the hydrocarbon

concentration in kerogen at the late stage is much lower than that at the early stage. This is because the diffusion flux out of the bulk kerogen is a source term for pores, as shown in the governing equations for pores and bulk kerogen.

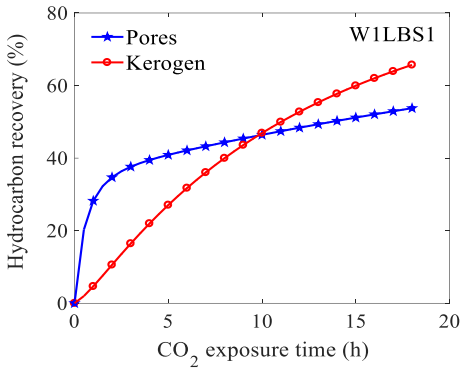

Figure 5-14 Hydrocarbon recovery in pores and kerogen for shale sample W1LBS1.

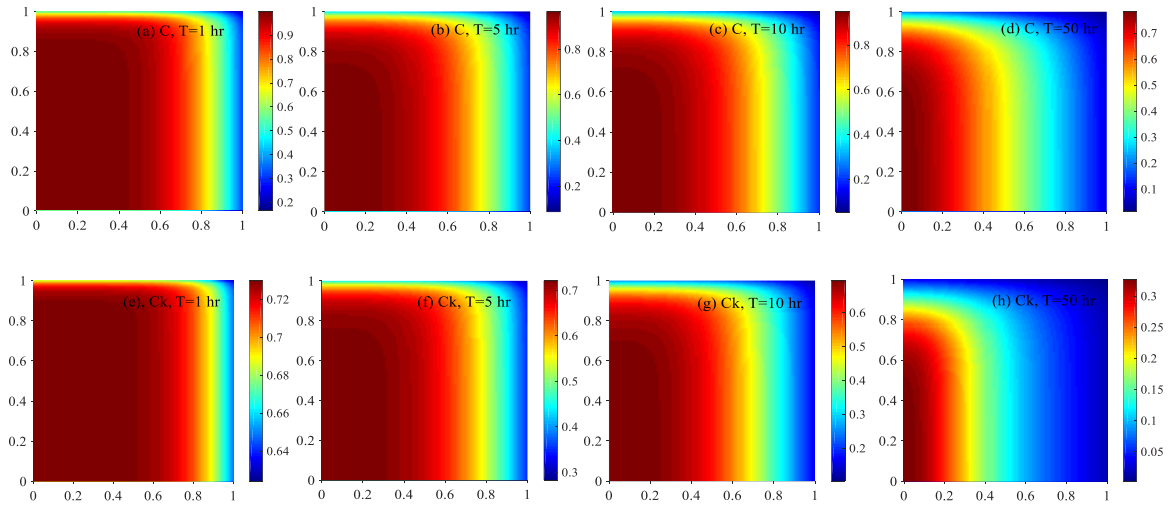

Figure 5-15 Visualization of hydrocarbon dimensionless concentration in pores (a-d) and kerogen (e-h) for shale W1LBS1. The X-axis is the dimensionless radius, the Y-axis is dimensionless half-length, and the original point is the center of the core.

3.3. Effects of Molecular Weight on Diffusion and Extraction

Figure 5-16 shows the hydrocarbon composition of crude oil produced from Lower Bakken

shale. The Bakken crude oil is very light, and sometimes C_{36}+ cannot be detected. The hydrocarbons that are lighter than C_6 probably vaporized during production and transportation. The major hydrocarbons in LBS are C_7-C_{25} and composed approximately 94% of the total hydrocarbons. The shale sample used for the CO_2 injection experiment was supplied by the operating company and had been wrapped with foil and refrigerated instantly upon collection. Recovery factors of hydrocarbons (C_{17}~C_{25}) were simulated using the PKDL model and were matched with experimental data from the literature (Hawthorne et al., 2019a).

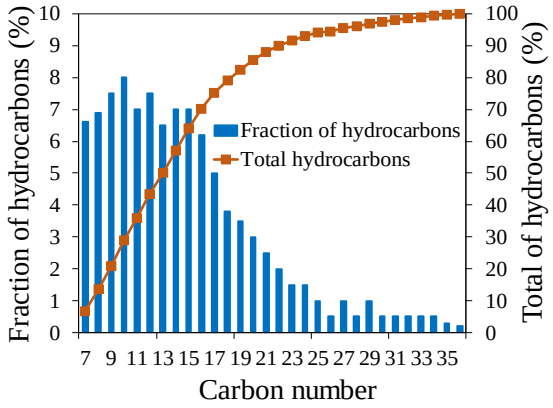

Figure 5-16 Compositions of crude oil produced from the Lower Bakken shale.

Figure 5-17 presents the recovery factors of hydrocarbons from C_7 to C_{25} for sample W3LBS. It is observed that the PKDL model accurately mimics the recovery of hydrocarbons with different molecular weights. The recovery of C_7-C_{25} shows significant differences and varies from 4%-36% for seven hours. The results also indicate that recovery rates decrease sharply with the carbon numbers. The CO_2 efficiently recovered the lighter hydrocarbons from the shale rocks. This is because the diffusion coefficients of hydrocarbons are significantly impacted by shape and size of molecules (Leahy-Dios and Firoozabadi, 2007). Since the hydrocarbons were recovered from the same sample, the effects of pore structure and organic matter were not considered. The diffusion coefficients mainly dominate the hydrocarbon recovery.

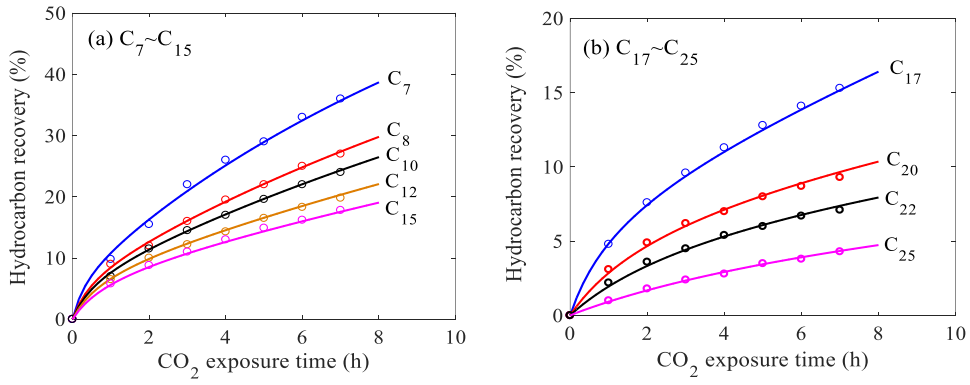

Figure 5-17 Recovery of hydrocarbons with different molecular weight (C_7~C_{25}) for sample W3LBS from well W3. The dots represent the experimental data and lines represent the PKDL model.

Figure 5-18 shows the relationships between extraction rate coefficients, diffusion coefficients, and carbon numbers. Results suggest that the effective diffusion coefficients decrease exponentially with carbon numbers, and the correlation coefficient is high. Results from the literature also indicated that the diffusion is a mass controlled process, and diffusion coefficients decrease exponentially with molecular weight (Tanahatoe and Kuil, 1997; Zeebe, 2011). It is reasonable to conclude that the higher the carbon numbers, the lower the diffusion coefficients. In addition, results show that extraction coefficients also drop exponentially with the carbon numbers, and have a high correlation coefficient. For a specific shale sample, the extraction coefficient is only impacted by the hydrocarbon diffusion coefficients in kerogen, as shown in Eq. (5.11). The extraction rate coefficients decrease exponentially because diffusion coefficients decrease exponentially with carbon numbers. The light hydrocarbons are recovered prior to the heavy hydrocarbons for the CO_2 injection process.

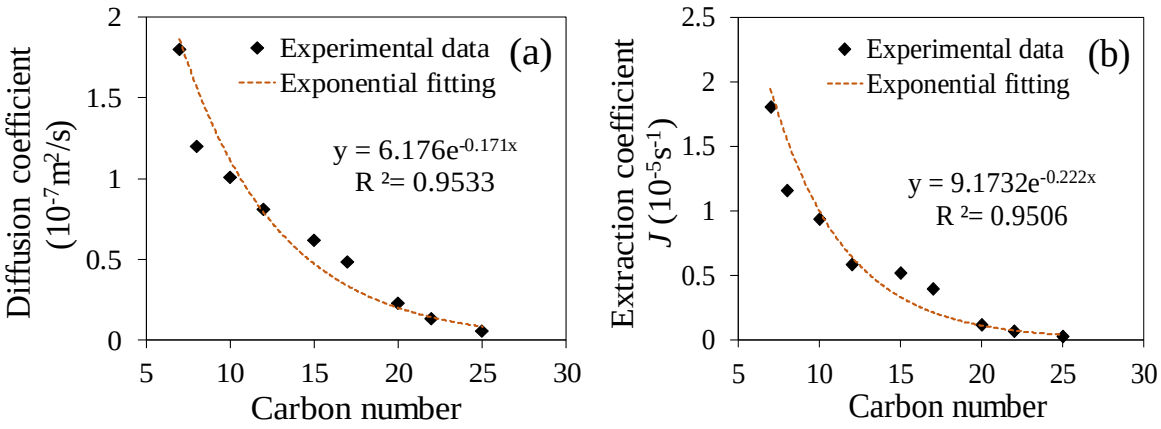

Figure 5-18 Relationships between diffusion coefficients (D_{er}) and carbon number (a); extraction rate coefficients (J) and carbon number (b).

4. Summary and Conclusions

In this work, a novel pore-kerogen diffuse layer model was proposed to capture the mass transfer between pores and organic matter in shale rocks. Mathematical models for hydrocarbon diffusion and extracting hydrocarbons from kerogen were matched with CO_2 injection experiments. This pore-kerogen diffuse layer model is capable of accurately predicting the hydrocarbon mass transfer between pores and kerogen matrix for supercritical CO_2 injection in shales. In addition, hydrocarbon recovery from shale rocks shows a delayed effect compared with tight rocks due to the additional mechanism of extracting hydrocarbons from kerogen by supercritical CO_2. For shale rocks, hydrocarbon effective diffusion coefficients vary from 0.61-3.3×10^{-7} m^2/s, and extraction rate coefficients vary from 1.7-4.9×10^{-5} s^{-1}. The effective diffusion coefficients of C_7-C_{25} in shale rocks vary from 0.06-1.8×10-7 m^2/s and decrease exponentially with carbon numbers. The extraction rate coefficients of C_7-C_{25} vary from 0.03-1.8×10^{-5} s^{-1} and decrease exponentially with carbon numbers because the diffusion coefficients of hydrocarbons in kerogen also decrease exponentially with carbon numbers.

We combined novel mathematical models with CO_2 injection experiments and advanced

mass transfer theories for CO_2 injection in shale reservoirs. This work should have wide application for future research of CO_2 enhanced oil recovery and geological sequestration in shale reservoirs.

CHAPTER VI:

CONCLUSIONS AND RECOMMANDATIONS

The goal of this Ph.D. work was to experimentally and numerically study the enhanced oil recovery mechanisms of surfactant and supercritical CO_2. To achieve this, we systematically investigated the permeability, porosity, pore structure, mineral composition, and TOC of various tight and shale samples by combining scanning electron microscope (SEM), X-ray diffraction (XRD), N_2 adsorption, and Rock-Eval analysis. The spontaneous imbibition experiments using water and surfactant were performed on various tight rocks. In addition, the water and oil vacuum imbibition experiments were conducted using shale samples to study the storage mechanisms of hydrocarbon in shale rocks. Furthermore, we numerically investigated the mass transfer mechanisms of hydrocarbon in shale for miscible CO_2 enhanced oil recovery. A new diffuse layer model was developed for hydrocarbon mass transfer in organic matter.

The spontaneous imbibition experiments and NMR measurements were combined to study the water-air two-phase flow in the Middle Bakken rocks. The water imbibition experiments were matched with mathematical models. The capillary pressure and relative permeability were obtained from the matching. Those models and experiments provide new methods to measure the capillary pressure and the relative permeability curves of tight rocks. Besides, surfactant imbibition experiments were carried out on Middle Bakken rock samples. Before the experiments, the core samples were saturated with Bakken crude oil. The oil recovery by anionic, cationic, and nonionic surfactant solutions was evaluated at high-temperature conditions. The effects of minerals, surfactant types, and pore size distribution on oil recovery were investigated. The surfactants can significantly improve the oil recovery of the Middle Bakken samples. The anionic surfactant yield higher oil recovery factors than those of nonionic and cationic surfactants.

In addition, the vacuum imbibition was conducted on various crushed shale samples using water and n-dodecane. Water can flow in the inorganic pores at the presence of capillary until it fully saturates the inorganic pores, while n-dodecane is able to flow in the inorganic pores and organic pores, and diffuse in organic matter. Water is not able to enter the organic matter due to the strong hydrophobic surface of organic matter. The oil stored in the organic matter can be obtained from the volume differences between n-dodecane and water. The effects of TOC and kerogen maturity on the storage capacity of organic matter were investigated. The total oil in kerogen decreases with thermal maturity. The oil volume in organic pores increases with thermal maturity. The dissolved oil volume in kerogen decreases with thermal maturity. The mathematical models for vacuum imbibition were proposed. The models were matched with the imbibition experiments by adjusting capillary pressure and dissolution rate coefficients. The diffusion in kerogen is a very slow process, and the dissolution rate constants vary from 8.09×10^{-9} to 2.58×10^{-10} s^{-1}.

A pore-kerogen diffuse layer model was proposed for the mass transfer between organic matter and pores for miscible CO_2 EOR in shale. The mathematical models for hydrocarbon recovery in crushed samples and core plugs were derived. The mathematical models are consistent with hydrocarbon recovery data obtained from the literature. The models were matched with experiments by adjusting diffusion coefficients and extraction rate coefficients. Results suggested that the TOC and hydrocarbon molecular weight have significant impacts on oil recovery. The organic matter slows down the oil recovery in shale rocks due to the low diffusion coefficients of hydrocarbon in organic matter. The higher the molecular weight, the lower the recovery. The diffusion coefficients of hydrocarbon in shale and the extraction rate coefficients decrease with carbon numbers.

However, the transport mechanisms in unconventional reservoirs are much complex than experiments in rock samples. The flow in fractures is not involved in this dissertation. It is of great importance to integrate imbibition mechanisms and the PKDL model into the numerical simulation of fractured reservoirs. The surfactant enhanced oil recovery is also a complex transport process, which probably includes flow, diffusion, and adsorption. The transport mechanisms of surfactants in rocks need further experimental and numerical studies. The transport mechanisms of CO_2 and hydrocarbon critical for EOR and carbon storage in shale reservoirs.

REFERENCES

Agrawal, V., Sharma, S., 2018. Improved Kerogen Models for Determining Thermal Maturity and Hydrocarbon Potential of Shale. Sci. Rep. 8, 1–8.

Alfarge, D., Wei, M., Bai, B., 2017. IOR Methods in Unconventional Reservoirs of North America: Comprehensive Review. Presented at the SPE Western Regional Meeting, Society of Petroleum Engineers.

Alhammadi, A.M., AlRatrout, A., Singh, K., Bijeljic, B., Blunt, M.J., 2017. In situ characterization of mixed-wettability in a reservoir rock at subsurface conditions. Sci. Rep. 7, 10753.

Alharthy, N., Teklu, T.W., Kazemi, H., Graves, R.M., Hawthorne, S.B., Braunberger, J., Kurtoglu, B., 2018. Enhanced Oil Recovery in Liquid-Rich Shale Reservoirs: Laboratory to Field. SPE Reserv. Eval. Eng. 21,

Aljamaan, H., Holmes, R., Vishal, V., Haghpanah, R., Wilcox, J., Kovscek, A.R., 2017. CO_2 Storage and Flow Capacity Measurements on Idealized Shales from Dynamic Breakthrough Experiments. Energy Fuels 31, 1193–1207.

Alvarez, J.O., Saputra, I.W.R., Schechter, D.S., 2017. Potential of Improving Oil Recovery with Surfactant Additives to Completion Fluids for the Bakken. Energy Fuels 31, 5982–5994.

Alvarez, J.O., Schechter, D.S., 2017. Wettability Alteration and Spontaneous Imbibition in Unconventional Liquid Reservoirs by Surfactant Additives. SPE Reserv. Eval. Eng. 20, 107–117.

Alyafei, N., Al-Menhali, A., Blunt, M.J., 2016. Experimental and Analytical Investigation of Spontaneous Imbibition in Water-Wet Carbonates. Transp. Porous Media 115, 189–207.

Alyafei, N., Blunt, M.J., 2018. Estimation of relative permeability and capillary pressure from mass imbibition experiments. Adv. Water Resour. 115, 88–94.

Arif, M., Lebedev, M., Barifcani, A., Iglauer, S., 2017. Influence of shale-total organic content on CO_2 geo-storage potential. Geophys. Res. Lett. 44, 8769–8775.

Atchariyawut, S., Jiraratananon, R., Wang, R., 2008. Mass transfer study and modeling of gas–liquid membrane contacting process by multistage cascade model for CO_2 absorption. Sep. Purif. Technol. 63, 15–22.

Begum, M., Yassin, M.R., Dehghanpour, H., 2019. Effect of kerogen maturity on organic shale wettability: A Duvernay case study. Mar. Pet. Geol. 110, 483–496.

Belhaj, A.F., Elraies, K.A., Mahmood, S.M., Zulkifli, N.N., Akbari, S., Hussien, O.S., 2020. The effect of surfactant concentration, salinity, temperature, and pH on surfactant adsorption for chemical enhanced oil recovery: a review. J. Pet. Explor. Prod. Technol. 10, 125–137.

Berthonneau, J., Obliger, A., Valdenaire, P.-L., Grauby, O., Ferry, D., Chaudanson, D., Levitz, P., Kim, J.J., Ulm, F.-J., Pellenq, R.J.-M., 2018. Mesoscale structure, mechanics, and transport properties of source rocks' organic pore networks. Proc. Natl. Acad. Sci. 115, 12365–12370.

Birdsell, D.T., Rajaram, H., Lackey, G., 2015. Imbibition of hydraulic fracturing fluids into partially saturated shale. Water Resour. Res. 51, 6787–6796.

Bousige, C., Ghimbeu, C.M., Vix-Guterl, C., Pomerantz, A.E., Suleimenova, A., Vaughan, G., Garbarino, G., Feygenson, M., Wildgruber, C., Ulm, F.-J., Pellenq, R.J.-M., Coasne, B.,

2016. Realistic molecular model of kerogen's nanostructure. Nat. Mater. 15, 576–582. https://doi.org/10.1038/nmat4541
Bush, I., 2019. NMR Studies of Enhanced Oil Recovery Core Floods and Core Analysis Protocols (Thesis). University of Cambridge. https://doi.org/10.17863/CAM.37374
Cadogan, S.P., Mistry, B., Wong, Y., Maitland, G.C., Trusler, J.P.M., 2016. Diffusion Coefficients of Carbon Dioxide in Eight Hydrocarbon Liquids at Temperatures between (298.15 and 423.15) K at Pressures up to 69 MPa. J. Chem. Eng. Data 61, 3922–3932.
Cardoso, O.R., Balaban, R. de C., 2015. Comparative study between Botucatu and Berea sandstone properties. J. South Am. Earth Sci. 62, 58–69.
Caudwell, D.R., Trusler, J.P.M., Vesovic, V., Wakeham, W.A., 2004. The Viscosity and Density of n-Dodecane and n-Octadecane at Pressures up to 200 MPa and Temperatures up to 473 K. Int. J. Thermophys. 25, 1339–1352.
Charoensuppanimit, P., Mohammad, S.A., Gasem, K.A.M., 2016. Measurements and Modeling of Gas Adsorption on Shales. Energy Fuels 30, 2309–2319.
Chatzis, I., Dullien, F.A.L., 1983. Dynamic immiscible displacement mechanisms in pore doublets: Theory versus experiment. J. Colloid Interface Sci. 91, 199–222.
Chen, L., Wang, Y., Wan, Y., Cai, Y., Xiong, Y., Fan, Z., Conradson, S.D., Fu, H., Yuan, L., Feng, W., 2020. Highly efficient and selective pillararene-based organic materials for Hg^{2+} and CH_3Hg^+ extraction from aqueous solution. Chem. Eng. J. 387, 124087.
Chen, Q., Gingras, M.K., Balcom, B.J., 2003. A magnetic resonance study of pore filling processes during spontaneous imbibition in Berea sandstone. J. Chem. Phys. 119, 9609–9616.
Chen, T., Yang, Z., Luo, Y., Lin, W., Xu, J., Ding, Y., Niu, J., 2018. Evaluation of Displacement Effects of Different Injection Media in Tight Oil Sandstone by Online Nuclear Magnetic Resonance. Energies 11, 2836.
Cheng, Z., Wang, Q., Ning, Z., Li, M., Lyu, C., Huang, L., Wu, X., 2018. Experimental Investigation of Countercurrent Spontaneous Imbibition in Tight Sandstone Using Nuclear Magnetic Resonance. Energy Fuels 32, 6507–6517.
Cheraghian, G., 2015. Effects of nanoparticles on wettability: A review on applications of nanotechnology in the enhanced Oil recovery. Int. J. Nano Dimens. 6, 443–452.
Cho, Y., Eker, E., Uzun, I., Yin, X., Kazemi, H., 2016. Rock Characterization in Unconventional Reservoirs: A Comparative Study of Bakken, Eagle Ford, and Niobrara Formations. Presented at the SPE Low Perm Symposium, Society of Petroleum Engineers.
Christensen, M., Tanino, Y., 2017. Waterflood Oil Recovery from Mixed-Wet Limestone: Dependence upon the Contact Angle. Energy Fuels 31, 1529–1535.
Craddock, P.R., Bake, K.D., Pomerantz, A.E., 2018. Chemical, Molecular, and Microstructural Evolution of Kerogen during Thermal Maturation: Case Study from the Woodford Shale of Oklahoma. Energy Fuels 32, 4859–4872.
Cui, R., Feng, Q., Chen, H., Zhang, W., Wang, S., 2019. Multiscale random pore network modeling of oil-water two-phase slip flow in shale matrix. J. Pet. Sci. Eng. 175, 46–59.
Cummins, B.M., Chinthapatla, R., Ligler, F.S., Walker, G.M., 2017. Time-Dependent Model for Fluid Flow in Porous Materials with Multiple Pore Sizes. Anal. Chem. 89, 4377–4381.
De Marco, I., Riemma, S., Iannone, R., 2018. Life cycle assessment of supercritical CO_2 extraction of caffeine from coffee beans. J. Supercrit. Fluids 133, 393–400.

Dehghanpour, H., Lan, Q., Saeed, Y., Fei, H., Qi, Z., 2013. Spontaneous Imbibition of Brine and Oil in Gas Shales: Effect of Water Adsorption and Resulting Microfractures. Energy Fuels 27, 3039–3049.
Dong, M., Dullien, F.A.L., Dai, L., Li, D., 2005. Immiscible Displacement in the Interacting Capillary Bundle Model Part I. Development of Interacting Capillary Bundle Model. Transp. Porous Media 59, 1–18.
Dunn, K.-J., Bergman, D.J., LaTorraca, G.A., 2002. Nuclear Magnetic Resonance: Petrophysical and Logging Applications. Elsevier.
Elwinger, F., Pourmand, P., Furó, I., 2017. Diffusive Transport in Pores. Tortuosity and Molecular Interaction with the Pore Wall. J. Phys. Chem. C 121, 13757–13764.
Emera, M.K., Sarma, H.K., 2007. Prediction of CO_2 Solubility in Oil and the Effects on the Oil Physical Properties. Energy Sources Part Recovery Util. Environ. Eff. 29, 1233–1242.
Ertas, D., Kelemen, S.R., Halsey, T.C., 2006. Petroleum Expulsion Part 1. Theory of Kerogen Swelling in Multicomponent Solvents. Energy Fuels 20, 295–300.
Esmaeilzadeh, P., Bahramian, A., Fakhroueian, Z., 2011. Adsorption of Anionic, Cationic and Nonionic Surfactants on Carbonate Rock in Presence of ZrO2 Nanoparticles. Phys. Procedia, 2011 International Conference on Physics Science and Technology (ICPST 2011) 22, 63–67.
Etminan, S.R., Javadpour, F., Maini, B.B., Chen, Z., 2014. Measurement of gas storage processes in shale and of the molecular diffusion coefficient in kerogen. Int. J. Coal Geol., Special issue: Adsorption and fluid transport phenomena in gas shales and their effects on production and storage 123, 10–19.
Fakher, S., Imqam, A., 2020. Application of carbon dioxide injection in shale oil reservoirs for increasing oil recovery and carbon dioxide storage. Fuel 265, 116944.
Falk, K., Coasne, B., Pellenq, R., Ulm, F.-J., Bocquet, L., 2015. Subcontinuum mass transport of condensed hydrocarbons in nanoporous media. Nat. Commun. 6, 6949.
Fernø, M.A., Hauge, L.P., Rognmo, A.U., Gauteplass, J., Graue, A., 2015. Flow visualization of CO_2 in tight shale formations at reservoir conditions. Geophys. Res. Lett. 42, 7414–7419.
Fishman, N.S., Hackley, P.C., Lowers, H.A., Hill, R.J., Egenhoff, S.O., Eberl, D.D., Blum, A.E., 2012. The nature of porosity in organic-rich mudstones of the Upper Jurassic Kimmeridge Clay Formation, North Sea, offshore United Kingdom. Int. J. Coal Geol., Shale Gas and Shale Oil Petrology and Petrophysics 103, 32–50.
Foley, A.Y., Nooruddin, H.A., Blunt, M.J., 2017. The impact of capillary backpressure on spontaneous counter-current imbibition in porous media. Adv. Water Resour. 107, 405–420.
Gao, H., Li, H., 2015. Determination of movable fluid percentage and movable fluid porosity in ultra-low permeability sandstone using nuclear magnetic resonance (NMR) technique. J. Pet. Sci. Eng. 133, 258–267.
Gbadamosi, A.O., Junin, R., Manan, M.A., Agi, A., Yusuff, A.S., 2019. An overview of chemical enhanced oil recovery: recent advances and prospects. Int. Nano Lett. 9, 171–202.
Gherabati, S.A., Hamlin, H.S., Smye, K.M., Eastwood, R.L., Male, F.R., McDaid, G., 2019. Evaluating hydrocarbon-in-place and recovery factor in a hybrid petroleum system: Case of Bakken and three forks in North Dakota. Interpretation 7, T607–T624.
Godefroy, S., Fleury, M., Deflandre, F., Korb, J.-P., 2002. Temperature Effect on NMR Surface Relaxation in Rocks for Well Logging Applications. J. Phys. Chem. B 106, 11183–11190. https://doi.org/10.1021/jp0213452

Gong, H., Qin, X., Shang, S., Zhu, C., Xu, L., San, Q., Li, Y., Dong, M., 2020. Enhanced Shale Oil Recovery by the Huff and Puff Method Using CO_2 and Cosolvent Mixed Fluids. Energy Fuels 34, 1438–1446.

Graue, A., Fernø, M.A., 2011. Water mixing during spontaneous imbibition at different boundary and wettability conditions. J. Pet. Sci. Eng. 78, 586–595.

Guo, H., Dou, M., Hanqing, W., Wang, F., Yuanyuan, G., Yu, Z., Yansheng, W., Li, Y., 2017. Proper Use of Capillary Number in Chemical Flooding. J. Chem.

Hattori, Y., Haruna, Y., Otsuka, M., 2013. Dissolution process analysis using model-free Noyes-Whitney integral equation. Colloids Surf. B Biointerfaces 102, 227–231.

Haugen, Å., Fernø, M.A., Mason, G., Morrow, N.R., 2014. Capillary pressure and relative permeability estimated from a single spontaneous imbibition test. J. Pet. Sci. Eng. 115, 66–77.

Hawthorne, S.B., Gorecki, C.D., Sorensen, J.A., Steadman, E.N., Harju, J.A., Melzer, S., 2013. Hydrocarbon Mobilization Mechanisms from Upper, Middle, and Lower Bakken Reservoir Rocks Exposed to CO_2. Presented at the SPE Unconventional Resources Conference Canada, Society of Petroleum Engineers.

Hawthorne, S.B., Grabanski, C.B., Miller, D.J., Kurz, B.A., Sorensen, J.A., 2019a. Hydrocarbon Recovery from Williston Basin Shale and Mudrock Cores with Supercritical CO_2: 2. Mechanisms That Control Oil Recovery Rates and CO_2 Permeation. Energy Fuels 33, 6867–6877.

Hawthorne, S.B., Miller, D.J., Grabanski, C.B., Azzolina, N., Kurz, B.A., Ardakani, O.H., Smith, S.A., Sanei, H., Sorensen, J.A., 2019b. Hydrocarbon Recovery from Williston Basin Shale and Mudrock Cores with Supercritical CO_2: Part 1. Method Validation and Recoveries from Cores Collected across the Basin. Energy Fuels 33, 6857–6866.

Hawthorne, S.B., Miller, D.J., Jin, L., Gorecki, C.D., 2016. Rapid and Simple Capillary-Rise/Vanishing Interfacial Tension Method To Determine Crude Oil Minimum Miscibility Pressure: Pure and Mixed CO_2, Methane, and Ethane. Energy Fuels 30, 6365–6372.

Heller, R., Zoback, M., 2014. Adsorption of methane and carbon dioxide on gas shale and pure mineral samples. J. Unconv. Oil Gas Resour. 8, 14–24.

Hou, B., Wang, Y., Cao, X., Zhang, J., Song, X., Ding, M., Chen, W., 2016. Surfactant-Induced Wettability Alteration of Oil-Wet Sandstone Surface: Mechanisms and Its Effect on Oil Recovery. J. Surfactants Deterg. 19, 315–324.

Hou, B., Wang, Y., Huang, Y., 2015. Mechanistic study of wettability alteration of oil-wet sandstone surface using different surfactants. Appl. Surf. Sci. 330, 56–64.

Hu, W., Jiang, Y., Chen, D., Lin, Y., Han, Q., Cui, Y., 2018. Impact of Pore Geometry and Water Saturation on Gas Effective Diffusion Coefficient in Soil. Appl. Sci. 8, 2097. https://doi.org/10.3390/app8112097

Huang, J., Jin, T., Barrufet, M., Killough, J., 2020. Evaluation of CO_2 injection into shale gas reservoirs considering dispersed distribution of kerogen. Appl. Energy 260, 114285.

Hughes, J.D., 2013. Energy: A reality check on the shale revolution. Nature 494, 307–308.

Humez, P., Négrel, P., Lagneau, V., Lions, J., Kloppmann, W., Gal, F., Millot, R., Guerrot, C., Flehoc, C., Widory, D., Girard, J.-F., 2014. CO_2–water–mineral reactions during CO_2 leakage: Geochemical and isotopic monitoring of a CO_2 injection field test. Chem. Geol. 368, 11–30.

Huo, P., Zhang, D., Yang, Z., Li, W., Zhang, J., Jia, S., 2017. CO_2 geological sequestration: Displacement behavior of shale gas methane by carbon dioxide injection. Int. J. Greenh. Gas Control 66, 48–59.
Iglauer, S., Pentland, C.H., Busch, A., 2015. CO_2 wettability of seal and reservoir rocks and the implications for carbon geo-sequestration. Water Resour. Res. 51, 729–774.
Jarrahian, Kh., Seiedi, O., Sheykhan, M., Sefti, M.V., Ayatollahi, Sh., 2012. Wettability alteration of carbonate rocks by surfactants: A mechanistic study. Colloids Surf. Physicochem. Eng. Asp. 410, 1–10.
Jarvie, D.M., Hill, R.J., Ruble, T.E., Pollastro, R.M., 2007. Unconventional shale-gas systems: The Mississippian Barnett Shale of north-central Texas as one model for thermogenic shale-gas assessment. AAPG Bull. 91, 475–499.
Jatukaran, A., Zhong, J., Persad, A.H., Xu, Y., Mostowfi, F., Sinton, D., 2018. Direct Visualization of Evaporation in a Two-Dimensional Nanoporous Model for Unconventional Natural Gas. ACS Appl. Nano Mater. 1, 1332–1338.
Jeon, P.R., Choi, J., Yun, T.S., Lee, C.-H., 2014. Sorption equilibrium and kinetics of CO_2 on clay minerals from subcritical to supercritical conditions: CO_2 sequestration at nanoscale interfaces. Chem. Eng. J. 255, 705–715.
Jia, B., Tsau, J.-S., Barati, R., 2019. A review of the current progress of CO_2 injection EOR and carbon storage in shale oil reservoirs. Fuel 236, 404–427.
Jia, W., McPherson, B., Pan, F., Dai, Z., Moodie, N., Xiao, T., 2018. Impact of Three-Phase Relative Permeability and Hysteresis Models on Forecasts of Storage Associated With CO_2-EOR. Water Resour. Res. 54, 1109–1126.
Jiang, Y., Luo, Y., Lu, Y., Qin, C., Liu, H., 2016. Effects of supercritical CO_2 treatment time, pressure, and temperature on microstructure of shale. Energy 97, 173–181.
Jin, L., Hawthorne, S., Sorensen, J., Pekot, L., Kurz, B., Smith, S., Heebink, L., Herdegen, V., Bosshart, N., Torres, J., Dalkhaa, C., Peterson, K., Gorecki, C., Steadman, E., Harju, J., 2017. Advancing CO_2 enhanced oil recovery and storage in unconventional oil play—Experimental studies on Bakken shales. Appl. Energy 208, 171–183.
Jing, W., Huiqing, L., Genbao, Q., Yongcan, P., Yang, G., 2019. Investigations on spontaneous imbibition and the influencing factors in tight oil reservoirs. Fuel 236, 755–768.
Kathel, P., Mohanty, K.K., 2013. Wettability Alteration in a Tight Oil Reservoir. Energy Fuels 27, 6460–6468.
Kelemen, S.R., Afeworki, M., Gorbaty, M.L., Sansone, M., Kwiatek, P.J., Walters, C.C., Freund, H., Siskin, M., Bence, A.E., Curry, D.J., Solum, M., Pugmire, R.J., Vandenbroucke, M., Leblond, M., Behar, F., 2007. Direct Characterization of Kerogen by X-ray and Solid-State 13C Nuclear Magnetic Resonance Methods. Energy Fuels 21, 1548–1561.
Kibria, M.G., Hu, Q., Liu, H., Zhang, Y., Kang, J., 2018. Pore structure, wettability, and spontaneous imbibition of Woodford Shale, Permian Basin, West Texas. Mar. Pet. Geol. 91, 735–748.
Kuang, W., Lu, M., Yeboah, I., Qian, G., Duan, X., Yang, J., Chen, D., Zhou, X., 2019. A comprehensive kinetics study on non-isothermal pyrolysis of kerogen from Green River oil shale. Chem. Eng. J., ISCRE 25 Special Issue: Bridging Science and Technology 377, 120275.
Kumar, A., Mandal, A., 2017. Synthesis and physiochemical characterization of zwitterionic surfactant for application in enhanced oil recovery. J. Mol. Liq. 243, 61–71.

Kumar, S., Panigrahi, P., Saw, R.K., Mandal, A., 2016. Interfacial Interaction of Cationic Surfactants and Its Effect on Wettability Alteration of Oil-Wet Carbonate Rock. Energy Fuels 30, 2846–2857.

Lafortune, S., Adelise, F., Garrido, D.R.R., Pokryszka, Z., 2014. Assessing CO_2 Adsorption Capacities onto Shales Through Gravimetric Experiments: A First Step in the Feasibility Study of Coupling "Fracking" with Carbon Storage. Energy Procedia, 12th International Conference on Greenhouse Gas Control Technologies, GHGT-12 63, 5933–5937.

Lai, F., Li, Z., Zhang, T., Zhou, A., Gong, B., 2019. Characteristics of microscopic pore structure and its influence on spontaneous imbibition of tight gas reservoir in the Ordos Basin, China. J. Pet. Sci. Eng. 172, 23–31.

Lan, Q., Xu, M., Binazadeh, M., Dehghanpour, H., Wood, J.M., 2015. A comparative investigation of shale wettability: The significance of pore connectivity. J. Nat. Gas Sci. Eng. 27, 1174–1188.

Larsen, J.W., Li, S., 1994. Solvent Swelling Studies of Green River Kerogen. Energy Fuels 8, 932–936.

Leahy-Dios, A., Firoozabadi, A., 2007. Molecular and Thermal Diffusion Coefficients of Alkane−Alkane and Alkane−Aromatic Binary Mixtures: Effect of Shape and Size of Molecules. J. Phys. Chem. B 111, 191–198.

Lemmon, E.W., Jacobsen, R.T., 2004. Viscosity and Thermal Conductivity Equations for Nitrogen, Oxygen, Argon, and Air. Int. J. Thermophys. 25, 21–69.

Leybros, A., Hung, L., Hertz, A., Hartmann, D., Grandjean, A., Boutin, O., 2017. Supercritical CO_2 extraction of uranium from natural ore using organophosphorus extractants. Chem. Eng. J. 316, 196–203.

Li, L., Wang, C., Li, D., Fu, J., Su, Y., Lv, Y., 2019. Experimental investigation of shale oil recovery from Qianjiang core samples by the CO_2 huff-n-puff EOR method. RSC Adv. 9, 28857–28869.

Li, L., Zhang, Y., Sheng, J.J., 2017. Effect of the Injection Pressure on Enhancing Oil Recovery in Shale Cores during the CO_2 Huff-n-Puff Process When It Is above and below the Minimum Miscibility Pressure. Energy Fuels 31, 3856–3867.

Li, M., Chen, Z., Ma, X., Cao, T., Li, Z., Jiang, Q., 2018. A numerical method for calculating total oil yield using a single routine Rock-Eval program: A case study of the Eocene Shahejie Formation in Dongying Depression, Bohai Bay Basin, China. Int. J. Coal Geol. 191, 49–65.

Li, M., Chen, Z., Ma, X., Cao, T., Qian, M., Jiang, Q., Tao, G., Li, Z., Song, G., 2019. Shale oil resource potential and oil mobility characteristics of the Eocene-Oligocene Shahejie Formation, Jiyang Super-Depression, Bohai Bay Basin of China. Int. J. Coal Geol. 204, 130–143.

Li, S., Li, Z., Dong, Q., 2016. Diffusion coefficients of supercritical CO_2 in oil-saturated cores under low permeability reservoir conditions. J. CO_2 Util. 14, 47–60.

Li, Y., Ruth, D., Mason, G., Morrow, N.R., 2006. Pressures acting in counter-current spontaneous imbibition. J. Pet. Sci. Eng., Reservoir Wettability 52, 87–99.

Li, Z., Dong, M., 2009. Experimental Study of Carbon Dioxide Diffusion in Oil-Saturated Porous Media under Reservoir Conditions. Ind. Eng. Chem. Res. 48, 9307–9317.

Liang, B., Jiang, H., Li, J., Gong, C., Jiang, R., Qu, S., Pei, Y., Yang, H., 2017. Investigation of Oil Saturation Development behind Spontaneous Imbibition Front Using Nuclear Magnetic Resonance T2. Energy Fuels 31, 473–481.

Liu, B., Qi, C., Zhao, X., Teng, G., Zhao, L., Zheng, H., Zhan, K., Shi, J., 2018. Nanoscale Two-Phase Flow of Methane and Water in Shale Inorganic Matrix. J. Phys. Chem. C 122, 26671–26679.
Liu, Junrong, Sheng, J.J., Wang, X., Ge, H., Yao, E., 2019. Experimental study of wettability alteration and spontaneous imbibition in Chinese shale oil reservoirs using anionic and nonionic surfactants. J. Pet. Sci. Eng. 175, 624–633.
Liu, Jun, Xie, L., Elsworth, D., Gan, Q., 2019. CO_2/CH_4 Competitive Adsorption in Shale: Implications for Enhancement in Gas Production and Reduction in Carbon Emissions. Environ. Sci. Technol. 53, 9328–9336.
Liu, K., Ostadhassan, M., Zhou, J., Gentzis, T., Rezaee, R., 2017. Nanoscale pore structure characterization of the Bakken shale in the USA. Fuel 209, 567–578. https://doi.org/10.1016/j.fuel.2017.08.034
Liu, K., Ostadhassan, M., Zou, J., Gentzis, T., Rezaee, R., Bubach, B., Carvajal-Ortiz, H., 2018. Multifractal analysis of gas adsorption isotherms for pore structure characterization of the Bakken Shale. Fuel 219, 296–311.
Liu, Yueliang, Ma, X., Li, H.A., Hou, J., 2019. Competitive adsorption behavior of hydrocarbon(s)/CO_2 mixtures in a double-nanopore system using molecular simulations. Fuel 252, 612–621.
Liu, Y., Yao, Y., Liu, D., Zheng, S., Sun, G., Chang, Y., 2018. Shale pore size classification: An NMR fluid typing method. Mar. Pet. Geol. 96, 591–601.
Löhr, S.C., Baruch, E.T., Hall, P.A., Kennedy, M.J., 2015. Is organic pore development in gas shales influenced by the primary porosity and structure of thermally immature organic matter? Org. Geochem. 87, 119–132.
Longbottom, T.L., Hockaday, W.C., Boling, K.S., Li, G., Letourmy, Y., Dong, H., Dworkin, S.I., 2016. Organic structural properties of kerogen as predictors of source rock type and hydrocarbon potential. Fuel 184, 792–798.
Loucks, R.G., Reed, R.M., Ruppel, S.C., Hammes, U., 2012. Spectrum of pore types and networks in mudrocks and a descriptive classification for matrix-related mudrock pores. AAPG Bull. 96, 1071–1098.
Lu, J., 2014. Development of novel surfactants and surfactant methods for chemical enhanced oil recovery (Thesis).
Luhmann, A.J., Tutolo, B.M., Bagley, B.C., Mildner, D.F.R., Seyfried, W.E., Saar, M.O., 2017. Permeability, porosity, and mineral surface area changes in basalt cores induced by reactive transport of CO_2-rich brine. Water Resour. Res. 53, 1908–1927.
Lyu, C., Ning, Z., Chen, M., Wang, Q., 2019. Experimental study of boundary condition effects on spontaneous imbibition in tight sandstones. Fuel 235, 374–383.
Lyu, C., Ning, Z., Wang, Q., Chen, M., 2018. Application of NMR T2 to Pore Size Distribution and Movable Fluid Distribution in Tight Sandstones. Energy Fuels 32, 1395–1405.
Mason, G., Morrow, N.R., 2013. Developments in spontaneous imbibition and possibilities for future work. J. Pet. Sci. Eng. 110, 268–293.
Mattax, C.C., Kyte, J.R., 1962. Imbibition Oil Recovery from Fractured, Water-Drive Reservoir. Soc. Pet. Eng. J. 2, 177–184.
Mavroudi, M., Kaldis, S.P., Sakellaropoulos, G.P., 2006. A study of mass transfer resistance in membrane gas–liquid contacting processes. J. Membr. Sci. 272, 103–115.

Mendes, M.F., Pessoa, F.L.P., Uller, A.M.C., 2002. An economic evaluation based on an experimental study of the vitamin E concentration present in deodorizer distillate of soybean oil using supercritical CO_2. J. Supercrit. Fluids 23, 257–265.
Meng, Z., Yang, S.-L., Cui, Y., Zhong, Z.-Y., Liang, C.-G., Wang, L., Qian, K., Ma, Q.-Z., Wang, J.-R., 2018. Enhancement of the imbibition recovery by surfactants in tight oil reservoirs. Pet. Sci. 15, 783–793.
Middleton, R.S., Gupta, R., Hyman, J.D., Viswanathan, H.S., 2017. The shale gas revolution: Barriers, sustainability, and emerging opportunities. Appl. Energy 199, 88–95.
Minagawa, H., Nishikawa, Y., Ikeda, I., Miyazaki, K., Takahara, N., Sakamoto, Y., Komai, T., Narita, H., 2008. Characterization of sand sediment by pore size distribution and permeability using proton nuclear magnetic resonance measurement. J. Geophys. Res. Solid Earth 113.
Mirchi, V., Saraji, S., Goual, L., Piri, M., 2015. Dynamic interfacial tension and wettability of shale in the presence of surfactants at reservoir conditions. Fuel 148, 127–138.
Mirzaei-Paiaman, A., 2015. Analysis of counter-current spontaneous imbibition in presence of resistive gravity forces: Displacement characteristics and scaling. J. Unconv. Oil Gas Resour. 12, 68–86.
Modica, C.J., Lapierre, S.G., 2012. Estimation of kerogen porosity in source rocks as a function of thermal transformation: Example from the Mowry Shale in the Powder River Basin of WyomingEstimation of Kerogen Porosity as a Function of Thermal Transformation. AAPG Bull. 96, 87–108.
Mohammed, M., Babadagli, T., 2015. Wettability alteration: A comprehensive review of materials/methods and testing the selected ones on heavy-oil containing oil-wet systems. Adv. Colloid Interface Sci. 220, 54–77.
Montes, I., Lai, C., Sanabria, D., 2003. Like Dissolves Like: A Guided Inquiry Experiment for Organic Chemistry. J. Chem. Educ. 80, 447.
Morrow, N.R., Mason, G., 2001. Recovery of oil by spontaneous imbibition. Curr. Opin. Colloid Interface Sci. 6, 321–337.
Mouzakis, K.M., Navarre-Sitchler, A.K., Rother, G., Bañuelos, J.L., Wang, X., Kaszuba, J.P., Heath, J.E., Miller, Q.R.S., Alvarado, V., McCray, J.E., 2016. Experimental Study of Porosity Changes in Shale Caprocks Exposed to CO_2-Saturated Brines I: Evolution of Mineralogy, Pore Connectivity, Pore Size Distribution, and Surface Area. Environ. Eng. Sci. 33, 725–735.
Negin, C., Ali, S., Xie, Q., 2017. Most common surfactants employed in chemical enhanced oil recovery. Petroleum 3, 197–211.
Nguyen, P., Carey, J.W., Viswanathan, H.S., Porter, M., 2018. Effectiveness of supercritical-CO_2 and N_2 huff-and-puff methods of enhanced oil recovery in shale fracture networks using microfluidic experiments. Appl. Energy 230, 160–174.
Okiongbo, K.S., Aplin, A.C., Larter, S.R., 2005. Changes in Type II Kerogen Density as a Function of Maturity: Evidence from the Kimmeridge Clay Formation. Energy Fuels 19, 2495–2499.
Olatunji, K., Zhang, J., Wang, D., 2018. Effect of the rock dimension on surfactant imbibition rate in the Middle Member of Bakken: Creating a model for frac design. J. Pet. Sci. Eng. 169, 416–420.
Pan, B., Jones, F., Huang, Z., Yang, Y., Li, Y., Hejazi, S.H., Iglauer, S., 2019. Methane (CH_4) Wettability of Clay-Coated Quartz at Reservoir Conditions. Energy Fuels 33, 788–795.

Pan, B., Li, Y., Wang, H., Jones, F., Iglauer, S., 2018. CO_2 and CH_4 Wettabilities of Organic-Rich Shale. Energy Fuels 32, 1914–1922.
Pederssetti, M.M., Palú, F., da Silva, E.A., Rohling, J.H., Cardozo-Filho, L., Dariva, C., 2011. Extraction of canola seed (Brassica napus) oil using compressed propane and supercritical carbon dioxide. J. Food Eng. 102, 189–196.
Perera, M.S.A., Gamage, R.P., Rathnaweera, T.D., Ranathunga, A.S., Koay, A., Choi, X., 2016. A Review of CO_2-Enhanced Oil Recovery with a Simulated Sensitivity Analysis. Energies 9, 481.
Plug, W.-J., Bruining, J., 2007. Capillary pressure for the sand–CO_2–water system under various pressure conditions. Application to CO_2 sequestration. Adv. Water Resour. 30, 2339–2353.
Polyanin, A.D., Nazaikinskii, V.E., Nazaikinskii, V.E., 2015. Handbook of Linear Partial Differential Equations for Engineers and Scientists. Chapman and Hall/CRC.
Pooladi-Darvish, M., Firoozabadi, A., 2000. Cocurrent and Countercurrent Imbibition in a Water-Wet Matrix Block. SPE J. 5, 3–11.
Powles, J.G., 1985. On the validity of the Kelvin equation. J. Phys. Math. Gen. 18, 1551–1560.
Prather, C.A., Bray, J.M., Seymour, J.D., Codd, S.L., 2016. NMR study comparing capillary trapping in Berea sandstone of air, carbon dioxide, and supercritical carbon dioxide after imbibition of water. Water Resour. Res. 52, 713–724.
Prey, D., Lefebvre, E., 1978. Gravity and Capillarity Effects on Imbibition in Porous Media. Soc. Pet. Eng. J. 18, 195–206.
Psarras, P., Holmes, R., Vishal, V., Wilcox, J., 2017. Methane and CO_2 Adsorption Capacities of Kerogen in the Eagle Ford Shale from Molecular Simulation. Acc. Chem. Res. 50, 1818–1828.
Qin, T., Javanbakht, G., Goual, L., 2019. Nanoscale Investigation of Surfactant-Enhanced Solubilization of Asphaltenes from Silicate-Rich Rocks. Energy Fuels 33, 3796–3807.
Qin, T., Javanbakht, G., Goual, L., Piri, M., Towler, B., 2017. Microemulsion-enhanced displacement of oil in porous media containing carbonate cements. Colloids Surf. Physicochem. Eng. Asp. 530, 60–71.
Ross, D.J.K., Marc Bustin, R., 2009. The importance of shale composition and pore structure upon gas storage potential of shale gas reservoirs. Mar. Pet. Geol. 26, 916–927.
Roychaudhuri, B., Tsotsis, T.T., Jessen, K., 2013. An experimental investigation of spontaneous imbibition in gas shales. J. Pet. Sci. Eng. 111, 87–97.
Saidian, M., Prasad, M., 2015. Effect of mineralogy on nuclear magnetic resonance surface relaxivity: A case study of Middle Bakken and Three Forks formations. Fuel 161, 197–206.
Saif, T., Lin, Q., Butcher, A.R., Bijeljic, B., Blunt, M.J., 2017. Multi-scale multi-dimensional microstructure imaging of oil shale pyrolysis using X-ray micro-tomography, automated ultra-high resolution SEM, MAPS Mineralogy and FIB-SEM. Appl. Energy 202, 628–647.
Salehi, M., Johnson, S.J., Liang, J.-T., 2008. Mechanistic Study of Wettability Alteration Using Surfactants with Applications in Naturally Fractured Reservoirs. Langmuir 24, 14099–14107.
Sang, Q., Li, Y., Zhu, C., Zhang, S., Dong, M., 2016. Experimental investigation of shale gas production with different pressure depletion schemes. Fuel 186, 293–304.
Sang, Q., Zhang, S., Li, Y., Dong, M., Bryant, S., 2018. Determination of organic and inorganic hydrocarbon saturations and effective porosities in shale using vacuum-imbibition method. Int. J. Coal Geol. 200, 123–134.

Sarkisov, L., Harrison, A., 2011. Computational structure characterisation tools in application to ordered and disordered porous materials. Mol. Simul. 37, 1248–1257.
Sato, M., Panaghi, K., Takada, N., Takeda, M., 2019. Effect of Bedding Planes on the Permeability and Diffusivity Anisotropies of Berea Sandstone. Transp. Porous Media 127, 587–603.
Schmid, K.S., Alyafei, N., Geiger, S., Blunt, M.J., 2016. Analytical Solutions for Spontaneous Imbibition: Fractional-Flow Theory and Experimental Analysis. SPE J. 21, 2,308-2,316.
Schmid, K.S., Geiger, S., Sorbie, K.S., 2011. Semianalytical solutions for cocurrent and countercurrent imbibition and dispersion of solutes in immiscible two-phase flow. Water Resour. Res. 47.
ShamsiJazeyi, H., Miller, C.A., Wong, M.S., Tour, J.M., Verduzco, R., 2014. Polymer-coated nanoparticles for enhanced oil recovery. J. Appl. Polym. Sci. 131.
Shen, J., Zhao, J., Qin, Y., Shen, Y., Wang, G., 2018. Water imbibition and drainage of high rank coals in Qinshui Basin, China. Fuel 211, 48–59.
Sheng, J.J., 2017. What type of surfactants should be used to enhance spontaneous imbibition in shale and tight reservoirs? J. Pet. Sci. Eng. 159, 635–643.
Siddiqui, M.A.Q., Ali, S., Fei, H., Roshan, H., 2018. Current understanding of shale wettability: A review on contact angle measurements. Earth-Sci. Rev. 181, 1–11. https://doi.org/10.1016/j.earscirev.2018.04.002
Soltanian, M.R., Amooie, M.A., Cole, D.R., Darrah, T.H., Graham, D.E., Pfiffner, S.M., Phelps, T.J., Moortgat, J., 2018. Impacts of Methane on Carbon Dioxide Storage in Brine Formations. Groundwater 56, 176–186. https://doi.org/10.1111/gwat.12633
Song, C., Yang, D., 2017. Experimental and numerical evaluation of CO_2 huff-n-puff processes in Bakken formation. Fuel 190, 145–162.
Song, C., Yang, D., 2013. Performance Evaluation of CO_2 Huff-n-Puff Processes in Tight Oil Formations. Presented at the SPE Unconventional Resources Conference Canada, Society of Petroleum Engineers.
Song, L., Martin, K., Carr, T.R., Ghahfarokhi, P.K., 2019. Porosity and storage capacity of Middle Devonian shale: A function of thermal maturity, total organic carbon, and clay content. Fuel 241, 1036–1044.
Song, W., Yao, J., Ma, J., Sun, H., Li, Y., Yang, Y., Zhang, L., 2018. Numerical Simulation of Multiphase Flow in Nanoporous Organic Matter With Application to Coal and Gas Shale Systems. Water Resour. Res. 54, 1077–1092.
Song, Y., Wang, Shenglong, Yang, M., Liu, W., Zhao, J., Wang, Shanrong, 2015. MRI measurements of CO_2–CH_4 hydrate formation and dissociation in porous media. Fuel 140, 126–135.
Sonnenberg, S.A., Pramudito, A., 2009. Petroleum geology of the giant Elm Coulee field, Williston Basin. AAPG Bull. 93, 1127–1153.
Standnes, D.C., 2004. Experimental Study of the Impact of Boundary Conditions on Oil Recovery by Co-Current and Counter-Current Spontaneous Imbibition. Energy Fuels 18, 271–282.
Standnes, D.C., Austad, T., 2003. Wettability alteration in carbonates: Interaction between cationic surfactant and carboxylates as a key factor in wettability alteration from oil-wet to water-wet conditions. Colloids Surf. Physicochem. Eng. Asp. 216, 243–259.

Standnes, D.C., Nogaret, L.A.D., Chen, H.-L., Austad, T., 2002. An Evaluation of Spontaneous Imbibition of Water into Oil-Wet Carbonate Reservoir Cores Using a Nonionic and a Cationic Surfactant. Energy Fuels 16, 1557–1564.

Su, S., Jiang, Z., Shan, X., Zhu, Y., Wang, P., Luo, X., Li, Z., Zhu, R., Wang, X., 2018. The wettability of shale by NMR measurements and its controlling factors. J. Pet. Sci. Eng. 169, 309–316.

Sui, H., Yao, J., 2016. Effect of surface chemistry for CH_4/CO_2 adsorption in kerogen: A moleculhttps://doi.org/10.1016/j.jngse.2016.03.097

Tanahatoe, J.J., Kuil, M.E., 1997. Molar Mass Dependence of the Apparent Diffusion Coefficient of Flexible Highly Charged Polyelectrolytes in the Dilute Concentration Regime. J. Phys. Chem. A 101, 8389–8394.

Tang, X., Jiang, Z., Jiang, S., Wang, P., Xiang, C., 2016. Effect of Organic Matter and Maturity on Pore Size Distribution and Gas Storage Capacity in High-Mature to Post-Mature Shales. Energy Fuels 30, 8985–8996.

Tao, Z., Clarens, A., 2013. Estimating the Carbon Sequestration Capacity of Shale Formations Using Methane Production Rates. Environ. Sci. Technol. 47, 11318–11325.

Tesson, S., Firoozabadi, A., 2019. Deformation and Swelling of Kerogen Matrix in Light Hydrocarbons and Carbon Dioxide. J. Phys. Chem. C 123, 29173–29183.

Tian, Y., Xiong, Y., Wang, L., Lei, Z., Zhang, Y., Yin, X., Wu, Y.-S., 2019a. A compositional model for gas injection IOR/EOR in tight oil reservoirs under coupled nanopore confinement and geomechanics effects. J. Nat. Gas Sci. Eng. 71, 102973.

Tian, Y., Yu, X., Li, J., Neeves, K.B., Yin, X., Wu, Y.-S., 2019b. Scaling law for slip flow of gases in nanoporous media from nanofluidics, rocks, and pore-scale simulations. Fuel 236, 1065–1077.

Wang, D., Liu, C., Wu, W., Wang, G., 2010. Novel Surfactants that Attain Ultra-Low Interfacial Tension between Oil and High Salinity Formation Water without adding Alkali, Salts, Co-surfactants, Alcohols and Solvents. Presented at the SPE EOR Conference at Oil & Gas West Asia, Society of Petroleum Engineers.

Wang, D., Zhang, J., Butler, R., Koskella, D., Rabun, R., Clark, A., 2014. Flow Rate Behavior and Imbibition Comparison Between Bakken and Niobrara Formationsrch. Presented at the SPE/AAPG/SEG Unconventional Resources Technology Conference, Unconventional Resources Technology Conference.

Wang, J., Shao, Y., Yan, X., Zhu, J., 2019. Review of (gas)-liquid-solid circulating fluidized beds as biochemical and environmental reactors. Chem. Eng. J. 121951.

Wang, J., Wang, B., Li, Y., Yang, Z., Gong, H., Dong, M., 2016. Measurement of dynamic adsorption–diffusion process of methane in shale. Fuel 172, 37–48.

Wang, J., Yuan, Q., Dong, M., Cai, J., Yu, L., 2017. Experimental investigation of gas mass transport and diffusion coefficients in porous media with nanopores. Int. J. Heat Mass Transf. 115, 566–579.

Wang, L., Yao, B., Xie, H., Kneafsey, T.J., Winterfeld, P.H., Yin, X., Wu, Y.-S., 2017. Experimental investigation of injection-induced fracturing during supercritical CO_2 sequestration. Int. J. Greenh. Gas Control 63, 107–117.

Wang, L., Yin, R., Sima, L., Fan, L., Wang, H., Yang, Q., Huang, L., 2018. Insights into Pore Types and Wettability of a Shale Gas Reservoir by Nuclear Magnetic Resonance: Longmaxi Formation, Sichuan Basin, China. Energy Fuels 32, 9289–9303. https://doi.org/10.1021/acs.energyfuels.8b02107

Wang, S., Feng, Q., Javadpour, F., Xia, T., Li, Z., 2015. Oil adsorption in shale nanopores and its effect on recoverable oil-in-place. Int. J. Coal Geol. 147–148, 9–24.
Wang, S., Javadpour, F., Feng, Q., 2016. Fast mass transport of oil and supercritical carbon dioxide through organic nanopores in shale. Fuel 181, 741–758.
Wang, T., Tian, S., Li, G., Sheng, M., Ren, W., Liu, Q., Zhang, S., 2018. Molecular Simulation of CO_2/CH_4 Competitive Adsorption on Shale Kerogen for CO_2 Sequestration and Enhanced Gas Recovery. J. Phys. Chem. C 122, 17009–17018.
Wang, X., Sheng, J.J., 2018. Spontaneous imbibition analysis in shale reservoirs based on pore network modeling. J. Pet. Sci. Eng. 169, 663–672.
Wang, Z., Li, Y., Liu, H., Zeng, F., Guo, P., Jiang, W., 2017. Study on the Adsorption, Diffusion and Permeation Selectivity of Shale Gas in Organics. Energies 10, 142.
Weck, P.F., Kim, E., Wang, Y., Kruichak, J.N., Mills, M.M., Matteo, E.N., Pellenq, R.J.-M., 2017. Model representations of kerogen structures: An insight from density functional theory calculations and spectroscopic measurements. Sci. Rep. 7, 7068.
Wei, B., Zhang, X., Liu, J., Xu, X., Pu, W., Bai, M., 2020. Adsorptive behaviors of supercritical CO_2 in tight porous media and triggered chemical reactions with rock minerals during CO_2-EOR and -sequestration. Chem. Eng. J. 381, 122577.
Wei, Z., Gao, X., Zhang, D., Da, J., 2005. Assessment of Thermal Evolution of Kerogen Geopolymers with Their Structural Parameters Measured by Solid-State 13C NMR Spectroscopy. Energy Fuels 19, 240–250.
Wu, J., Yu, J., Wang, Z., Fu, X., Su, W., 2018. Experimental investigation on spontaneous imbibition of water in coal: Implications for methane desorption and diffusion. Fuel 231, 427–437.
Wu, T., Zhao, H., Tesson, S., Firoozabadi, A., 2019. Absolute adsorption of light hydrocarbons and carbon dioxide in shale rock and isolated kerogen. Fuel 235, 855–867.
Xie, X., Krooss, B.M., Littke, R., Amann-Hildenbrand, A., Li, M., Li, Z., Snowdon, L.R., Mohnhoff, D., 2019. Accessibility and mobility of hydrocarbons in lacustrine shale: Solvent flow-through extraction experiments on Eocene oil shales from Bohai Bay Basin, eastern China. Org. Geochem. 127, 23–36.
Xu, H., Tang, D., Zhao, J., Li, S., 2015. A precise measurement method for shale porosity with low-field nuclear magnetic resonance: A case study of the Carboniferous–Permian strata in the Linxing area, eastern Ordos Basin, China. Fuel 143, 47–54.
Xu, M., Binazadeh, M., Zolfaghari, A., Dehghanpour, H., 2018. Effects of Dissolved Oxygen on Water Imbibition in Gas Shales. Energy Fuels 32, 4695–4704.
Xu, Z., Cheng, L., Cao, R., Jia, P., Wu, J., 2017. Simulation of counter-current imbibition in single matrix and field scale using radical integral boundary element method. J. Pet. Sci. Eng. 156, 125–133.
Yang, R., Guo, X., Yi, J., Fang, Z., Hu, Q., He, S., 2017. Spontaneous Imbibition of Three Leading Shale Formations in the Middle Yangtze Platform, South China. Energy Fuels 31, 6903–6916.
Yang, Y., Liu, J., Yao, J., Kou, J., Li, Z., Wu, T., Zhang, K., Zhang, L., Sun, H., 2020. Adsorption behaviors of shale oil in kerogen slit by molecular simulation. Chem. Eng. J. 387, 124054.
Yang, Z., Dong, M., Zhang, S., Gong, H., Li, Y., Long, F., 2016. A method for determining transverse permeability of tight reservoir cores by radial pressure pulse decay measurement. J. Geophys. Res. Solid Earth 121, 7054–7070. https://doi.org/10.1002/2016JB013173

Yang, Z., Dong, Z., Wang, L., Yin, T., Fan, X., Lin, M., Zhang, J., 2018. Experimental Study on Selective Adsorption/Desorption of CO_2 and CH_4 Behaviors on Shale under a High-Pressure Condition. Energy Fuels 32, 9255–9262. https://doi.org/10.1021/acs.energyfuels.8b02068

Yao, Y., Liu, D., Che, Y., Tang, D., Tang, S., Huang, W., 2010. Petrophysical characterization of coals by low-field nuclear magnetic resonance (NMR). Fuel, 17th International Symposium on Alcohol Fuels 89, 1371–1380.

Yassin, M.R., Begum, M., Dehghanpour, H., 2017. Organic shale wettability and its relationship to other petrophysical properties: A Duvernay case study. Int. J. Coal Geol. 169, 74–91.

Yildiz, H.O., Gokmen, M., Cesur, Y., 2006. Effect of shape factor, characteristic length, and boundary conditions on spontaneous imbibition. J. Pet. Sci. Eng. 53, 158–170.

Yin, H., Zhou, J., Jiang, Y., Xian, X., Liu, Q., 2016. Physical and structural changes in shale associated with supercritical CO_2 exposure. Fuel 184, 289–303.

Yu, W., Lashgari, H.R., Wu, K., Sepehrnoori, K., 2015. CO_2 injection for enhanced oil recovery in Bakken tight oil reservoirs. Fuel 159, 354–363.

Yuan, C.-D., Pu, W.-F., Wang, X.-C., Sun, L., Zhang, Y.-C., Cheng, S., 2015. Effects of Interfacial Tension, Emulsification, and Surfactant Concentration on Oil Recovery in Surfactant Flooding Process for High Temperature and High Salinity Reservoirs. Energy Fuels 29, 6165–6176.

Yuan, W., Pan, Z., Li, X., Yang, Y., Zhao, C., Connell, L.D., Li, S., He, J., 2014. Experimental study and modelling of methane adsorption and diffusion in shale. Fuel 117, 509–519.

Yuan, Y., Rezaee, R., 2019. Impact of Paramagnetic Minerals on NMR-Converted Pore Size Distributions in Permian Carynginia Shales. Energy Fuels 33, 2880–2887.

Yuan, Y., Rezaee, R., Verrall, M., Hu, S.-Y., Zou, J., Testmanti, N., 2018. Pore characterization and clay bound water assessment in shale with a combination of NMR and low-pressure nitrogen gas adsorption. Int. J. Coal Geol. 194, 11–21.

Zeebe, R.E., 2011. On the molecular diffusion coefficients of dissolved CO_2, HCO^{3-}, and CO_3^{2-} and their dependence on isotopic mass. Geochim. Cosmochim. Acta 75, 2483–2498.

Zeng, L., Zhang, Y., Liu, Q., Yang, L., Xiao, J., Liu, X., Yang, Y., 2016. Determination of mass transfer coefficient for continuous removal of cadmium by emulsion liquid membrane in a modified rotating disc contactor. Chem. Eng. J. 289, 452–462.

Zhang, Han, 1996. Viscosity and Density of Water + Sodium Chloride + Potassium Chloride Solutions at 298.15 K. J. Chem. Eng. Data 41, 516–520.

Zhang, K., 2016. Experimental and Numerical Investigation of Oil Recovery from Bakken Formation by Miscible CO_2 Injection. Presented at the SPE Annual Technical Conference and Exhibition, Society of Petroleum Engineers.

Zhang, L., Liang, H., Zhao, Y., Xie, J., Peng, X., Li, Q., 2020. Gas transport characteristics in shale matrix based on multiple mechanisms. Chem. Eng. J. 386, 124002.

Zhang, M., Zhan, S., Jin, Z., 2020. Recovery mechanisms of hydrocarbon mixtures in organic and inorganic nanopores during pressure drawdown and CO_2 injection from molecular perspectives. Chem. Eng. J. 382, 122808.

Zhang, S., Li, C., Pu, H., Ling, K., Sun, R., Zhao, J.X., 2019a. Experimental Study of Surfactant-Assisted Oil Recovery in the Middle Bakken Cores. Presented at the SPE Liquids-Rich Basins Conference - North America, Society of Petroleum Engineers.

Zhang, S., Li, Y., Pu, H., 2020. Studies of the storage and transport of water and oil in organic-rich shale using vacuum imbibition method. Fuel 266, 117096.

Zhang, S., Pu, H., Zhao, J.X., 2019b. Experimental and Numerical Studies of Spontaneous Imbibition with Different Boundary Conditions: Case Studies of Middle Bakken and Berea Cores. Energy Fuels 33, 5135–5146.
Zhang, Y., Yu, W., Li, Z., Sepehrnoori, K., 2018. Simulation study of factors affecting CO_2 Huff-n-Puff process in tight oil reservoirs. J. Pet. Sci. Eng. 163, 264–269.
Zhong, X., Pu, H., Zhou, Y., Zhao, J.X., 2019a. Comparative Study on the Static Adsorption Behavior of Zwitterionic Surfactants on Minerals in Middle Bakken Formation. Energy Fuels 33, 1007–1015.
Zhong, X., Pu, H., Zhou, Y., Zhao, J.X., 2019b. Static Adsorption of Surfactants on Bakken Rock Surfaces in High Temperature, High Salinity Conditions. Presented at the SPE International Conference on Oilfield Chemistry, Society of Petroleum Engineers.
Zhou, J., Xie, S., Jiang, Y., Xian, X., Liu, Q., Lu, Z., Lyu, Q., 2018. Influence of Supercritical CO_2 Exposure on CH_4 and CO_2 Adsorption Behaviors of Shale: Implications for CO_2 Sequestration. Energy Fuels 32, 6073–6089.
Zhou, X., Yuan, Q., Zhang, Y., Wang, H., Zeng, F., Zhang, L., 2019. Performance evaluation of CO_2 flooding process in tight oil reservoir via experimental and numerical simulation studies. Fuel 236, 730–746.
Zhu, C., Li, Y., Zhao, Q., Gong, H., Sang, Q., Zou, H., Dong, M., 2018. Experimental study and simulation of CO_2 transfer processes in shale oil reservoir. Int. J. Coal Geol. 191, 24–36.
Zhu, C., Sheng, J., Ettehadtavakkol, A., Li, Y., Gong, H., Li, Z., Dong, M., 2020. Numerical and Experimental Study of Enhanced Shale-Oil Recovery by CO_2 Miscible Displacement with NMR. Energy Fuels 34, 1524–1536.